

# Macroporous Polymer-Derived Ceramic Monoliths for Cryogenic Applications Manufactured by Water-Based Freeze Casting

Dem Fachbereich Produktionstechnik

der

UNIVERSITÄT BREMEN

Zur Erlangung des Grades

Doktor-Ingenieur

genehmigte

Dissertation

von

M.Sc. Huixing Zhang

Gutachter:

Prof. Dr.-Ing. Kurosch Rezwan, Prof. Dr.rer.nat. Michael Scheffler

Tag der mündlichen Prüfung: 24. April 2018



## Acknowledgements

Firstly, I would like to thank Prof. Dr. Ing. Kurosch for giving me opportunity to work in Advanced Ceramics Group, his advice and scientific help during this time. I would like to thank Dr. rer. nat. Michaela Wilhelm for all her help, advice during the last 4 years, both in scientific work and in life. I would like to thank Prof. Dr. rer. nat. Michael Scheffler to be the co-examiner of my thesis.

I would like to thank the group members of Advanced Ceramics Group for all the scientific discussion, and advices which greatly extended my knowledge in many fields. I would like to thank especially the members from polymer derived ceramics group for their useful comments and discussion and share of knowledge.

I would like to thank the entire technical staff in Advanced Ceramics Group for their sharing of knowledge and help. I would like to thank Christian Ellenberg for his immediate help for solving the technique problem in the lab. I would like to thank Tina Kühn, Christian Nuortila and Jürgen Horvath for their help in laboratory. I would like to thank the administrative staff Gabriela Berger, Andrea Baitz, Sabine Vogelsang, for their help in the office.

This work was supported by German Research Foundation (DFG) within the Research Training Group GRK 1860 “Micro-, meso- and macroporous nonmetallic Materials: Fundamentals and Applications” (MIMENIMA). I would like to thank Prof. Michael Dreyer for all the useful discussion and advice during the progress reports and scientific discourses during my involvement in MIMENIMA research training group. I would like to thank also the all the other members of MIMENIMA for their insights regarding my work, especially Yulia Grebenyuk, during the scientific discourse, progress report and workshops organized by the PhD students and post doctors.

I thank Prof. Zhipeng Xie in Tsinghua University, China and Prof. Laifeng Li in Chinese Academy of Sciences for support in thermal properties measurement at cryogenic temperature during my research abroad in China. I would like to thank Vassilios Siozios of the department of Application thermal analysis at TA Instruments (Waters GmbH) for carrying out low temperature specific heat capacity measurement.

I would like to thank all the students contribute to this work. Their contributions are listed at the end of this work.

I would like to thank the group members, especially Ludmilla Derr and Gesa Hollermann for their kindness and patience to help me to get into a different culture better.

I would like to thank my family and friends for supporting me all the time during the period of this work.

## Contents

Acknowledgements.....	iii
Zusammenfassung.....	viii
Abstract.....	x
List of abbreviations and important symbols.....	xii
Materials and chemical structure.....	xv
1. Introduction.....	1
References.....	3
2. State of the art.....	5
2.1 Materials for cryogenic engineering and requirements for their applications.....	5
2.1.1 Materials for cryogenic engineering.....	5
2.1.2 Cryogenic wicking in porous materials.....	6
2.2 Thermal properties of porous ceramics.....	9
2.2.1 Thermal conductivity, thermal expansion and specific heat capacity of ceramics.....	9
2.2.2 Thermal properties of porous ceramics.....	11
2.3 Mechanical properties of porous ceramics.....	14
2.3.1 Mechanical properties of ceramics.....	14
2.3.2 Compressive strength of porous materials.....	15
2.2.3 Compressive strength of ceramics at cryogenic temperatures.....	17
2.4 Design of macroporous ceramics for different applications.....	17
2.4.1 Fabrication of macroporous structure.....	17
2.4.2 Macroporous ceramics in different applications.....	25
2.5 Polymer derived ceramics.....	25
2.5.1 Cross-linking and pyrolytic conversion of preceramic polymers.....	25
2.5.2 Adjustment of porosity and surface characteristics.....	27
2.5.3 Polymer derived ceramics as structural materials and for other applications.....	29
References.....	30
3. Aim of the work and approach.....	37
4. Characterization methods.....	39
4.1 Zeta potential and particle size analysis.....	39

## Contents

---

4.1.1 Zeta potential .....	39
4.1.2 Particle size analysis.....	40
4.2 Characterization of specific surface area.....	40
4.3 Characterization of porous structure .....	42
4.3.1 Micro/mesoporosity measurement .....	42
4.3.2 Macroporosity measurement.....	43
4.4 Characterization of surface characteristics.....	44
4.5 Compressive strength analysis .....	44
4.6 Characterization of thermal properties .....	46
4.6.1 Thermal conductivity.....	46
4.6.2 Specific heat capacity .....	48
4.6.3 Coefficient of thermal expansion.....	48
4.7 Permeability measurement .....	49
References .....	51
5. Adjusting hydrophilicity of polysiloxane by thermal decomposition for freeze casting.....	53
5.1 Introduction.....	53
5.2 Experimental details.....	55
5.2.1 Material .....	55
5.2.2 Processing.....	55
5.2.3 Characterization .....	57
5.3 Results .....	57
5.3.1 Properties of H44-derived fillers.....	57
5.3.2 Pore structure and porosity.....	59
5.3.3 Specific surface area and hierarchical structure .....	61
5.3.4 Surface characteristics .....	62
5.4 Discussion.....	63
5.4.1 Lamellar morphology of SiOC materials.....	63
5.4.2 Hierarchical structure.....	63
5.4.3 Influences of the process parameters .....	64
5.5 Conclusion.....	65
References .....	65

6. Adjusting hydrophilicity of polysiloxane by composition for freeze casting..... 68

6.1 Introduction..... 68

6.2 Experimental procedure ..... 70

6.2.1. Materials ..... 70

6.2.2 Processing..... 70

6.2.3. Characterizations ..... 72

6.3 Results ..... 73

6.3.1 Fillers ..... 73

6.3.2 Monoliths prepared by freeze casting ..... 76

6.4 Discussion..... 80

6.4.1 Modification of surface characteristics of fillers ..... 80

6.4.2 The hierarchical porous structure ..... 82

6.4.3 Influences of silica sol..... 83

6.4.4 Influences of process parameters..... 83

6.5 Conclusion ..... 84

References ..... 84

7. Cryogenic properties of unidirectional porous SiOC ceramics ..... 88

7.1 Introduction..... 89

7.2 Materials and methods ..... 91

7.2.1 Preparation of hybrid filler ..... 92

7.2.2 Freeze casting process ..... 92

7.2.3 Characterizations ..... 92

7.3 Results ..... 94

7.4 Discussion..... 100

7.4.1 The influence of environmental temperature on compressive strength ..... 100

7.4.2 Influence of compositions and anisotropy on coefficients of thermal expansion..... 102

7.4.3. Thermal conductivity of hierarchically-ordered porous monolith ..... 104

7.4.4 Potential applications..... 106

7.5 Conclusion ..... 106

References ..... 107

8. Conclusions ..... 111

## Contents

---

9. Outlook .....	114
Appendix.....	116

### Zusammenfassung

Makroporöse SiOC-Keramiken wurden durch ein wasserbasiertes Gefriergussverfahren unter Verwendung von Polysiloxanen als Vorläufer und Kieselzol als Wasserphase und Bindemittel hergestellt. Die erhaltenen porösen Monolithe haben eine anisotrope poröse Struktur und anisotrope thermische und mechanische Eigenschaften. Das makroporöse SiOC wurde für kryogene Anwendungen entwickelt, die Massentransportprozesse und thermische Transportprozesse beinhalten.

Der erste Teil dieser Arbeit konzentriert sich auf die Herstellung von makroporösen Monolithen. Um dieses wasserbasierten Gefriergussverfahren verwenden zu können, wurden die präkeramischen Polymere hinsichtlich ihrer hydrophilen/hydrophoben Oberflächeneigenschaften modifiziert. Für die Oberflächenmodifikation wurden zwei Ansätze gewählt.

Der erste Ansatz zur Modifizierung der Benetzbarkeit des Präkursors war die Pyrolyse des Methylpolysiloxanen (H44) in Inertgas bei niedriger Temperatur, wodurch hybridkeramische Materialien (H44-Füllstoff) erzeugt wurden. Über die Pyrolysetemperatur können die Oberflächeneigenschaften variiert werden. H44-Füller, die durch Pyrolyse von Methylphenylpolysiloxan bei 600 °C erhalten wurden, waren hydrophil genug, um als Festphase in einem wasserbasierten Verfahren eingesetzt werden zu können. Der Einfluss der Feststoffbeladung, der Gefriertemperaturen und der Pyrolysetemperaturen auf die Porosität und die spezifische Oberfläche wurden untersucht. Die Kombination von polymer-abgeleiteten Füllern mit dem Gefriergussverfahren führte bei Pyrolysetemperatur von 600–700 °C zu einer trimodalen Porenstruktur (Mikro/Meso/Makroporen). Die spezifische Oberfläche zeigte auch bei einer Pyrolysetemperatur von 1000 °C noch hohe Werte von bis zu 74 m<sup>2</sup>·g<sup>-1</sup> aufweisen. Die Porenform kann je nach Gefriertemperatur von lamellar bis röhrenförmig angepasst werden.

Der zweite Ansatz zur Modifizierung der Benetzbarkeit bestand darin, mehr hydrophile Gruppen auf der Oberfläche von Methylpolysiloxan (MK) durch Vernetzung mit (3-Aminopropyl)triethoxysilan (APTES) einzuführen. Die Molverhältnisse zwischen MK und APTES und Pyrolysetemperatur beeinflussten die Mengen an Aminopropylgruppen auf der Oberfläche der vernetzten Produkte, die wiederum die Basizität und Hydrophilie veränderten. Bei beiden Methoden waren neben den Oberflächeneigenschaften auch Oberflächenladungen zur Erzeugung stabiler Suspensionen verantwortlich, die zur Herstellung homogen aufgebauter Monolithe notwendig sind. Insbesondere der mit einem MK: APTES-Molverhältnis von 1: 1 hergestellte und bei 600 °C pyrolysierte Füller, war aufgrund seiner guten Benetzbarkeit und der Suspensionsstabilität für das Gefriergießen anwendbar. Der MK-APTES abgeleitete Monolith zeigte ebenfalls eine hierarchische Mikro/Meso/Makroporöse Struktur. Die Dampfadsorptionsmessung zeigte, dass ein hoher Gehalt an Kieselzol die Hydrophilie erwartungsgemäß stark verbesserte und auch die Pyrolysetemperatur die Hydrophilie in



geringem Maße beeinflusste. Bemerkenswerterweise war das Kieselöl für die Bildung von Mesoporen verantwortlich.

Der zweite Teil der Arbeit bestand darin die mechanischen und thermischen Eigenschaften von unidirektionalen porösen SiOC-Keramiken, die mit MK und H44 hergestellt wurden, bei kryogenen Temperaturen und Raumtemperatur zu untersuchen. Die Druckfestigkeit von Monolithen wurde sowohl in Luft (293 K) als auch in flüssigem Stickstoff (77 K) untersucht. Der Einfluss sowohl der Flüssigkeit als auch der kryogenen Temperatur auf die Druckfestigkeit wurde untersucht. Die Druckfestigkeit der Monolithen zeigte nicht nur Anisotropie, sondern auch eine signifikante Zunahme in flüssigem Stickstoff. Diese Zunahme kann auf den in den porösen Strukturen gefangenen flüssigen Stickstoff und die kryogene Temperatur zurückzuführen sein. Der lineare thermische Ausdehnungskoeffizient, die Wärmeleitfähigkeit und die spezifische Wärmekapazität von porösem SiOC wurden von der Kryogentemperatur bis zur Raumtemperatur untersucht. Die Monolithen beider Materialien zeigten anisotrope lineare Ausdehnungskoeffizienten, wobei die Schrumpfung in paralleler Richtung fast das Doppelte der Schrumpfung der senkrechten Richtung aufwies. Der mit H44 hergestellte Monolith zeigte eine thermische Schrumpfung, die doppelt so hoch ist, wie die der mit MK und APTES hergestellten Monolithe. Dies kann auf die Zusammensetzungsunterschiede und die Messbedingungen zurückgeführt werden. Die thermischen Leitfähigkeiten beider Monolithen aus zwei Präkursoren zeigten anisotrope Merkmale und ähnliche Werte. Die minimalen und maximalen Werte für die Wärmeleitfähigkeit sind  $0,2$  und  $0,9 \text{ W}\cdot\text{m}^{-1}\cdot\text{K}^{-1}$ . Wärmeleitfähigkeiten und spezifische Wärmekapazitäten zeigten einen Aufwärtstrend von niedriger Temperatur zu Raumtemperatur. Es wurde angenommen, dass die maximalen Wärmeleitfähigkeiten dieser Materialien hauptsächlich durch die Makroporosität und die Wärmeleitfähigkeit des Hybridmaterials bestimmt wurden.

## Abstract

Macroporous SiOC ceramics were prepared by a water-based freeze casting process, using polysiloxanes as precursors and silica sol as water phase and binder. The obtained porous monoliths have anisotropic porous structure and thermal and mechanical properties. The macroporous SiOC aimed at cryogenic applications which involve mass transport and thermal transport processes.

The first part of the thesis focuses on manufacturing macroporous monoliths, in which process the surface characteristics of preceramic polymers in terms of hydrophobicity/hydrophilicity were modified to be used in the water-based freeze casting process. Two approaches were chosen for the surface modification.

The first approach to modify the wettability of the precursor was pyrolysis of hydrophobic methyl phenyl polysiloxanes (H44) in inert gas at low temperature, by which hybrid ceramic materials (H44-derived filler) were generated. Depending on the pyrolysis temperatures, the surface characteristics can be varied from hydrophobic to hydrophilic. H44-derived fillers obtained by pyrolyzing methyl phenyl polysiloxane at 600 °C were hydrophilic enough to be used as solid phase in water-based process. The influence of solid loading, freeze temperatures and pyrolysis temperatures on porosity and specific surface areas were investigated. The combination of polymer derived filler materials with freezing casting method resulted in the trimodal pore structure (micro/meso/macropore) at pyrolysis temperature of 600–700 °C. Even at pyrolysis temperature of 1000 °C, the specific surface area was be as high as 74 m<sup>2</sup>·g<sup>-1</sup>. The pore shape can be tailored from lamellar to tubular depending on freezing temperatures.

The second approach to modify the wettability was to introduce more hydrophilic groups to the hydrophobic methyl polysiloxane (MK) by cross-linking with (3-Aminopropyl)triethoxysilane (APTES). The molar ratios between MK and APTES and pyrolysis temperature led to different amounts of aminopropyl groups in the cross-linked products, which altered the basicity and hydrophilicity. For both approaches, besides the surface characteristics, surface charges also account for stable suspension to prepare final homogenous monoliths. Filler material prepared with MK: APTES molar ratio of 1:1, pyrolyzed at 600 °C was applicable for freeze casting considering the wettability and suspension stability. The monolith prepared with MK-APTES derived filler had also a hierarchical micro/meso/macroporous structure. The vapor adsorption indicated that the high content of silica sol improved the hydrophilicity greatly, and pyrolysis temperature also influenced the hydrophilicity to a minor degree. Notably, the silica sol is responsible for the formation of mesopores.

The second part of the thesis was to investigate the mechanical and thermal properties of the obtained unidirectional porous SiOC ceramics prepared with MK and H44 at cryogenic and room temperatures. The compressive strength of monoliths was investigated both in air (293 K) and in liquid nitrogen (77 K). The influence of both liquid and cryogenic temperature on

compressive strength was investigated. The compressive strength of monoliths showed not only anisotropy, but also a significant increase in liquid nitrogen. This increase may be due to the liquid nitrogen trapped inside the porous structures and cryogenic temperature. The linear thermal expansion coefficients (CTE), thermal conductivity and specific heat capacity of porous SiOC, were studied from cryogenic to room temperature. Both monoliths show anisotropic linear expansion coefficients, with the parallel direction having almost twice the shrinkage of the perpendicular direction. The monolith prepared with H44 showed thermal shrinkage twice as much as that prepared with MK and APTES, which might be due to the composition differences and measurement condition. The thermal conductivities of both monoliths made from two precursors showed anisotropic features and similar values. The minimum and maximum values for thermal conductivity are 0.2 and 0.9  $W \cdot m^{-1} \cdot K^{-1}$ . Thermal conductivities and specific heat capacities displayed an upward trend from low temperature to room temperature. It was assumed that the maximum heat conductivities of these materials were determined mainly by the macroporosity and the thermal conductivity of the hybrid material.

## List of abbreviations and important symbols

APTES	3-(Aminopropyl)triethoxysilane
BET	Brunauer–Emmett–Teller method
BJH	Barret-Joyner-Halenda method
CMC	Ceramic-matrix composite
DSC	Differential scanning calorimetry
DI	Dry ice
EMT	Effective Medium Theory
FZ	Freeze casting
H44	Silres® H44, methyl phenyl polysiloxane
LN	Liquid nitrogen
MK	Silres® MK, methyl polysiloxane
PAA	Polyacrylic acid
PDCs	Polymer derived ceramics
PMA	Polyacrylamide
PVA	Polyvinyl alcohol
PVC	Polyvinyl chloride
SEM	Scanning electron microscopy
SSA	Specific surface area
TBA	Tert-butyl alcohol
TEOS	Tetraethyl orthosilicate
TESPSA	3-(triethoxysilyl)propylsuccinic anhydride
TGA	Thermogravimetric analysis
XRD	X- ray diffraction

$b$	Constant related directly to the pore characteristics,
$C$	Constant
$C_p$	Specific heat capacity
$d$	Dimension of pore
$E$	Elastic modulus
$K$	Material constants in Weibull's statistical theory
$K_p, K_{z+}, K_{z-}$	Permeability of porous materials
$k_g$	Thermal conductivity of gas
$k'_g$	Thermal conductivity of pore in vacuum (=0)
$k_{mine}$	Minimum effective thermal conductivity
$k_{maxe}$	Maximum effective thermal conductivity
$k_{s-hybrid}$	Thermal conductivity of hybrid materials
$k_{s-wall}$	Thermal conductivity of lamellar walls
$l$	Crack size in Griffith equation
$\Delta L/L$	Strain
$m$	Weibull modulus
$m_s$	Sample weight
$p_L$	Longitudinal pore fraction in anisotropic porous structure
$p_0$	Cross-sectional pore fraction in anisotropic porous structure
$p_t$	Total porosity
$P_{water}$	Volume percentage of water in the pores
$P/P_0$	Relative pressure
$P_w$	Probability of failure in Weibull's statistical theory

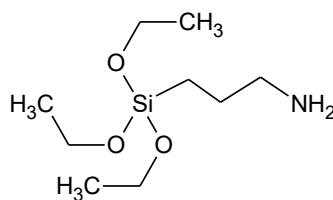
## List of abbreviations and important symbols

---

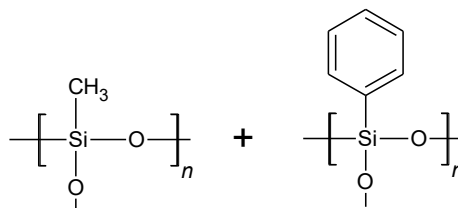
$Q$	Heat flow rate
$T_m$	Mean absolute temperature
$v_{meso-p}$	Mesoporosity inside lamellar walls
$v_{solid}$	Solid volume percent inside lamellar walls
$V_s$	Solid volume
$V_p$	Pore volume
$W_{vapor}$	Water adsorption per gram of ceramics
$\alpha$	Thermal diffusivity
$\alpha_l$	Coefficient of thermal expansion in longitudinal direction
$\alpha_t$	Coefficient of thermal expansion in transverse direction
$\zeta$	Zeta potential
$\epsilon$	Strain
$\varepsilon$	Emissivity in Leob equation
$\rho$	Density
$\nu$	Poisson's ratio
$\gamma_0$	Surface energy
$\sigma$	Compressive strength
$\sigma_0$	Characteristic strength in Weibull's statistical theory

## Materials and chemical structure

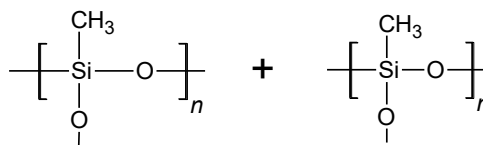
APTES 3-(Aminopropyl)triethoxysilane



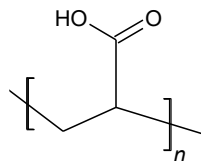
H44 Silres® H44  
Methyl phenyl polysiloxane



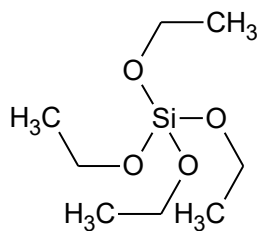
MK Silres® MK  
Methyl polysiloxane



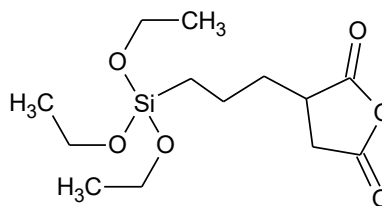
PAA Polyacrylic acid



TEOS Tetraethyl orthosilicate



TESPSA 3-(triethoxysilyl)propylsuccinic anhydride







## 1. Introduction

Cryogenic temperature has no fixed temperature range; generally it refers to the temperature lower than  $-150\text{ }^{\circ}\text{C}$  (123K) [1]. Cryogenic applications or cryogenic engineering includes aerospace applications [2], or superconducting areas [3], etc. Capillary transport of cryogenic liquids is one special application in this area.

Cryogenic liquids like liquid hydrogen, liquid oxygen and liquid methane, etc. are used as propellants in the space technology. The propellant management devices which are designed to separate the liquid propellants from the pressured gas in the tanks under zero gravity are based on the wicking (capillary transport) and bubble point phenomena [4]. The porous structure component in the propellant management device allows the liquid to permeate, but blocks out gas below a critical differential pressure. The low surface tension of cryogenic liquid determined the pore size range to be tens of micrometers. Thus, the adjusted design of the porous medium is of vital importance.

In this cryogenic space application, metallic components are commonly used and most research work of the capillary transport of cryogenic liquids is also focused on using metallic weaves as transport medium [5]. However, the metal components are of high density and suffer from corrosion with time. Therefore, new substitute materials are need. Ceramic porous materials have high strength, low density and strong corrosive resistance, which may be promising materials to replace metallic weaves. So far, there has been some initial study on the capillary transport of cryogenic liquid using porous structured metallic weaves and glass frits in literature [6]. Due to a high flexibility to modify the porosity on different length scales as well as the wetting of the surfaces, polymer derived ceramics (PDCs) have been under research for many applications [7] and are promising materials for the capillary transport of cryogenic liquids. Therefore their surface characteristics, the macropore sizes and porosity were adjusted and investigated in the present study.

In this work, freeze casting technique was used to create the anisotropic macroporous polymer derived ceramics. Freeze casting produces monoliths of high permeability and the monolith size can easily be scaled up, which is very important for this application. Porous polymer derived ceramics are normally prepared with solution based freeze casting method, in which process the preceramic polymers dissolve in organic solvents, such as *tert*-butyl alcohol, camphene, cyclohexane, etc. For example, porous SiOC or SiC ceramics have been prepared by freeze casting using preceramic polymers as precursors and camphene and *tert*-butyl alcohol as solvents [8-9]. However, the degree of cross-linking needs to be carefully monitored. Insufficient cross-linking leads to poor mechanical integrity and excessive cross-linking of polymer solution causes gelation before freezing. In this work, preceramic polymers were used in a suspension based freeze casting, using water as the solvent. The results showed that it can avoid the problem of over or insufficient cross-linking, and the monoliths also have less shrinkage.

The mechanical and thermal properties of ceramics change with temperature. The porous ceramics for cryogenic applications are fabricated at room temperature, but operate at cryogenic temperature. Additionally, they carry loads between ambient and low temperature components. Therefore, investigation of thermal and mechanical properties of the porous ceramics is very important for this application. However, there is little work on mechanical and thermal properties of porous ceramics at cryogenic temperature. Although there has been extensive investigation of mechanical properties of the ceramics at room temperature or higher temperatures, it was mainly on nonporous materials [10-12]. For porous ceramics, mechanical property investigations have also only been focused on room or high temperature behaviour. Thus, thermal and mechanical properties of the porous ceramics by water-based freeze casting from cryogenic to room temperatures were investigated in this work.

**Section 2** describes the state of the art of this research work, which covers the cryogenic engineering materials, thermal and mechanical properties of porous ceramics and preparation methods of macroporous structure, etc. The section 2.1 describes the materials for cryogenic engineering such as aerospace applications and superconductivity fields. The materials have to withstand harsh working environments for such applications. Porous metallic wicks for capillary transport in aerospace application are focused on propellant acquisition devices and heat pipes. Comparing to porous metal materials, porous ceramics generally have lower density, higher corrosive resistance, higher mechanical strength and higher thermal stability, which can be potential substitution materials for metals. Thermal and mechanical properties of ceramics are normally greatly influenced by environmental temperature. Due to the difference between porous and dense materials, there are quite a few theories being proposed for determining the thresholds of thermal properties, such as parallel and series models, Maxwell-Eucken and Effective Medium Theory [13], which are described in section 2.2. The factors influencing the mechanical properties, such as porosity, anisotropy or temperatures are discussed in section 2.3. The macroporous structures, in terms of pore size, shape, porosity can be designed by various methods according to a specific application. In section 2.4, different kinds of strategies to prepare macroporous ceramics are introduced and freeze casting method as well as its resultant structure is emphasized. The wide applications of polymer derived ceramics due to its low processing temperature and cost, tailorable surface characteristics and plastic processing technologies for producing different shapes are discussed in section 2.5.

**Section 3** describes the aim of the work and approach.

**Section 4** provides the background of the characterization methods used in this work, which includes characterizing the fillers as well as final porous SiOC monoliths.

**Section 5** discusses the preparation of porous PDCs by using H44 as the precursor in water-based freeze casting method. The hydrophobic precursor was modified by thermal decomposition at 600 °C to get hydrophilic H44-derived filler, which was applied later in water. The influence of process parameters on pore size and the specific surface areas and surface

characteristics was investigated. The solid loading of 30–40wt% resulted in crack free monoliths, and freeze temperature of -150 °C and -80 °C resulted in the desired pore sizes for capillary transport of cryogenic liquids.

**Section 6** describes using MK as the precursor in water-based freeze casting to prepare porous SiOC monoliths. This precursor cannot be converted to hydrophilic fillers by thermal decomposition, therefore, APTES was used to modify the surface characteristics, and a further thermal decomposition was needed to get the hydrophilic filler applicable for water-based freeze casting. The influence of MK: APTES ratio as well as the thermal treatment temperatures on the wettability and suspension stability of fillers was investigated.

The monolith structure prepared with both H44 and MK had similar porous structure; however, the mechanical properties and thermal properties may differ. Therefore, in **section 7**, those properties of both monoliths were investigated, especially at cryogenic temperatures, either inside liquid nitrogen or vacuumed chamber cooled by liquid nitrogen or argon.

### References

- [1] R. Radebaugh, *Cryogenics*, The MacMillan Encyclopedia of Chemistry, 2002, New York.
- [2] R. G. Ross, *Aerospace coolers: A 50-year quest for long-life cryogenic cooling in space*, Cryogenic Engineering, ISBN 978-0-387-33324-3, Springer, 2007, New York.
- [3] C. Buzea, T. Yamashita, Review of the superconducting properties of MgB<sub>2</sub>, *Supercond. Sci. Technol.* 14 (2001) R115–R146.
- [4] J. W. Hartwig, *Liquid acquisition devices for advanced in-space cryogenic propulsion systems*, ISBN: 978-0-12-803989-2, Elsevier Inc., 2016, London.
- [5] N. Fries, K. Odic, M. Conrath, M. Dreyer, The effect of evaporation on the wicking of liquids into a metallic weave, *J. Colloid Interface Sci.* 321 (2008) 118–129.
- [6] Y. Grebenyuk, M. Dreyer, Wicking of liquid nitrogen into superheated porous structures, *Cryogenics* 78 (2016) 27–39.
- [7] P. Colombo, G. Mera, R. Riedel, G. D. Sorarù, Polymer-derived ceramics: 40 years of research and innovation in advanced ceramics, *J. Am. Ceram. Soc.* 93 (2010) 1805–1837.
- [8] M. Naviroj, S. M. Miller, P. Colombo, K. T. Faber, Directionally aligned macroporous SiOC via freeze casting of preceramic polymers, *J. Eur. Ceram. Soc.* 35 (2015) 2225–2232.
- [9] B. H. Yoon, E. J. Lee, H. E. Kim, Highly aligned porous silicon carbide ceramics by freezing polycarbosilane/camphene solution, *J. Am. Ceram. Soc.* 90 (2007) 1753–1759.
- [10] E. Volkmann, K. Tushtev, D. Koch, C. Wilhelmi, J. Göring, K. Rezwan, Assessment of three oxide/oxide ceramic matrix composites: Mechanical performance and effects of heat treatments, *Composites Part A* 68 (2015) 19–28.
- [11] X. R. Ren, W. Pan, Mechanical properties of high-temperature-degraded yttria-stabilized zirconia, *Acta Mater.* 69 (2014) 397–406.

[12] Q. Z. Chen, J. L. Xu, L. G. Yu, X. Y. Fang, K. A. Khor, Spark plasma sintering of sol–gel derived 45S5 Bioglass®-ceramics: Mechanical properties and biocompatibility evaluation, *Mater. Sci. Eng. C* 32 (2012) 494–502.

[13] L. L. Gong, Y. H. Wang, X. D. Cheng, R. F. Zhang, H. P. Zhang, Thermal conductivity of highly porous mullite materials, *Int. J. Heat Mass Transfer* 67 (2013) 253–259.

## 2. State of the art

### 2.1 Materials for cryogenic engineering and requirements for their applications

#### 2.1.1 Materials for cryogenic engineering

Different kinds of materials are used in the cryogenic engineering: metal, ceramics, polymer or composite materials. Materials are selected considering the unique operating environments of cryogenic engineering, including extremes of temperature, close dimensional tolerances, and radiation exposures, etc [1]. Reliability is of great importance, due to the fact that these materials are often inaccessible for inspection or repair and their performance is crucial during the entire life cycle of the device.

In these applications, cryogenic materials are used as support structures, vessels, or electrical insulation, etc. The components and its required properties are listed in Table 2.1.

Table: 2.1 Materials for components in cryogenic applications and their required properties [1].

Support elements	Vessels	Electrical insulation
Struts (compression)	Cryostats	Turn insulation
Straps (tension)	Pressure vessels	Layer insulation
Critical material properties		
Tensile strength	Thermal conductivity	Through thickness properties
Tensile modulus	Tensile strength	• Shear strength
Compressive strength	Tensile modulus	• Shear/compressive strength
Compressive modulus	Thermal conductivity	• Compressive strength
Thermal conductivity	Permeability	Fatigue
Thermal expansion	Fatigue	Electrical strength
Fatigue		Thermal expansion
Radiation effects		Thermal conductivity
		Fabrication
		Radiation effects

In the aerospace applications, structural components, such as liquid hydrogen-oxygen rocket engine bearings are made from  $\text{Si}_3\text{N}_4$ , which is chosen because it is 30 percent harder and 40 percent lighter than steel [2]. Epoxy based materials are often used in the cryogenic fuel tanks due to its high specific strength and stiffness, low curing shrinkage and good chemical and corrosion resistances [3]. The telescopes in infrared astronomical space telescope missions are usually cooled to cryogenic temperature in order to achieve high sensitivity. SiC based materials have a high ratio of stiffness over mass, high thermal conductivity, and high tolerance against the impact of energetic particle [4]. Therefore, the mirrors of the ASTRO-F telescope are made of sandwich-type silicon carbide (SiC) materials, comprising a porous core and a chemical-

vapor-deposited coat of SiC on the surface. The optical performance of SiC at cryogenic temperatures has been investigated [5].

The electrical resistance of most metals decreases as temperature decreases. Certain metals lose all electrical resistance below some transition temperature and become superconductors. For example, bulk metallic glass (BMGs) possess ultrahigh strength, super-elasticity, high resistance to corrosion, and good fatigue characteristics, and a few materials also exhibit superconductivity at low temperature and good magnetic properties [6]. Powerful superconducting electromagnets are used in maglev trains, magnetic resonance imaging (MRI), nuclear magnetic resonance (NMR), magnetic confinement fusion reactors (e.g. tokamaks) and beam-steering and focusing magnets used in particle accelerators etc. In nuclear fusion energy applications, the fusion systems require the reacting plasma to be confined by magnetic fields. If such magnets were conventional, such as water-cooled copper magnets, they would consume all or most of the reactor power output, therefore, the fusion reactors must use either cryogenically cooled or superconducting coils [7]. Cryogenics will also be essential for all the fuel cycling from cryo-pumping to the isotope separation and clean-up of the plasma exhaust gas. Furthermore, the peripheral components for heating and refueling, such as neutral and pellet injection also need cryogenics, etc. The requirements for the superconducting coils will be the main important issue for cryogenic systems for fusion [8]. Dyneema fiber (polyethylene fiber) reinforced plastics can be used as materials for superconducting coils bobbin. The nitrogen-strengthened steels can be used as structural materials for large coil task (LCT) coil case for the toroidal field [9].

Polymers are used widely in cryogenic applications due to their favorable friction and wear behavior in the absence of external lubrication. For example, polytetrafluoroethylenes (PTFE) are particularly advantageous because they can act as solid lubricants. The use of polymer materials for tribologically stressed systems at cryogenic temperature includes [10]:

- Storage and distribution of refrigerants: pumps, valves, bearing, seals
- Space technology including turbo pump bearings in rocket engines, gyroscopes and moving parts in satellites

### **2.1.2 Cryogenic wicking in porous materials**

Capillary transport (or wicking,) is the ability of a liquid to flow in narrow spaces with capillary forces. In the space, the main issue when dealing with the functionality of spacecraft propellant tanks is the lack of gravity to define which is "up" or "down". Therefore the wicking process is employed to solve the fuel delivery in the liquid-propellant management system for rockets and space vehicles. Wicking process is also vital for the function of heat pipes, which are used as primary elements of thermal control systems for both space and electronics applications [11]. Cryogenic wicking deals with wicking at cryogenic temperature. During the cryogenic wicking

process, there is heat transport as well as mass transport. Therefore not only porous structures, but also thermal properties of the wick materials are very important for this process [11–12].

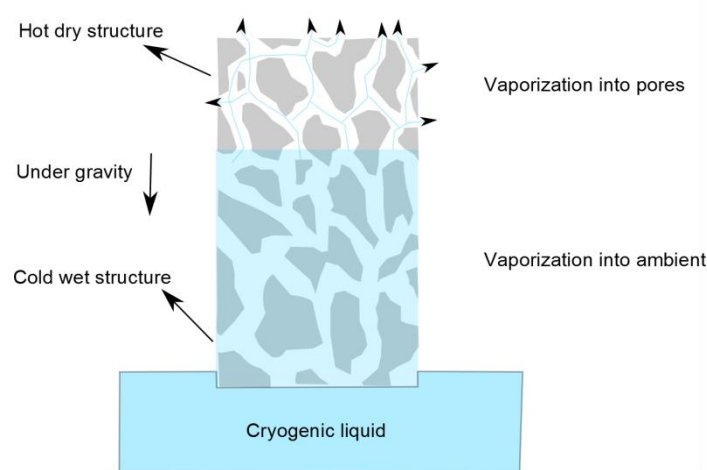


Figure 2.1: Wicking of cryogenic liquid into porous medium under gravity, modified from [12].

Cryogenic fuel delivery in propellant management device (PMD) technology normally uses metallic wicks. One structure of the PMD is shown in Figure 2.2. The PMD includes a network of galleries, made of porous screens running through it, which provide the gas free propellant during the mission accelerations [13]. The porous structure influences the permeability, accordingly pumping ability, and the pore size for this cryogenic wicking are normally tens of micrometers [12,14,15]. For example, Symones [14] investigated the influence of metallic wicks (Dutch Twilled Weave) with different mesh sizes (largest size 20×250, smallest 325×2300, that is, 166  $\mu\text{m}$  and 10  $\mu\text{m}$ ) on its wicking behavior and Fries et al. [16] published their wicking investigation using same metallic waves (200×1400, 14  $\mu\text{m}$ , porosity 33%) related to PMD application.

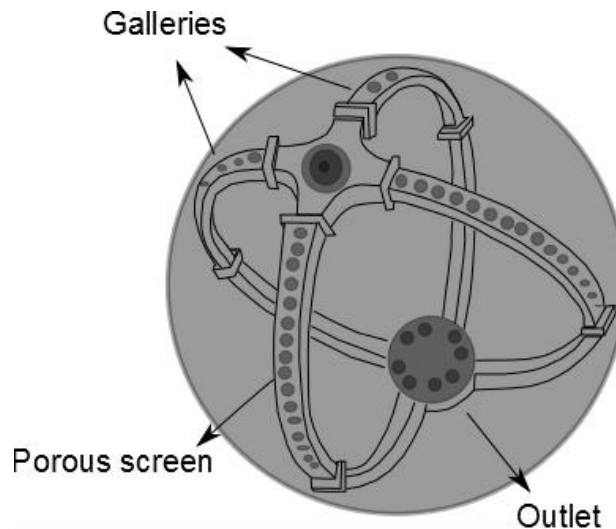


Figure 2.2: Propellant management devices [13].

Loop heat pipe (LHP) is a high efficient two-phase heat transfer device with a capillary wick in the evaporator to circulate the working fluid. One structure of LHPs is shown in Figure 2.3. Khrustalev et al. reported cooling behavior of cryogenic loop heat pipes with a temperature range from 65K to 140K, using liquid oxygen as a working fluid and stainless steels as wick materials (density 7480–8000 kg/m<sup>3</sup>, pore radius 2.4 μm, wick permeability  $5 \times 10^{-14}$  m<sup>2</sup>) [17]. Zhang et al. investigated metallic mesh structure (4 stacked layers, pore size 5 μm) used for cryogenic wicking of liquid nitrogen, liquid helium and liquid oxygen, etc. [18]. For the thermal management, LHPs can be used to control the temperature by precise adjustment of thermal conductivity.

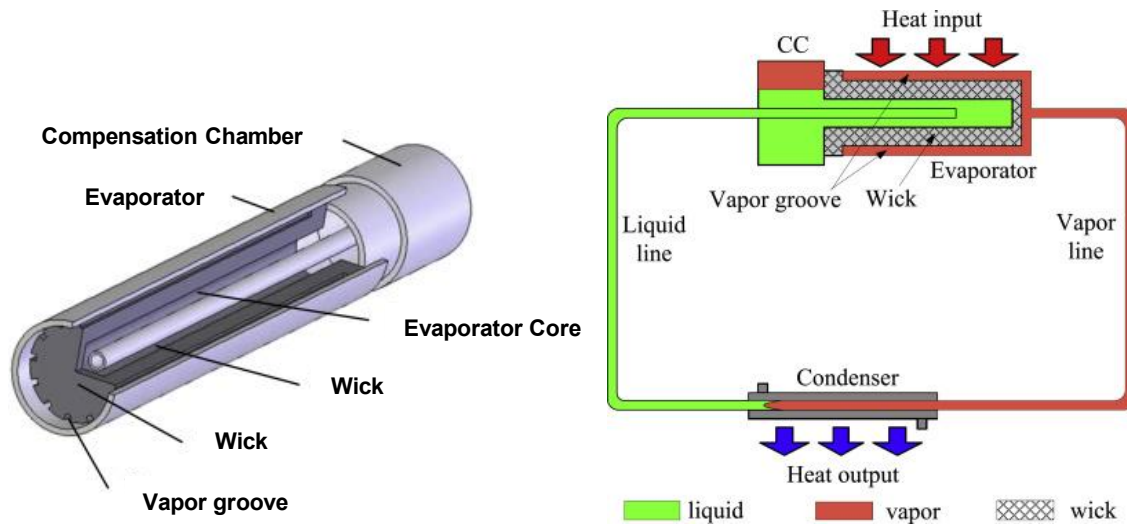


Figure 2.3: Structure of evaporator and compensation chamber and schematic of a LHP, modified from [19].

For both propellant delivery and heat pipes applications, the wicks have direct contact with cryogenic liquid; therefore, metallic wicks are more prone to have corrosion. Besides, the density of metal is contradicting to light weight design of aerospace applications. There are ceramic heat pipe wicks, such as silicon dioxide/aluminum wick [20]; however, most of them are used at high temperature, due to the fact that metallic wicks cannot work properly above 800 °C, especially in corrosive and harsh environment [21]. Therefore, wicking performance of ceramics, such as glass frits [12, 15] began to draw attention for cryogenic wicking. Ceramics have the advantage of high strength, low density, high corrosive resistance and low thermal conductivity [22]. However, the pore size range and the monolith size required for cryogenic wicking proposed a great challenge for fabrication. Additionally, the thermal and mechanical properties of such porous ceramics also need to be investigated.



## 2.2 Thermal properties of porous ceramics

### 2.2.1 Thermal conductivity, thermal expansion and specific heat capacity of ceramics

Materials of high thermal conductivity are widely used in heat sink applications while materials of low thermal conductivity are used as thermal isolation. Most of the ceramics have relatively low thermal conductivity compared to metals. Heat is conducted in ceramics by propagation of nonharmonic elastic waves in the medium. The thermal vibrations of the structural units form a propagated wave that transfers the thermal energy through the solid substance in energy quanta is termed as phonon. Thermal conductivity is dictated by the phonon mean free path and the phonon scattering refers to the resistance to heat flow in solid substances [23]. The phonon propagation can be written as:

$$\lambda = \frac{1}{3} \int c(w) \cdot v \cdot l(w) \cdot d(w) \quad (2.1)$$

Where  $c(w)$  is the heat capacity for the frequency interval of lattice vibrations  $w$ , and  $v$  is the mean velocity of the sound,  $l(w)$  is the mean path of the phonons. A few scattering mechanisms contribute to the heat resistance, which is equal to the inverse value of the thermal conductivity. The contribution of thermal resistance includes the interaction of the phonons with the pores, scattering of the phonons on the crystal boundaries, impurities and point defects etc. [23].

Single crystal ceramics have much higher thermal conductivity than ceramics with impurity (foreign atoms) due to phonon scattering caused by atom vacancies. The polycrystalline ceramics also have lower conductivity than single crystal ceramics due to phonon scattering at grain boundaries [24]. Thermal conductivity of non-crystalline solids is several orders of magnitude smaller than that of crystals and is independent of the chemical composition [25]. Temperature has different effects on the thermal conductivity of crystalline solid and vitreous materials, which can be seen from Figure 2.4. The thermal conductivity of crystalline solids increases with temperature rise at cryogenic temperature range; however, decreases with further temperature rise [24, 26]. Thermal conductivity of vitreous materials normally increases with the temperature rise continuously [25, 27].

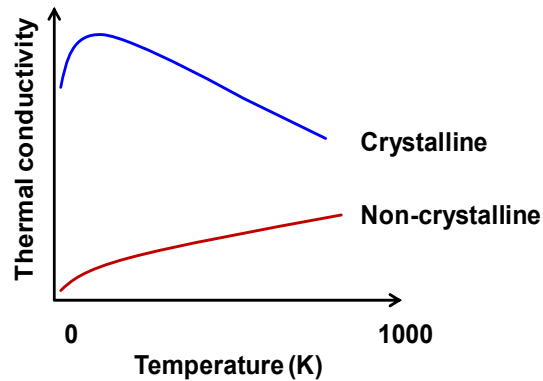


Figure 2.4: Influence of temperature on thermal conductivity of crystalline and non-crystalline solids at different temperature range.

As discussed above, there are several ways to adjust the thermal conductivity, by altering the crystallinity, adding impurities, changing temperatures and increasing the porosity of the structure. For example, yttria stabilized zirconia (YSZ) has one of the lowest thermal conductivities of ceramics at elevated temperature ( $\sim 2.3 \text{ W}\cdot\text{m}^{-1}\cdot\text{K}^{-1}$  at  $1000^\circ\text{C}$  for a fully dense material) due to its high concentration of point defects (oxygen vacancies and substitutional solute atoms), which scatters heat-conducting phonons. This material is therefore used as the ceramic coating in thermal barrier coating [28].

Most of ceramics show positive thermal expansion, that is, the volume expands as the temperature rises. There are also some materials showing negative thermal expansion, such as cubic zirconium tungstate [29]. Near zero thermal expansion materials are normally composite materials [30].  $\text{Al}_2\text{TiO}_5\text{-ZrTiO}_4\text{-ZrO}_2$  composites showed coefficient of thermal expansion (CTE) as low as  $-2 \times 10^{-6} \text{ K}^{-1}$  [31]. Controlling thermal expansion of ceramics is very important for the structural components, especially for the precise aerospace applications. There are several factors influencing CTEs, such as crystallinity, temperature, compositions etc. Regarding crystallinity influencing thermal expansion, for example, close-packed crystalline structure of sodium chloride tends to have high expansions, while materials of less symmetrical structures, such as zircon ( $\text{ZrSiO}_4$ ) or willemite ( $\text{Zn}_2\text{SiO}_4$ ) tend to have low thermal expansion [32]. The vitreous silica has a much lower thermal expansion, in which thermal expansion can only change due to silicon-oxygen distance, while the thermal expansion in silica of crystalline types can be induced by cooperative rotations in the crystalline network, contributing to higher thermal expansion [33]. However, fused mullite showed slightly higher thermal expansion than crystalline mullite [34]. The open porosity generally has no influence on the CTE. For example, Coble et al. reported that CTEs were the same when the porosity of sintered alumina changed from 4% to 49%, however, it changed from  $5.4 \times 10^{-6} \text{ K}^{-1}$  to  $9.7 \times 10^{-6} \text{ K}^{-1}$  when the temperature changed from  $25^\circ\text{C}$  to  $1200^\circ\text{C}$  [35].

Specific heat capacity ( $C_p$ ) of pure ceramics are contributed by the lattice vibrations (phonons and localized modes), and impurities slightly influence the specific heat capacity [36]. Specific heat capacity of crystalline materials can be calculated roughly by the Einstein-Debye relationship; however, it cannot be applied to vitreous materials [37]. The influence of crystallinity on the specific heat capacity is considered as small [25]. Specific heat capacity changes with composition as well as temperature. In general, the specific heat of a material constituted of different solid phases can be calculated using the rule of mixtures [38]. Specific heat capacity rises with temperature dramatically below the Debye temperature and obeys the Debye law (2.2) at temperatures below  $10^{-2}\theta$ , where  $\theta$  is the Debye temperature and  $c$  is a constant [39–40]. When the temperature increased further, the influence of temperature on specific heat capacity is less significant. The influence of temperature on the specific heat capacity of one polymorph of SiC (4H-SiC) can be seen from Figure 2.5.

$$C_v = cT^3 \quad (2.2)$$

Materials of different phases (polymorphs) also have different specific heat capacity, for example 6H-SiC has higher specific heat capacity than 4H-SiC and polycrystalline SiC [41].

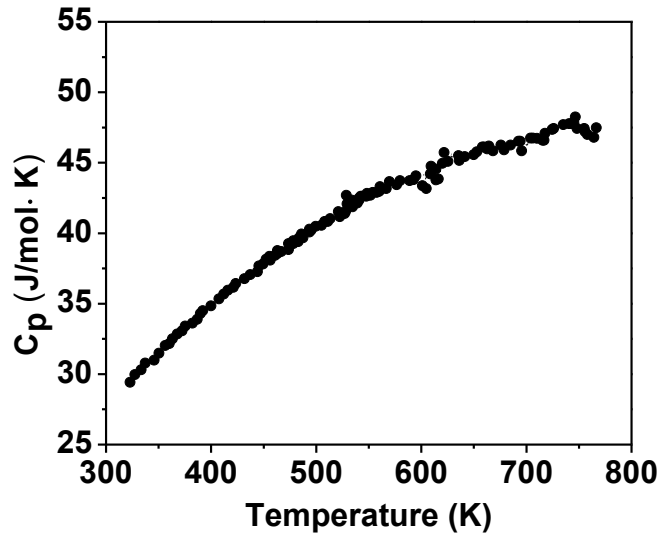


Figure 2.5:  $C_p/T$  plot of monocrystalline 4H-SiC from 300K to 800 K [41].

### 2.2.2 Thermal properties of porous ceramics

As discussed in 2.2.1, thermal properties of porous ceramics differ from dense ceramics mainly in thermal conductivity; whereas thermal expansion coefficient and specific heat capacity are not influenced. Porous structure affects thermal conductivity via pore size, porosity and anisotropy, etc. Porous ceramics can be seen as a heterogeneous system made of gas (pore) and dense ceramics (solid).

To understand the influence of pore size on thermal conductivity, it is important to know that thermal conductivity of a porous (cellular) material is comprised of four parts: conduction through the solid  $\lambda_s^*$ , conduction through the gas  $\lambda_g^*$ , convection within the cells  $\lambda_c^*$  and radiation through the cell walls and across the cell voids  $\lambda_r^*$ , as shown in the following equation [42]:

$$\lambda^* = \lambda_s^* + \lambda_g^* + \lambda_c^* + \lambda_r^* \quad (2.3)$$

The solid contribution is normally significantly higher than that of the gas contained in the pores, which is negligible. The convection contribution largely depends on the cell size, and it is negligible when the cells are small than 3–4 mm. The radiation contribution is highly dependent on the porosity, pore size, and temperature [43]. One example of the radiation contribution can be seen from work of Francl et al., in which the thermal conductivity of alumina with cylindrical pore sizes of 1.46 and 0.82 mm were investigated at 400 and 800 °C. Thermal conductivity of both materials is the same at 400 °C, however, thermal conductivity of porous alumina with a pore size of 1.46 mm is slightly higher than that of 0.82 mm at 800 °C [44].

There are a few theories proposed to understand the influence of porosity on thermal conductivity. Series model and Parallel models serve as lower and upper bounds for effective conductivity [45–46]:

$$\text{Series model: } k_e = \frac{1}{(1 - v_2)/k_1 + v_2/k_2} \quad (2.4)$$

$$\text{Parallel model: } k_e = (1 - v_2)k_1 + v_2k_2 \quad (2.5)$$

in which  $v_1$ ,  $v_2$ , and  $k_1$ ,  $k_2$  represent the volume fraction and thermal conductivity of pores and solid materials, respectively.

Two forms of Maxwell-Eucken model give much narrower boundaries than Series and Parallel models [46].

$$\text{Maxwell - Eucken 1: } k_e = k_1 \frac{2k_1 + k_2 - 2(k_1 - k_2)v_2}{2k_1 + k_2 + (k_1 - k_2)v_2} \quad (2.6)$$

$$\text{Maxwell - Eucken 2: } k_e = k_2 \frac{2k_2 + k_1 - 2(k_2 - k_1)(1 - v_2)}{2k_2 + k_1 + (k_2 - k_1)(1 - v_2)} \quad (2.7)$$

The Effective Medium Theory (EMT) equation can be used to describe the relation between thermal conductivity and porosity in a structure, where pores are distributed randomly [46–47]:

$$k_e = \frac{1}{4} \left\{ (3v_2 - 1)k_2 + (3v_1 - 1)k_1 + [((3v_2 - 1) + (3v_1 - 1)k_1)^2 + 8k_1k_2]^{\frac{1}{2}} \right\} \quad (2.8)$$

Gong et al. reported the thermal conductivity of highly porous mullite materials and compared it with Parallel model, Series model, EMT and Maxwell-Eucken 1 and Maxwell-Eucken 2. The

experimental results fall in the boundaries defined by these theories [48], which can be seen from Figure 2.6. In this figure, the porosity is divided into two categories: internal porosity (foams, sponges) and external porosity (granular or particulate materials). Smith et al. reported that the Maxwell-Eucken relation can be used for closed porosity and EMT (Landauer relation) for open porous structures when the porosity of alumina and zirconia ceramics is lower than 65%. For porosity higher than 65% Maxwell-Eucken (Hashin Shtrikmann upper bound) and Russell's relation described well the relation of thermal conductivity and the porosity in case of kaolin-based foams and calcium aluminate foam ceramics [49].

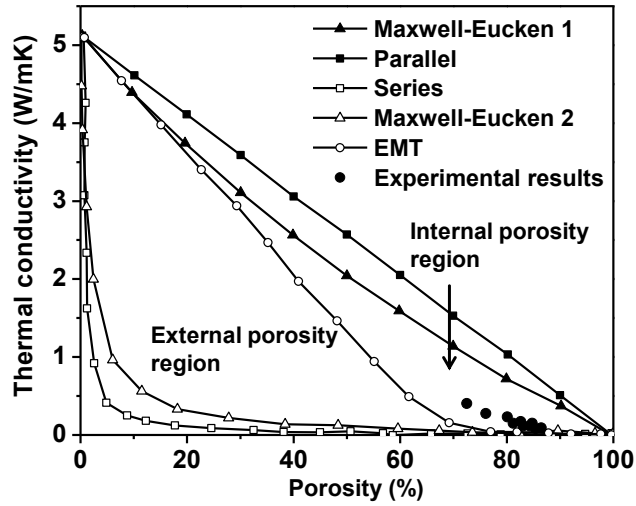


Figure 2.6: Thermal conductivity of porous mullite as a function of porosity for the experimental data, theoretical curves, modified from [48].

Anisotropic structure, such as biomorphous SiC prepared by using woods as templates or cylindrical pores made by freeze casting, also influences the thermal conductivity. Heat prefers to transfer within the continuous solid path than within the voids, which acts as heat deflection points. Franci reported that Leob equation can give relative accurate results for both isometric pores and cylindrical pores [44]. The Leob equation is composed as the following:

$$k_p = k_{solid} \left[ (1 - P_0) + \frac{p_0}{\frac{P_L k_s}{4\sigma\epsilon\gamma d T_m^3} + (1 - p_L)} \right] \quad (2.9)$$

Where  $k_{solid}$  is the conductivity of the solid with no porosity,  $p_0$  is the cross-sectional pore fraction,  $p_L$  is the longitudinal pore fraction,  $\sigma$  is the radiation constant,  $\epsilon$  is the emissivity,  $\gamma$  is the geometrical pore factor,  $d$  is the dimension of pore and  $T_m$  is the mean absolute temperature.

Pappacena et al proposed that in the axial direction for cylindrical pores, the thermal conductivity can be calculated by [43]:

$$k_{solid,axial}^* = (1 - p)k_{solid} \quad (2.10)$$

where  $p$  is the porosity of the material. In the transverse direction (heat flow is perpendicular to the pores), the thermal conductivity can be calculated by [43]:

$$k_{solid,transverse}^* = k_{solid} \left(1 - \left[\left(\frac{4}{\pi}\right)p\right]^{0.5}\right) \quad (2.11)$$

## 2.3 Mechanical properties of porous ceramics

### 2.3.1 Mechanical properties of ceramics

Ceramics are brittle materials, however still widely used in industry applications, due to the high hardness, high corrosive resistance, etc. The reasons for the low ductility of ceramics are mainly due to the low manoeuvrability and mobility of dislocation (line defects), which leads to very low plastic deformation of ceramics [23]. In ceramics, the grain boundaries have lower strength, which decrease the strength of polycrystalline materials compared to single crystalline materials and pores (cracks) can decrease the strength further. Fracture begins with crack nucleation and then propagates. The influence of crack size on the strength can be seen from Griffith equation:

$$\sigma_{Griffith} = \sqrt{\frac{2\gamma_0 E}{kl}} \quad (2.12)$$

Where  $l$  is the crack size,  $\gamma_0$  is the surface energy,  $E$  is the elastic modulus, and  $k$  is a dimensionless term related to crack and sample geometry.

The strength of samples is size-dependent, because the probability of finding a big crack in large volume samples is much higher than in a small volume sample. Tensile strength is much less comparing to bending strength, considering tensile stress is applied in the whole body and bending stress is applied in a thin region. Cracks in ceramics under compression are more difficult to open and propagate due to low ductility, leading to high compressive strength. Weibull's statistical theory of strength (Two-parameter Weibull distribution) can be used to quantitatively describe the relation between fracture probability ( $P_w$ ) and volume ( $V$ ):

$$P_w(\sigma, W) = 1 - \exp(-KV\sigma^m) \quad (2.13)$$

Where  $K$  and  $m$  are material constants and  $m$  is termed as Weibull modulus. To predict the probability of failure for a given stress ( $\sigma$ ), the Weibull plot can be rewritten as:

$$P_w(\sigma, W) = 1 - \exp\left[-\left(\frac{\sigma}{\sigma_0}\right)^m\right] \quad (2.14)$$

where  $\sigma_0$  is the characteristic strength where  $P_w = 0.632$ .

Depending on the specific applications, different kinds of mechanical properties of ceramics are focused, such as creep behaviors, thermal shock resistance, bending strength, compressive strength or fracture toughness, etc. In the wicking applications, the compressive strength is of greater importance than other properties, therefore in this work only the compressive strength of ceramics is considered.

### 2.3.2 Compressive strength of porous materials

Pores in ceramics can be seen as cracks; therefore, the compressive strength is greatly influenced by the pore size, porosity and anisotropy.

The influence of pore size on compressive strength can be understood by Griffith equation (2.12), the compressive strength generally decreases with the increase of pore size. Liu investigated compressive strength of porous hydroxyapatite ceramics of different pore sizes: 0.093 mm, 0.188 mm, 0.42 mm. The influence of pore size on compressive is more substantial at lower porosity (47%) than at higher porosity (64.3%), as shown in Figure 2.7 [50].

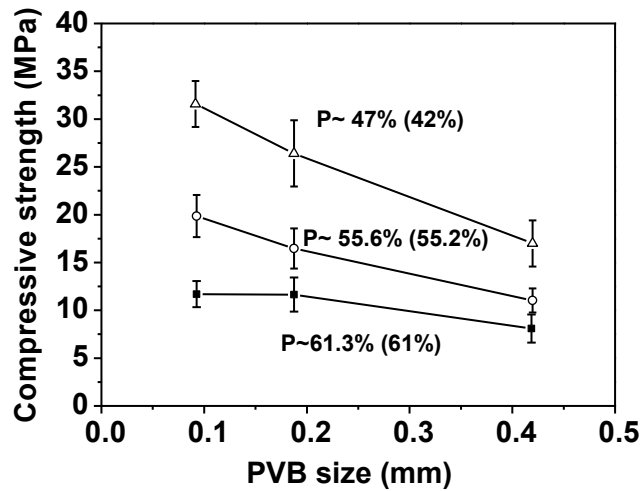


Figure 2.7: Influence of pore size on compressive strength at different porosity [50].

In cellular materials, the influence of porosity on compressive strength can be seen from Ash y's theory (2.15), which describes the relation between strength and bulk density [42]. Total porosity is the reciprocal of relative density (2.16).

$$\frac{\sigma}{\sigma_s} = C \left( \frac{\rho}{\rho_s} \right)^m \quad (2.15)$$

$$p_t = 1 - \frac{\rho}{\rho_s} \quad (2.16)$$

Where  $C$  is a dimensionless constant and the exponent  $m$  is '1.5' or '2', depending on whether the cell morphology is open cell or closed cell.  $\rho$  is the density of porous

material, and  $\rho_s$  is the density of the solid material. An increase in the relative density (a decrease in porosity) leads to thicker walls, therefore higher strength. Compressive strength of silicon oxycarbide ceramic foams made from direct foaming increased from  $1.31 \pm 0.59$  MPa to  $9.9 \pm 1.78$  MPa when the relative density is increased from 10% to 25% [51]. Additionally, there are quite a few empirical models for compressive strength-porosity relation, such as Ryshkewitch model, Schiller model, Balshin model and Hasselman model [52–53]. Chen et al. investigated the influence of porosity on compressive strength of cement mortar and compared the results with the above mentioned models, as shown in Figure 2.8 [53]. Besides, the dependency of compressive strength of porous ceramics on porosity can also be estimated by the method based on minimum solid area approach [54]:

$$\sigma = \sigma_s \exp(-bp_t) \quad (2.17)$$

Where  $b$  is related directly to the pore characteristics, and  $p_t$  is the porosity.

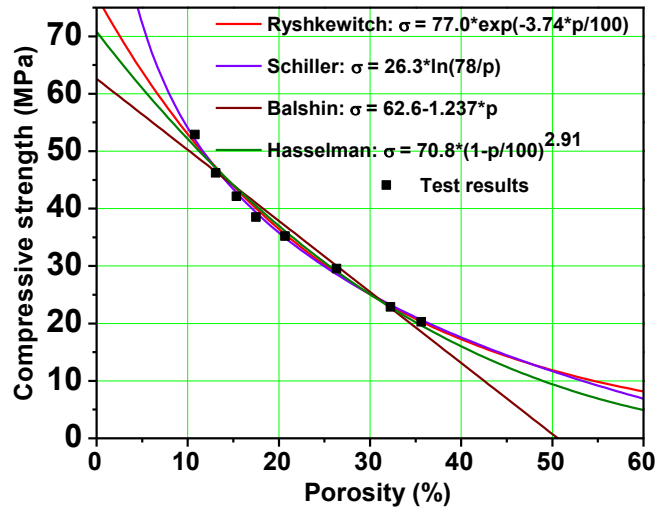


Figure 2.8: Compressive strength of porous cement mortar and fittings by different theories, modified from [53].

In case of anisotropic materials, the compressive strength in different directions is different. Compressive strength can also be estimated by Ashby theory described by (2.15), in which  $m$  is '2' for transverse direction (perpendicular to longitude pore) and is '1' for the longitudinal direction [42], which means that the compressive strength is linearly related to the apparent density. Hing et al. investigated compressive strength of anisotropic and isotropic porous hydroxyapatite materials, and found that the increase of apparent density resulted in linearly



increase of ultimate compressive stress for anisotropic specimens in longitudinal direction and non-linearly increase (quadratic) for isotropic porous specimens [55].

### **2.2.3 Compressive strength of ceramics at cryogenic temperatures**

Ceramics have generally low thermal expansion, however, when a huge temperature change happens, thermal stress is created inside the structure. Especially for hybrid materials, like concrete, a temperature change generates different thermal expansions between components resulting in cracks and stress inside the ceramic, which influences the compressive strength greatly. Ceramics show a certain degree of plastic behavior at a temperature close to its melting temperature. For example, Barsoum et al. reported that the  $Ti_3SiC_2$  had a compressive strength of 600 MPa at room temperature and 260 MPa at 1300 °C (certain plasticity) [56]. Cryogenic temperatures influence the compressive strength mainly in three ways. In the first way, atom distances in ceramics get short at low temperature, which results in increased interaction between the atoms, leading to high strength. In the second way, the cryogenic temperature induces stress in the sample and can therefore lead to a phase transformation. For example, stress induces a phase transformation of  $CeO_2$  stabilized  $ZrO_2$  from tetragonal to monoclinic phase at cryogenic temperature, which leads to an increase of compressive strength [57]. In the third way, the crack propagation path changes at low temperature. At 77 K, more intergranular crack propagation happens than transgranular propagation inside  $Si_3N_4$ , which leads to an increased fracture toughness, positively related with strength [58].

In this work, compressive strength of SiOC porous materials are investigated, and more details of the influence of cryogenic temperature on compressive strength can be found in Chapter 7.

## **2.4 Design of macroporous ceramics for different applications**

### **2.4.1 Fabrication of macroporous structure**

Macroporous materials refer to materials with pore size larger than 50 nm. „Macroporous ceramics with pore size range from 400 nm to 4 mm and porosity within the range 20–97% have been produced for a number of well-established and emerging applications, such as molten metal filtration, catalysis, refractory insulation, and hot gas filtration” [59]. There are a few methods to get the macroporous structure: partial sintering, replica methods, sacrificial template methods, direct foaming methods and additive methods. The principles of some methods are shown in figure 2.9.

## 2. State of the art

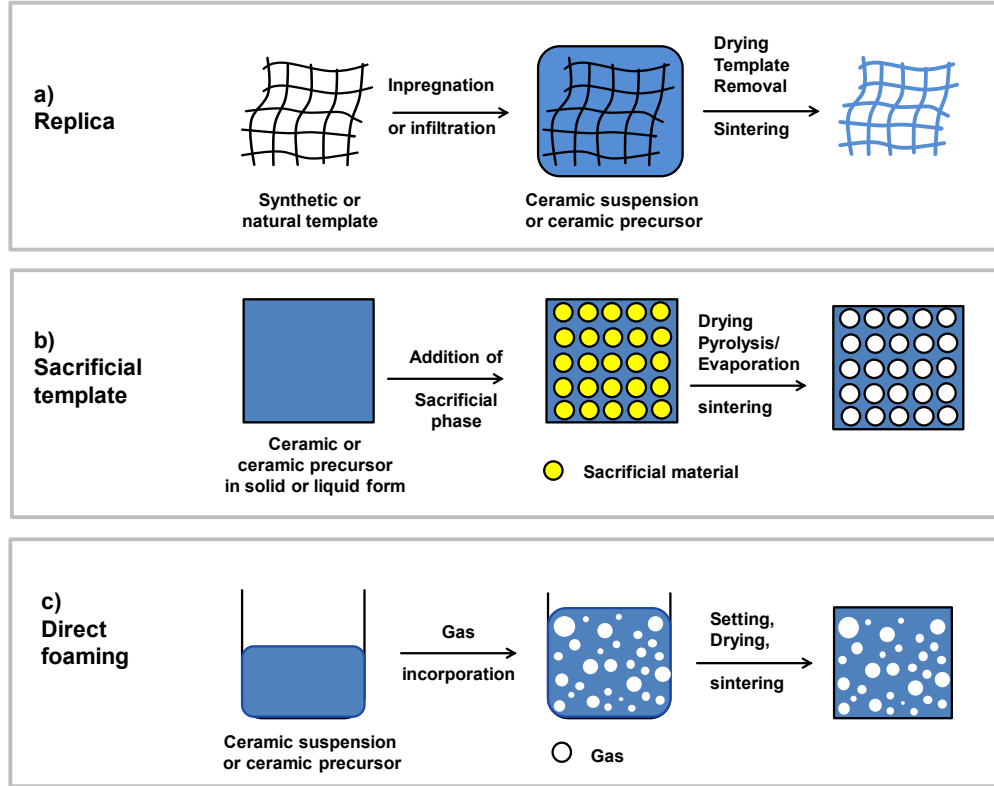


Figure 2.9: Scheme of possible processing routes used for producing macroporous ceramics, modified from [59].

Partial sintering of powders leads to macroporous structure, which is the simplest method to prepare the macroporous structure. The initial particle size as well as the heating rate influences the pore size and porosity greatly. However, the porosity prepared by this method is relatively low. Therefore other methods were developed to fabricate porous structure in more controllable way.

In 1961, Schwarzwaldner and Sommer firstly used polymeric sponges as templates to prepare cellular ceramics [60]. An open-celled sponge is first immersed in ceramic slurry, after that excess slurry is removed from the sponge, then volatile slurry constituents are evaporated by low temperature treatment, followed by a firing process. During the firing process, the polymeric sponges are burned out, which leaves only the skeleton made of ceramics. The obtained cellular ceramic has the same morphology as the replica template. Polyurethane foams are often used as the polymeric sponges, other natural templates, such as coral, wood, etc. have also been used to prepare cellular ceramics of different morphologies. The cellular structure prepared by this method has hollow struts as shown by Figure 2.10 [61]. These hollow structures are often cracked during pyrolysis of the polymeric template and degrade the mechanical strength of porous ceramics greatly. The pore size range prepared by replica method using polymeric sponge ranged from 200  $\mu\text{m}$  to 3 mm and the porosity can be from 40% to 95%. Further reduction of pore size is difficulty due to limited impregnating polymeric sponges

with slurry. It is very important that the ceramic slurry shows shear-thinning behavior to guarantee it is partially removable under shearing condition and avoid dripping at the same time. Infiltration of ceramic precursors into wood instead of impregnating can further reduce the pore size further, as low as 10  $\mu\text{m}$ ; the obtained porous structures possess anisotropic pores. In case of corals as templates, they are removed by leaching using strong acidic solution. To duplicate the structure of templates instead of hollow struts, replamineform method (replicated life forms) can be applied [62]. During replamineform process, wax is used to coat the templates under vacuum, and after hardening, the template is removed. Then the 'reverse' template is impregnated with ceramic slurry, and wax can be removed by melting. Biocompatible ceramic structures for bone replacement were often prepared in this way.

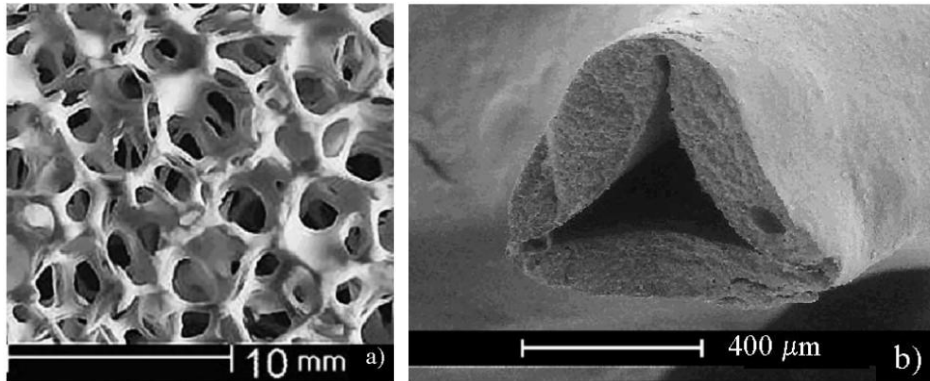


Figure 2.10: a) Cellular ceramics prepared by replica method, b) a hollow strut of cellular ceramics [61].

Unlike replica methods, porous structures made from sacrificial templates are 'negative' replica of template structure. To get porous structure, a biphasic composite made of sacrificial phase and continuous matrix is made. The simplest way to prepare biphasic composite is pressing the homogenized mixture of sacrificial template and ceramic precursor powders [63] or filtrating packed sacrificial templates [64]. The commonly used sacrificial templates include synthetic organic templates including polystyrene beads (PS beads), poly(methyl methacrylate) beads (PMMA beads) and polyvinyl alcohol (PVA beads) [59] and natural organics like gelatin, alginate and starch. Salts can also be used as template, such as sodium chloride [65]. The biphasic composite can also be prepared by forming a two phase suspension followed by a solidification process, such as freeze casting [66], emulsion based sol-gel process [67] or phase separation accompanied sol-gel process [68].

Freeze casting refers to freezing a liquid suspension or solution containing ceramic powders or ceramic precursors to get a porous structure, which is the negative replica of solvent crystals. Freeze casting produces high permeability and near-net shape products. During freezing process, the solvent crystals grow along the imposed temperature gradient, therefore, particles or precursors are rejected from the freezing front to form the wall structure. Based on this, it can be divided into suspension based freeze casting (particles are rejected) and solution based

freeze casting (thermally induced phase separation). The whole freeze casting process can be divided into four steps: 1) Preparation of the slurry, 2) Controlled solidification of the slurry, 3) Sublimation of the solvent, 4) Sintering or densification of the green body [66]. The pore structure is the replica of the solvent crystals. The scheme of freeze casting is shown in Figure 2.11.

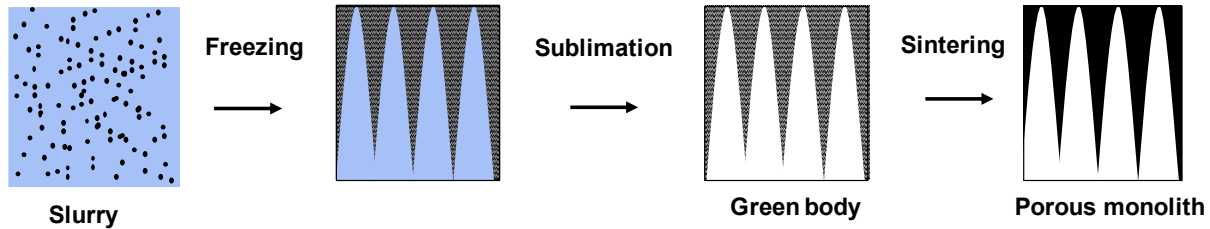


Figure 2.11: The scheme of freeze casting process.

During the slurry preparation, moderate solid loadings are required, too less solid loading leads to cracks in the sample and too high solid loading leads to inhomogeneity (porosity and density gradient) of samples. The porosity is mainly determined by the volume ratio of frozen solvent in the green body and porosity from 25 to 90 % can be obtained by this method. The particle size also influences the fine porous structure. Large particle size results in low stability of the suspension (due to gravitational force), leading to particle sediment. Besides, the large particles also results in less accurate structure of pores. Both inorganic oxides and preceramic polymers can be used in the freeze casting process [63].

The solidification conditions determine mainly the porous structure. Freezing temperature should be lower than melting point of the solvent and freeze rate determines the pore size. High freezing front velocity results in a structure with smaller pores. The freezing front velocity can be influenced by the temperature gradient, viscosity of suspension, particle sizes, etc. Pore sizes prepared from freeze casting range from 1  $\mu\text{m}$  to 100  $\mu\text{m}$ , depending on the freezing rate. The morphology is mainly influence by the solvents used; however, it can be modified by adding additives. The solidification conditions of solvents and its corresponding structure can be seen in Table 2.2 and some typical structures are shown in Figure 2.12.

Table: 2.2 Solvents and its corresponding porous structure in freeze casting.

Solvents (+Additive)	Solidification conditions	Morphology
Water	$< 0^{\circ}\text{C}$	Lamellae
Camphene [69]	$< 40^{\circ}\text{C}$	Dendritic pores
<i>Tert</i> -butyl alcohol [70]	$< 25^{\circ}\text{C}$	Prismatic channels
Cyclohexane [69]	$< 6^{\circ}\text{C}$	Dendritic pores
Water (10wt% sucrose) [71]	$< 0^{\circ}\text{C}$	Cellular
Water + <i>Tert</i> -butyl alcohol [72]	$< 0^{\circ}\text{C}$ , depending on additive	Lamellar, snowflake, dendritic,

## 2. State of the art

Water (PVA) [73]	concentrations < 0°C, depending on additive concentration	needle-like or prismatic Plate and dendritic pores
------------------	--	---

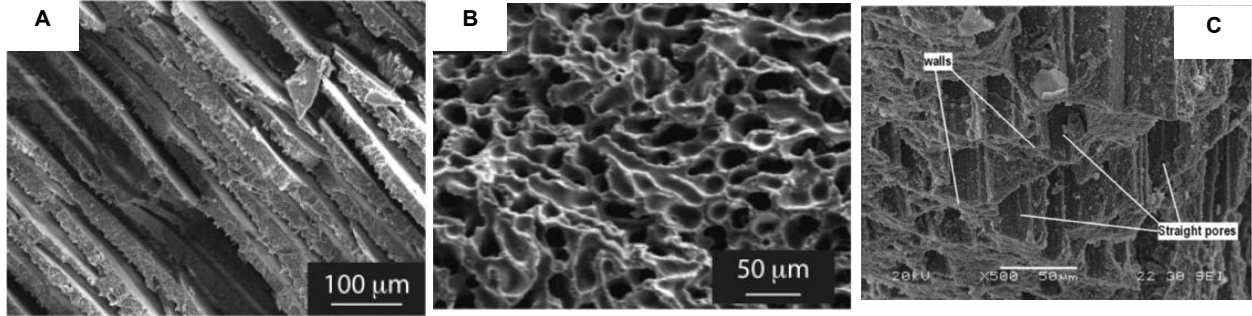


Figure 2.12: some typical structures of freeze casting using water, camphene or tert-butyl alcohol as solvents, alumina as solid phase [70, 74–75].

Unidirectional porous structure can be obtained by anisotropic freezing. The unidirectional freezing gradient can be obtained by using a special instrument, which can control the temperature profile to achieve a steady freezing front velocity, as shown in Figure 2.13. Slurries are frozen in the Teflon mold placed at the top of a cold finger (cooled by liquid nitrogen). A heater placed on the metallic rods and a thermocouple placed on the side of the mold can be used to control the freezing kinetics.

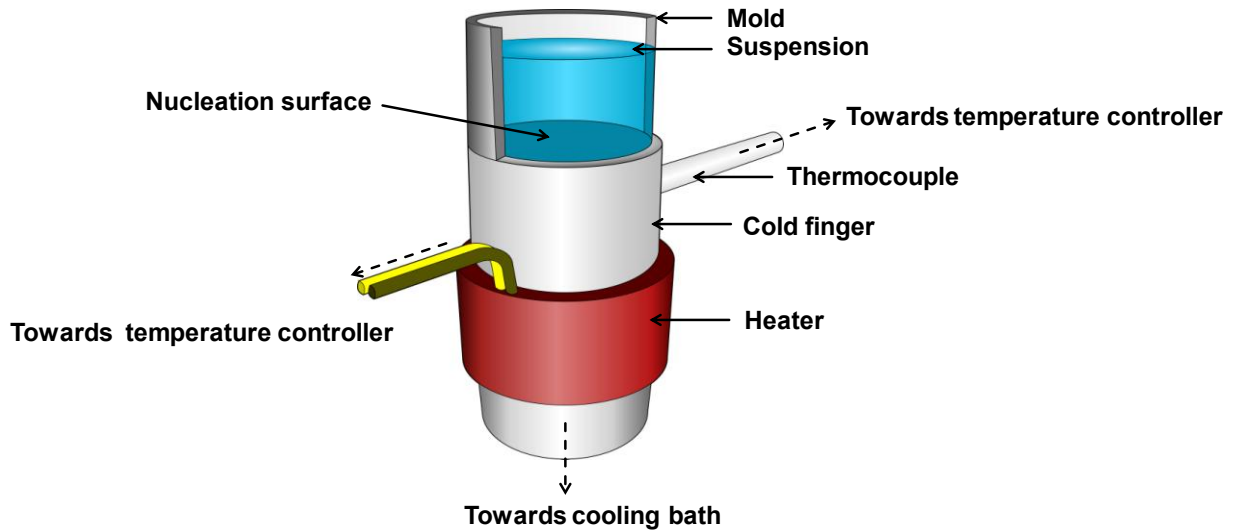


Figure 2.13: Setup for unidirectional freezing, modified from [71].

Samples prepared by unidirectional freezing have anisotropic structures and therefore anisotropic properties. Munch et al. showed that the compressive strength of alumina prepared

by freeze casting (with 10% sucrose in citric acid solution, pH=2.5) can be ten times higher in parallel direction (around 12.5 MPa) than in perpendicular direction (around 1 MPa) [71].

After solidification, the frozen solvent is removed by sublimation to get a green body, which is subjected to subsequent sintering or pyrolysis for densification. During the sintering or pyrolysis, micropores (if exist) can be removed. In case of high solid loading samples, the macroporous structure can even be removed and a dense structure is obtained [76]. More details of freeze casting can be found in Chapter 5 and 6.

Emulsion templating can also be used for manufacturing of macroporous ceramics. Emulsions are made of a continuous phase and a dispersed phase, which can be stabilized mostly by surfactant or colloidal particles adsorbed at liquid interfaces. Depending on the ratio of water or oil, emulsion can be divided into oil-in-water emulsion or water-in-oil emulsion. The emulsion can be prepared by pressing the pressurized oil to be dispersed, through controlled pores of membranes, forming countless oil droplets on the inner surface of the membrane [77]. To prepare ceramic materials by emulsion templating, a ceramic precursor is added to emulsion. Then sol gel (inorganic materials) or polymerization (organic precursor) is often needed to form a rigid shell around liquid droplets to avoid structure collapse during the liquid removal. After subsequent washing or heat treatment, macroporous ceramics can be obtained. The porosity and morphology can be adjusted by changing the ratio between oil phase and water phase. When the volume of the droplets exceeds 50%, droplets self-assemble happens, which leads to ordered porous structure [78]. Emulsion method can produce the pore size from 50 nm to 250  $\mu\text{m}$  [79], which can be adjusted by choosing membrane pore size to get desired droplets size.

Phase separation accompanied sol-gel process can be used to prepare a bicontinuous porous structure, in which both, gel-rich and solvent-rich, phases are interconnected on micrometer scale. Macroporous  $\text{Al}_2\text{O}_3$  has been prepared using  $\text{AlCl}_3$  as the precursors in a water/ ethanol mixture, in which PEO induces phase separation and propylene oxide controls the gelation [68].

In direct foaming method, a porous structure is created by introducing gas into ceramic suspension or a liquid precursor, followed by setting of the porous structure. Gas can be introduced either by chemical methods or physical methods. Physical methods include air entrapment by stirring [80], or evaporation of volatile solvents etc. [80–81]. Chemical methods include generating  $\text{CO}_2$  by chemical reaction [81], or gases by decomposition of blowing agents [63]. Due to the high gas-liquid interfacial area, liquid foams are thermodynamically unstable. Therefore, to get narrow pore size distribution the liquid foams need to get stabilized during setting process, avoiding drainage, coalescent and Ostwald ripening of bubbles. Surfactants stabilize foams by adsorbing on the gas-liquid interfaces, which lowers substantially surface energy of interfaces. Apart from surfactants, amphiphilic particles can also stabilize bubbles [59]. Pore sizes of particle stabilized foams (10 to 300  $\mu\text{m}$ ) can be relatively smaller than that of surfactant stabilized foams (20 to 1000  $\mu\text{m}$ ) [59]. The setting process can be achieved by sol-gel process or polymerization.

Additive manufacturing also named as rapid prototyping or 3D printing, refers to applying computer-aided design model to produce three-dimensional structure by sequential assembly of individual layers of the object (layer deposition process), which can be seen from Figure 2.14. Additive manufacturing can be used to prepare porous ceramics as well as dense ceramics. This technology has been less employed in ceramics than plastic or metal industry due to the high melting points of ceramics. In spite of this, it is a very promising technique. For example scaffolds for biological applications have been manufactured by additive manufacturing. Additive manufacturing of ceramics can start from ceramic powders or polymer precursors, in form of powders, paste and suspension. In case of paste or suspension as ink materials, it should show shear thin behavior of rheology, which means that the ink materials should flow through the deposition nozzle at high shear stresses and then be able to suddenly set at low stress to achieve shape retention [82]. When ceramic powders are used as ink materials, they are jointed either by sintering using laser generating high temperature (e.g. selective laser sintering technique), using feedstock containing ceramic powders and binders (direct inkjet printing) or applying binder layer on top of ceramic layer and subsequent sintering process. Ceramic powders as ink materials often result in residual porosity after sintering, therefore having negative effect on the mechanical properties. Porous ceramics prepared by indirect printing have pores generally bigger than 500  $\mu\text{m}$  mostly due to difficulty in removing excess powders [83]. Porous ceramics prepared by selective laser sintering can produce pore sizes down to 300  $\mu\text{m}$ . For polymer ceramic precursors, stereolithography are applied, in which photosensitive resin is exposed to light for curing and is pyrolyzed to get ceramic parts [84]. Stereolithography can generate cell sizes as small as 1  $\mu\text{m}$  [85]. Introducing ceramic powders into polymer precursors makes additive manufacturing of ceramic parts more versatile.

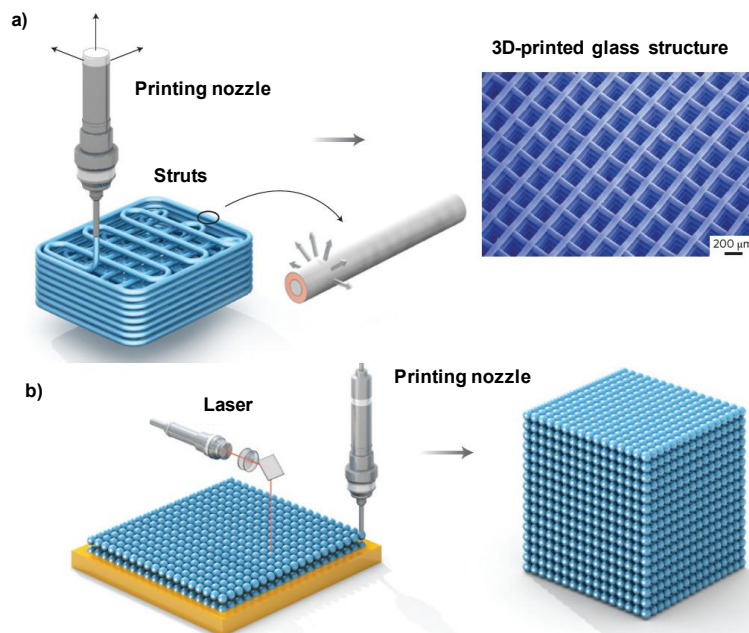


Figure 2.14: Scheme of additive manufacturing (Robocasting) [88].

## 2. State of the art

The mechanical properties of macroporous ceramics are of particular interest in this work. Studart et al summarized the compressive strength of macroporous ceramics ( $\text{Al}_2\text{O}_3$ ,  $\text{Si(O)C}$ , HAP) prepared by the direct foaming, replica method and sacrificial templating method with different relative density (porosity) [86].

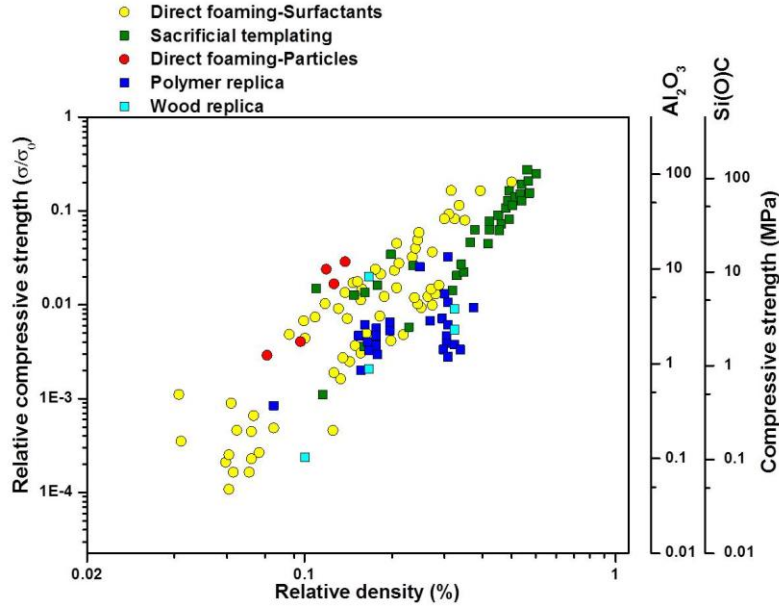


Figure 2.15: Compressive strength of macroporous ceramics prepared by different techniques, modified from [86]. The relative strength is the compressive strength ratio between porous and dense materials, assuming the compressive strength of dense alumina and silicon carbide to be 400 and 450 MPa [86].

The compressive strength of macroporous ceramics prepared by additive manufacturing has also been studied. Eckel et al showed the compressive strength of  $\text{SiOC}$  microlattice (periodic macroporous structure) prepared by additive manufacturing is much higher than foams prepared by other methods [87].

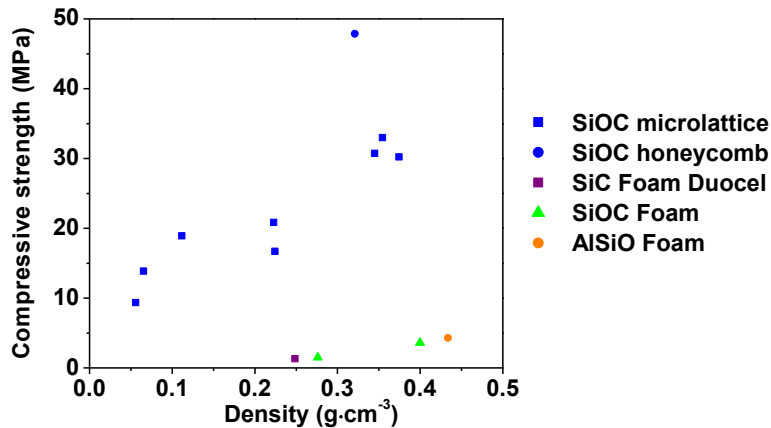


Figure 2.16: Compressive strength of  $\text{SiOC}$  microlattice comparing with other foams [87].



### 2.4.2 Macroporous ceramics in different applications

Macroporous ceramics have been widely used in industry and biomedical applications, such as catalysis supports in the heterogeneous reactions, where gases or liquids pass through the catalyst support with catalyst well distributed on it. Different shapes (foam, or honeycomb or pellets) of catalyst support materials (glass, silica, quartz etc.) have been used [88]. Hierarchical pores are often engineered into the macroporous structure to improve the specific surface area for the active sites [89]. These hierarchically ordered porous ceramics can also be used as electrode materials in electro-chemical devices [90].

Due to the sieving effects of pores, macroporous ceramics can be applied in filtration. Filtration can be classified into different categories based on pore diameters, for macroporous materials, mainly related to macro-filtration ( $100\text{ nm} < d < 10\text{ }\mu\text{m}$ ) and filtration ( $d > 10\text{ }\mu\text{m}$ ) [88]. Ceramic filters are widely used in diesel engines as diesel particulate filters [91]. Besides, porous ceramics can be modified with functional groups or silver particles as water purification filters for water treatment [92]. Another application of ceramic filter is to exclude impurities in molten metal filtration [93].

Bioapplications, such as dental or orthopedic implants require the ceramic materials to be chemically inert and biocompatible, and to have adequate mechanical strength and adequate fatigue life, proper weight and density. For example, macroporous ceramics used as scaffolds for bone tissue engineering require compressive strength of 0.2–2.5 MPa [94]. The macropores allow the blood and nutrients to transfer through the porous structure and ingrowth of cells. Besides, the porous ceramics should show degradability, which means they can be replaced by bone after long-term. Bioglass® [95], hydroxyapatite [96–97] are normally used to fabricate bone scaffold, most of them have pores size around 100 to 1000  $\mu\text{m}$ .

## 2.5 Polymer derived ceramics

### 2.5.1 Cross-linking and pyrolytic conversion of preceramic polymers

Non-oxide ceramics such as silicon carbide (SiC) and silicon nitride ( $\text{Si}_3\text{N}_4$ ) are used as thermo-mechanical materials due to their stiffness and structural stability under harsh environments. These materials exhibit a very high resistance to oxidation below 1400 °C, especially boron-containing SiCN ceramics can be stable even at 2200 °C due to the high temperature stability in terms of decomposition. Preceramic polymers can be used to produce polymer derived ceramics, such as SiC,  $\text{Si}_3\text{N}_4$ , etc. Preceramic polymers which contain silicon in the backbone can be divided into different types based on the elements in the backbone as shown in Figure 2.17. Preceramic polymers are prepared from monomers, and chlorosilanes  $\text{R}_x\text{SiCl}_{4-x}$  ( $x=1-3$ ; R= organic side group) are the most frequently used starting compounds due to their commercial availability and low cost. Chlorosilanes can be transferred into different polymers depending on solvents (water or toluene or  $\text{NH}_3$ , etc.) [98].

Pre-ceramic polymers begin usually cross-linking under heating or light radiation conditions. Polysilazanes can cross-link at room temperature in air and polysiloxanes also cross-link at room temperature in the presence of water. The cross-linked products convert to ceramics during pyrolysis. SiC, Si<sub>3</sub>N<sub>4</sub>, SiCN, or SiBOC etc. can be obtained depending on the types of precursors. However, even from the same pre-ceramic polymer, different products can be produced at different pyrolysis temperatures. Figure 2.18 shows the corresponding products of polysiloxanes at different pyrolysis temperature. Polysiloxanes cross-link from 200 to 400 °C, start decomposition above 400 °C, and form hybrid ceramics up to 800 °C. Further increase of temperature leads to SiOC or SiC ceramics depending on the temperature range.

Comparing to the traditional way of using ceramic powders to prepare ceramic components, polymer derived ceramics have the following advantages [99]:

1. Preparing ceramic components which are difficult to obtain by conventional powder processing. For example, SiOC materials cannot be prepared by dissolving oxygen or carbon in SiC or SiO<sub>2</sub> ceramic powders. It can, however, easily be prepared by pyrolyzing polysiloxanes.
2. Preparing ceramic shapes (fibers and layers, or composite materials) which are difficult to obtain by conventional powder processing. Conventional plastic forming technologies (polymer infiltration pyrolysis, injection molding, coating from solvent, or resin transfer molding) can be used to fabricate monoliths. Besides, near-net-shape ceramics can be prepared by mixing active fillers into polymer precursors and controlling pyrolysis conditions.
3. Lower processing temperatures compared to conventional powder processing. To sinter covalent SiC or Si<sub>3</sub>N<sub>4</sub> by conventional ceramic powder processes, the temperature should be as high as 1700–2000 °C. However, with pre-ceramic precursors, only moderate temperatures like 1100–1300 °C are needed [98].
4. Tailoring of pore size, thermal stability and surface characteristics. Compared to ceramic powder processing, pre-ceramic precursors often result in micropores or mesopores, which are very beneficial for applications requiring high specific surface areas. The organic groups can be fully or partially decomposed to alter the surface characteristics.

## Preceramic Organosilicon Polymers

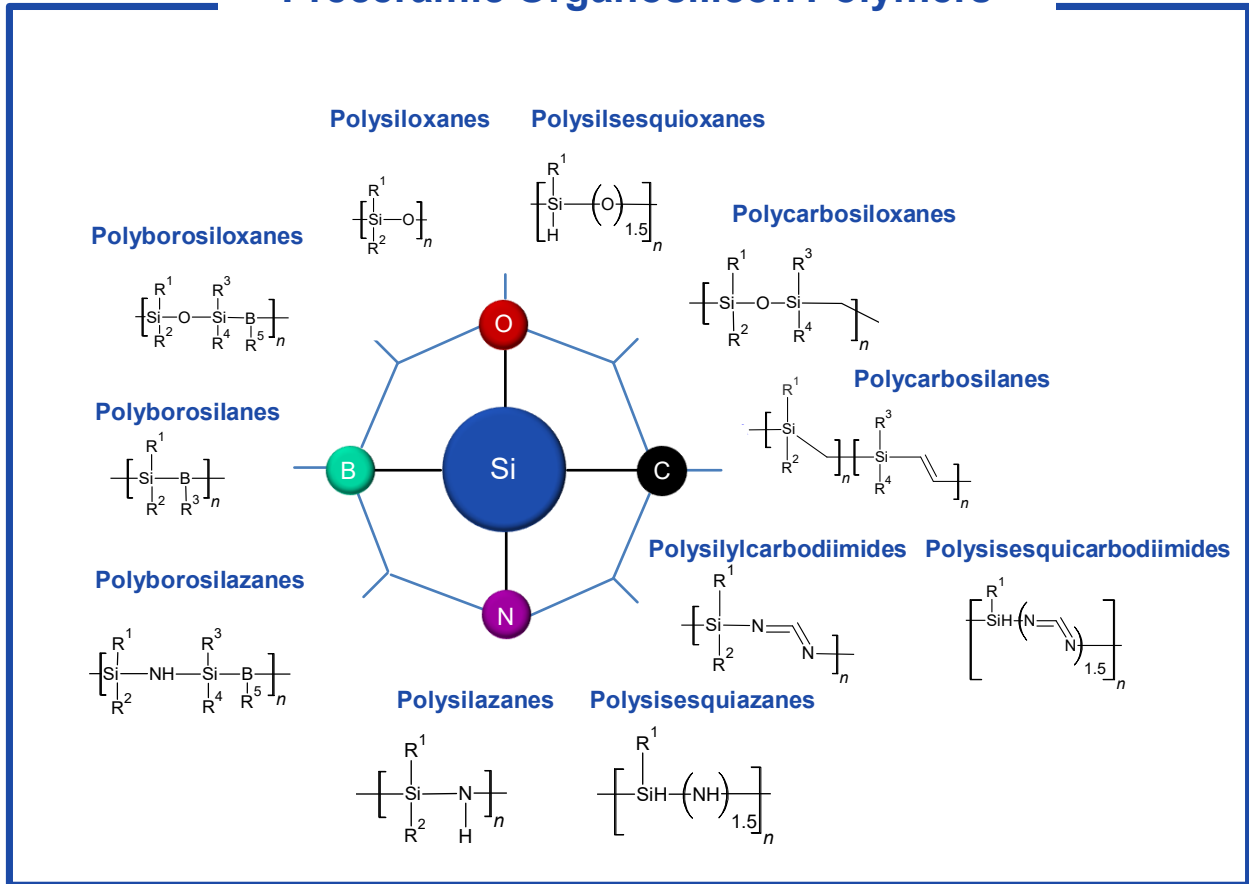


Figure 2.17: Types of preceramic organosilicon polymers [98].

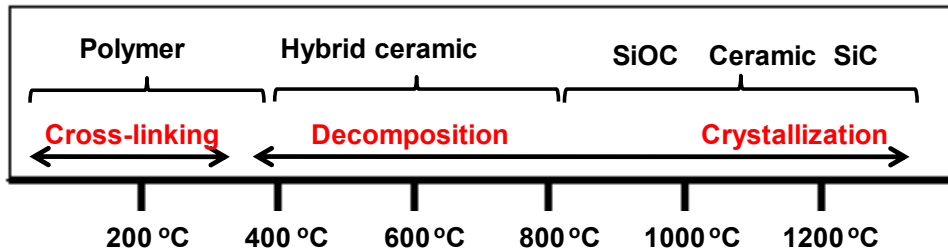


Figure 2.18: Pyrolytic conversion products of polysiloxanes at different temperature.

### 2.5.2 Adjustment of porosity and surface characteristics

Pyrolyzing preceramic polymers can produce either nonporous or porous ceramics, depending on the processing parameters. Comparing with ceramic powder precursors, micropores (pore size < 2nm) or mesopores (2nm < pore size < 50 nm) can be additionally created by polymer derived ceramics. Therefore, using preceramic polymer enables easy fabrication of hierarchically porous structure. Taking polysiloxane as an example, from 200 °C to 400 °C, water

molecular and oligomers are released from the cross-linked body. At temperature higher than 400 °C, organic function groups are released. In case of methyl phenyl polysiloxane, C<sub>6</sub>H<sub>5</sub>- is decomposed at around 500–700 °C [100]. Due to the gas evolution, micropores can be created during the pyrolysis.

Molecular structure of precursors, pyrolysis temperatures, heating rates and gas atmosphere all can influence the gas evolution; therefore the porous structures can be tuned by the choice of these parameters. Most of the pores produced directly by preceramic polymers are micropores, which lead to high specific surface area. Sorarù et al investigated both pyrolysis products of linear and hyperbranched alkoxy-substituted polysiloxanes of the type '[Si(OR)<sub>2</sub>CH<sub>2</sub>]', which showed that the hyperbranched precursors led to micro/mesopores after pyrolysis, while linear precursor only led to micropores [101]. Prasad et al. showed that pyrolysis of poly(diphenylsilylcarbodiimide) at 1000–1500 °C for 2 h resulted in nonporous materials, further increase of temperature to 1600 °C led to micropores formation and there were no micropores observed at temperature higher than 2000 °C [102]. Schmidt et al. showed that fast pyrolysis of cross-linked polysiloxanes led to crack formation and micropores collapse even at 600 °C, while slow pyrolysis can preserve mesopores up to 1200 °C [103].

Surface characteristics of polymer derived ceramics mainly refer to hydrophilicity/hydrophobicity. Surface attracting water is hydrophilic, while surface repelling water is hydrophobic. Engineering surface characteristics is important in many technical processes. For example, separating oil from water in case of oil spills remediation needs a separation medium with more hydrophobic surfaces to absorb hydrophobic petroleum hydrocarbons [104]. Different surface characteristics can also be interpreted as different surface energies or surface tensions. In wicking applications, the wetting of the surface by liquids is greatly influenced by surface characteristics of the solid. Ferrero et al. reported that polyester fabric surfaces with different plasma treatments showed significantly different capillary rise heights [105].

The commonly used preceramic polymers are hydrophobic, and the surface characteristics of polymer derived products can be altered by varying pyrolysis temperatures, as seen from Figure 2.18. Prenzel et al. reported that pyrolyzing methyl polysiloxane (MK) at temperatures below 630 °C resulted in hydrophobic surface, while pyrolyzing at 700 °C made the hydrophobic organic moieties on the surface decompose further, leading to more hydrophilic surface [106].

The surface characteristics of the polymer derived ceramics can also be modified by the choice of the precursors, or surface modification, which influences the surface characteristics of final ceramics. There are a few techniques for surface modification. Plasma is often used to modify the surface characteristics of the preceramic polymers; however, the surface characteristics of derived ceramics are not much affected. The surface characteristics of the precursors can be modified to a greater extent by compositing it with more hydrophilic materials. The surface characteristics can be adjusted by varying the ratio between the preceramic polymers to hydrophilic materials. More details can be seen from chapter 5.

### 2.5.3 Polymer derived ceramics as structural materials and for other applications

The main limitations of applying polymer derived ceramics are due to the high volume shrinkage (may exceed 50%) and the pronounced density increase (a factor of 2 or 3) during the polymer-ceramic conversion. Fillers can be used to compensate the shrinkage caused by polymer decomposition and using active fillers can even get near-net shaped components, which can be used as structural materials. The applications of polymer derived ceramics include the following fields:

#### (1) Coating

Pre-ceramic polymers can form covalent bonds between precursors and coated surface; therefore, they are very attractive for coating on metals, polymers and ceramics against corrosion, oxidation at high temperature or wear, in applications such as environmental barrier coating, thermal barrier coating, and protective coating against metal corrosion [107]. Due to the isotropic shrinkage behavior, the thicknesses are controlled between 100–200 nm to avoid crack formation. By adding fillers the thickness of coating can be increased.

#### (2) Fibers

Polymer derived ceramics can be used to prepare fibers (SiC, SiCN or SiBCN fibers) used in ceramic matrix composites. Light weight SiC fiber reinforced SiC matrix composites can be used as thermal protection devices in extreme environments for aerospace applications, like combustion and turbine section components of aero-propulsion and land-based gas turbine engines. It has superior properties comparing with metallic super alloys, monolithic ceramics, carbon fiber composites or oxide/oxide ceramic composites.

#### (3) Matrix

Pre-ceramic polymers can also be used as matrix for fiber reinforced ceramic matrix composites (CMCs), in which polymers are introduced into CMCs as melt liquids by impregnation [108]. Polysiloxanes derived matrixes are restricted to applications below 1200 °C due to the oxygen content in the matrix, while polysilazanes and polyborosilazanes derived ceramics can survive higher temperatures [109].

#### (4) High performance components

Filled polysiloxanes can be used to prepare high precision shaping of complex components for vacuum pump devices for harsh environments. Fillers, such as Al<sub>2</sub>O<sub>3</sub> or SiO<sub>2</sub> are used to adjust their coefficients of thermal expansion to be compatible with steel or aluminum alloys [110].

Ceramic-matrix composites derived from polycarbosilane precursors with SiC as filler, carbon fiber as reinforcement are used as brake disc in high performance automobile due to the lower density and better friction coefficient compared to metal brakes [98].

Silicon carbide based composites have been studied for in-vessel components of nuclear fusion reactors due to its following properties: Higher operating temperatures than metallic alloys, low level of long-lived radioisotopes and tolerance against neutron irradiation up to high temperatures [111].

### (5) Other applications

Due to adjustable porosity and surface characteristics, polymer derived ceramics can also be used to prepare membranes for breaking or creating micro-emulsions and ceramic micro electro mechanical systems (MEMS). The porous polymer derived ceramics have also been investigated as electrode materials for electrochemical applications.

### References

- [1] J. B. Schutz, Properties of composite materials for cryogenic applications, *Cryogenics* 38 (1988) 3–12.
- [2] Space shuttle main engine enhancements, NASA, Fact sheet number: FS-2000-07-159-MSFC.
- [3] Y. X. He, Q. Li, T. Kuila, N. H. Kim, T. W. Jiang et al., Micro-crack behavior of carbon fiber reinforced thermoplastic modified epoxy composites for cryogenic applications, *Composites: Part B* 44 (2013) 533–539.
- [4] K. Enya, N. Yamada, T. Imai, Y. Tange, H. Kaneda et al., High-precision CTE measurement of hybrid C/SiC composite for cryogenic space telescopes, *Cryogenics* 52 (2012) 86–89.
- [5] H. Kaneda, T. Onaka, T. Nakagawa, K. Enya, H. Murakami et al., Cryogenic optical performance of the ASTRO-F SiC telescope, *Appl. Optics* 44 (2005) 6823–6832.
- [6] H. Q. Li, C. Fan, K. X. Tao, H. Choo, P. K. Liaw, Compressive behavior of a Zr-based metallic glass at cryogenic temperatures, *Adv. Mater.* 18 (2006) 752–754.
- [7] C. E. Taylor, *Cryogenic engineering and fusion power*, Advances in cryogenic engineering, ISBN: 978-1-4613-9849-3, Springer, 1995, Boston.
- [8] A. Yamanaka, T. Kashima, K. Hosoyama, Coil bobbin composed of high-strength polyethylene fiber reinforced plastics for a stable high-field superconducting magnet. *IEEE Trans. Appl. Supercond.* 11 (2001) 4061–4064.
- [9] K. Yoshida, H. Nakajima, K. Koizumi, M. Shimada, Y. Sanada et al., *Development of cryogenic structural materials for tokamak reactor, Austenitic Steels at Low Temperature*, ISBN: 978-1-4613-3732-4, Springer, 1983, Boston.
- [10] S. Kalia, S. Y. Fu, *Polymers at cryogenic temperatures*, ISBN: 978-3-642-35334-5, Springer, 2013, Berlin.
- [11] N. Fries, *Capillary transport processes in porous materials – experiment and model*, ISBN 978-3-86955-507-2, Cuvillier Verlag, 2010, Göttingen.
- [12] M. Zhang, *Capillary transport of cryogenic liquids in porous structure*, ISBN 978-3-95404-443-6, Cuvillier Verlag, 2013, Göttingen.

- [13] F. T. Dodge, The new dynamic behavior of liquids in moving containers, Southwest Research Institute, 2000, Texas.
- [14] E. P. Symons, Wicking of liquids in screens, Technical Report NASA TN-D-7657, NASA Lewis Research Center, 1974, Cleveland.
- [15] Y. Grebenyuk, M. E. Dreyer, Wicking of liquid nitrogen into superheated porous structures, *Cryogenics* 78 (2016) 27–39.
- [16] N. Fries, K. Odic, M. Dreyer, Wicking of perfectly wetting liquids into a metallic mesh, Proceedings of the 2nd International Conference on Porous Media and its Applications in Science and Engineering, 2007, Hawaii.
- [17] D. K. Khrustalev, S. Y. Semenov, Advances in low-temperature, cryogenic and miniature loop heat pipes, V Minsk International Seminar 'Heat Pipes, Heat Pumps, Refrigerators', 2003, Minsk.
- [18] T. Zhang, P. deBock, E. W. Stautner, T. Deng, C. Immer, Demonstration of liquid nitrogen wicking using a multi-layer metallic wire cloth laminate, *Cryogenics* 52 (2012) 301–305.
- [19] L. Bai, L. P. Zhang, G. P. Lin, J. He, D. S. Wen, Development of cryogenic loop heat pipes: A review and comparative analysis, *Appl. Therm. Eng.* 89 (2015) 180–191.
- [20] B. Seidenberg, T. D. Swanson, Ceramic heat pipe wick, US 4883116 A, 1989.
- [21] P. Meisel, M. Jobst, W. Lippmann, A. Hurtado, Design and manufacture of ceramic heat pipes for high temperature applications, *Appl. Therm. Eng.* 75 (2015) 692–699.
- [22] X. Q. Cao, R. Vassen, D. Stoeber, Ceramic materials for thermal barrier coatings, *J. Eur. Ceram. Soc.* 24 (2014) 1–10.
- [23] A. Koller, Structure and properties of ceramics, ISBN 0-444-98719-3, Elsevier, 1994, Amsterdam.
- [24] K. Watari, K. Ishizaki, F. Tsuchiya, Phonon scattering and thermal conduction mechanisms of sintered aluminium nitride ceramics, *J. Mater. Sci.* 28 (1993) 3709–3714.
- [25] R. C. Zeller, R. O. Phol, Thermal conductivity and specific heat of noncrystalline solids, *Phys. Rev. B* 4 (1971) 2029–2041.
- [26] D. Y. Li, Y. Y. Wu, P. Kim, L. Shi, P. D. Yang et al., Thermal conductivity of individual silicon nanowires, *Appl. Phys. Lett.* 83 (2003) 2934–2936.
- [27] J. A. Katerberg, A. C. Anderson, Low-temperature specific heat, thermal conductivity, and ultrasonic velocity of glassy carbon, *J. Low Temp. Phys.* 30 (1978) 739–745.
- [28] N. P. Padture, M. Gell, E. H. Jordan, Thermal barrier coatings for gas-turbine engine applications, *Science* 296 (2012) 280–286.
- [29] J. S. O. Evans, P. A. Hanson, R. M. Ibberson, N. Duan, U. Kameswari et al., Low-temperature oxygen migration and negative thermal expansion in  $ZrW_{2-x}Mo_xO_8$ , *J. Am. Chem. Soc.* 122 (2000) 8694–8699.
- [30] D. K. Agrawal, R. Roy, Composite route to "zero" expansion ceramics, *J. Mater. Sci.* 20 (1985) 4617–4623.
- [31] F. J. Parker,  $Al_2TiO_5$ - $ZrTiO_4$ - $ZrO_2$  composites: A new family of low thermal expansion ceramics, *J. Am. Ceram. Soc.* 73 (1990) 929–932.

- [32] F. A. Hummel, Observations on the thermal expansion of crystalline and glassy substances, *Am. Ceram. Soc.* 33 (1950)102–107.
- [33] J. Bischoe, C. S. Robinson, Jr., B. E. Warren, X-Ray study of boric oxide-silica glass, *J. Am. Ceram. Soc.* 22 (1939) 180–184.
- [34] H. Schneider, E. Eberhard, Thermal expansion of mullite, *J. Am. Ceram. Soc.*73 (1990) 2073–2076.
- [35] R. L. Coble, W. D. Kingery, Effect of porosity on the physical properties of sintered alumina, *J. Am. Ceram. Soc.* 39 (1956) 377–385.
- [36] E. P. Roth, A. C. Anderson, Low-temperature thermal conductivity and specific heat of a machinable ceramic, *J. Appl. Phys.* 47 (1976) 3644–3647.
- [37] D. E. Sharp, L. B. Ginther, Effect of composition and temperature on the specific heat of glass, *J. Am. Ceram. Soc.* 34 (1951) 260–271.
- [38] A. Mochot, D. S. Smith, S. Degot, C. Gault, Thermal conductivity and specific heat of kaolinite: Evolution with thermal treatment, *J. Eur. Ceram. Soc.* 28 (2008) 2639–2644.
- [39] R. B. Stephens, Low-temperature specific heat and thermal conductivity of noncrystalline dielectric solid, *Phys. Rev. B* 8 (1973) 2896–2905.
- [40] B. L. Zink, R. Pietri, F. Hellman, Thermal conductivity and specific heat of thin-film amorphous silicon, *Phys. Rev. Lett.* 96 (2006) 055902 (1–4).
- [41] L. Hitova, R. Yakimova, E. P. Trifonova, A. Lenchev, E. Janzen, Heat capacity of 4H-SiC determined by differential scanning calorimetry, *J. Electrochem. Soc.* 147 (2000) 3546–3547.
- [42] L. J. Gibson, M. F. Ashby, *Cellular solids structure and properties*, ISBN 0-521-49560-1, Cambridge University Press, 1997, Cambridge.
- [43] K. E. Pappacena, K. T. Faber, H. Wang, W. D. Porter, Thermal conductivity of porous silicon carbide derived from wood precursors, *J. Am. Ceram. Soc.* 90 (2007) 2855–2862.
- [44] J. Francl, W. D. Kingery, Experimental investigation of effect of porosity on thermal conductivity, *J. Am. Ceram. Soc.* 37 (1954) 99–107.
- [45] G. C. J. Bart, *Thermal conduction in non homogeneous and phase change media*, ISBN 90-9007794-4, Delft University of Technology, 1994, Netherlands.
- [46] J. K. Carson, S. J. Lovatt, D. J. Tanner, A. C. Cleland, Thermal conductivity bounds for isotropic, porous materials, *Int. J. Heat Mass Transfer.* 48 (2005) 2150–2158.
- [47] R. Landauer, The electrical resistance of binary metallic mixtures, *J. Appl. Phys.* 23 (1952) 779–784.
- [48] L. L. Gong, Y. H. Wang, X. D. Cheng, R. F. Zhang, H. P. Zhang, Thermal conductivity of highly porous mullite materials, *Int. J. Heat Mass Transfer.* 67 (2013) 253–259.
- [49] D. S. Smith, A. Alzina, J. Bourret, B. Nait-Ali, F. Pennec et al., Thermal conductivity of porous materials, *J. Mater. Res.* 28 (2013) 2260–2272.
- [50] D. M. Liu, Influence of porosity and pore size on the compressive strength of porous hydroxyapatite ceramic, *Ceram. Int.* 23 (1997) 135–139.
- [51] P. Colombo, J. R. Hellmann, D. L. Shelleman, Mechanical properties of silicon oxycarbide ceramic foams, *J. Am. Ceram. Soc.* 84 (2001) 2245–2251.



- [52] R. Kumar, B. Bhattacharjee, Porosity, pore size distribution and in situ strength of concrete, *Cem. Concr. Res.* 33 (2003) 155–164.
- [53] X. D. Chen, S. X. Wu, J.K. Zhou, Influence of porosity on compressive and tensile strength of cement mortar, *Constr. Build. Mater.* 40 (2013) 869–874.
- [54] R. W. Rice, Comparison of stress concentration versus minimum solid area based mechanical property-porosity relations, *J. Mater. Sci.*, 28 (1993) 2187–2190.
- [55] K. A. Hing, S. M. Best, W. Bonfield, Characterization of porous hydroxyapatite, *J. Mater. Sci.: Mater. Med.* 10 (1999) 135–145.
- [56] M. W. Barsoum, T. El-Raghy, Synthesis and characterization of a remarkable ceramic:  $Ti_3SiC_2$ , *J. Am. Ceram. Soc.* 79 (1996) 1953–1956.
- [57] L. F. Li, Z. Zhang, L. Z. Zhao, Z. H. Tu, Y. Y. Li, Strength and toughness of  $ZrO_2$ -based ceramics at cryogenic temperature, *Cryogenics*, 34 (1994) 469–472.
- [58] W. J. Xuan, J. Yi, Z. P. Xie, W. Liu, J. Chen, Enhanced fracture toughness of silicon nitride ceramics at cryogenic temperatures, *Scr. Mater.* 66 (2012) 891–894.
- [59] A. R. Studart, U. T. Gonzenbach, E. Tervoort, L. J. Gauckler, Processing routes to macroporous ceramics: a review, *J. Am. Ceram. Soc.* 89 (2006) 1771–1789.
- [60] K. Schwarzwaldner, A. V. Somers, Methods of making porous ceramic articles, US3090094, 1963.
- [61] P. Colombo, J. R. Hellmann, Ceramic foams from preceramic polymers, *Mat. Res. Innovat.* 6 (2002) 260–272.
- [62] R. A. White, J. N. Weber, E. W. White, Replamineform: a new process for preparing porous ceramic, metal, and polymer prosthetic materials, *Science* 176 (1972) 922–924.
- [63] C. Vakifahmetoglu, I. Menapace, A. Hirsch, L. Biasetto, R. Hauser et al., Highly porous macro- and micro-cellular ceramics from a polysilazane precursor, *Ceram. Int.* 35 (2009) 3281–3290.
- [64] I. K. Sung, Christian, M. Mitchell, D. P. Kim, P. J. A. Kenis, Tailored macroporous SiCN and SiC structures for high-temperature fuel reforming, *Adv. Funct. Mater.* 15 (2005) 1336–1342.
- [65] T. J. Fitzgerald, V. J. Michaud, A. Mortensen, Processing of microcellular SiC foams, *J. Mater. Sci.* 30 (1995) 1037–1045.
- [66] S. Deville, Freeze-casting of porous ceramics: a review of current achievements and issues, *Adv. Eng. Mater.* 10 (2008) 155–169.
- [67] A. Imhof, D. J. Pine, Uniform macroporous ceramics and plastics by emulsion templating, *Adv. Mater.* 10 (1998) 697–700.
- [68] Y. Tokudome, K. Fujita, K. Nakanishi, K. Miura, K. Hirao, Synthesis of monolithic  $Al_2O_3$  with well-defined macropores and mesostructured skeletons via the sol-gel process accompanied by phase separation, *Chem. Mater.* 19 (2007) 3393–3398.
- [69] M. Naviroj, S. M. Miller, P. Colombo, K.T. Faber, Directionally aligned macroporous SiOC via freeze casting of preceramic polymers, *J. Eur. Ceram. Soc.* 35 (2015) 2225–2232.
- [70] R. F. Chen, C. A. Wang, Y. Huang, L. G. Ma, W. Y. Lin, Ceramics with special porous structures fabricated by freeze-gelcasting: using tert-butyl alcohol as a template, *J. Am. Ceram. Soc.* 90 (2007) 3478–3484.

- [71] E. Munch, E. Saiz, A. P. Tomsia, S. Deville, Architectural control of freeze-cast ceramics through additives and templating, *J. Am. Ceram. Soc.* 92 (2009) 1534–1539.
- [72] Y. F. Tang, S. Qiu, C. Wu, Q. Miao, K. Zhao, Freeze cast fabrication of porous ceramics using tert-butyl alcohol-water crystals as template, *J. Eur. Ceram. Soc.* 36 (2016) 1513–1518.
- [73] C. Pekor, B. Groth, I. Nettleship, The effect of polyvinyl alcohol on the microstructure and permeability of freeze-cast alumina, *J. Am. Ceram. Soc.* 93 (2010) 115–120.
- [74] S. Deville, E. Saiz, A. P. Tomsia, Ice-templated porous alumina structures, *Acta Mater.* 55 (2007) 1965–1974.
- [75] K. Araki, J. W. Halloran, Porous ceramic bodies with interconnected pore channels by a novel freeze casting technique, *J. Am. Ceram. Soc.* 88 (2005) 1108–1114.
- [76] S. W. Sofie, F. Dogan, Freeze casting of aqueous alumina slurries with glycerol, *J. Am. Ceram. Soc.* 84 (2001) 1459–1464.
- [77] T. Nakashima, M. Shimizu, M. Kukizaki, Particle control of emulsion by membrane emulsification and its application, *Adv. Drug Deliv. Rev.* 45 (2000) 47–56.
- [78] A. Imhof, D. J. Pine, Ordered macroporous materials by emulsion templating, *Nature* 389 (1997) 948–951.
- [79] I. Akartuna, A. R. Studart, E. Tervoort, L. J. Gauckler, Macroporous ceramics from particle-stabilized emulsions, *Adv. Mater.* 20 (2008) 4714–4718.
- [80] S. Barg, C. Soltmann, M. Andrade, D. Koch, G. Grathwohl, Cellular ceramics by direct foaming of emulsified ceramic powder suspension, *J. Am. Ceram. Soc.* 91 (2008) 2823–2829.
- [81] P. Colombo, M. Modesti, Silicon oxycarbide foams from a silicone preceramic polymer and polyurethane, *J. Sol-Gel Sci. Technol.* 14 (1999) 103–111.
- [82] G. Pierin, C. Grotta, P. Colombo, C. Mattevi, Direct ink writing of micrometric SiOC ceramic structures using a preceramic polymer, *J. Eur. Ceram. Soc.* 36 (2016) 1589–1594.
- [83] A. Zocca, P. Colombo, C. M. Gomes, J. Günster, Additive manufacturing of ceramics: issues, potentialities, and opportunities, *J. Am. Ceram. Soc.* 98 (2015) 1983–2001.
- [84] M. Schwentenwein, J. Homa, Additive manufacturing of dense alumina ceramics, *Int. J. Appl. Ceram. Technol.* 12 (2015) 1–7.
- [85] U. G. K. Wegst, H. Bai, E. Saiz, A. P. Tomsia, R. O. Ritchie, Bioinspired structural materials, *Nature* 14 (2014) 23–36.
- [86] U. T. Gonzenbach, A. R. Studart, E. Tervoort, L. J. Gauckler, Macroporous ceramics from particle-stabilized wet foams, *J. Am. Ceram. Soc.* 90 (2007) 16–22.
- [87] Z. C. Eckel, C. Y. Zhou, J. H. Martin, A. J. Jacobsen, W. B. Carter, T. A. Schaedler, Additive manufacturing of polymer-derived ceramics, *Science* 351 (2016) 58–62.
- [88] T. Ohji, M. Fukushima, Macro-porous ceramics: processing and properties, *Int. Mater. Rev.* 57 (2012) 115–131.
- [89] C. M. A. Parlett, K. Wilson, A. F. Lee, Hierarchical porous materials: catalytic applications, *Chem. Soc. Rev.* 43 (2013) 3876–3893.
- [90] Y. Li, Z. Y. Fu, B. L. Su, Hierarchically structured porous materials for energy conversion and storage, *Adv. Funct. Mater.* 22 (2012) 4634–4667.

- [91] J. Adler, Ceramic diesel particulate filters, *Int. J. Appl. Ceram. Technol.* 2[6] (2005) 429–439.
- [92] Y. H. Lv, H. Liu, Z. Wang, S. J. Liu, L. J. Hao et al., Silver nanoparticle-decorated porous ceramic composite for water treatment, *J. Memb. Sci.* 331 (2009) 50–56.
- [93] M. J. Pryor, T. J. Gray, Ceramic foam filter, US3947363 A, 1976.
- [94] K. Rezwani, Q. Z. Chen, J. J. Blaker, A. R. Boccaccini, Biodegradable and bioactive porous polymer/inorganic composite scaffolds for bone tissue engineering, *Biomaterials* 27 (2006) 3413–3431.
- [95] K. Zhang, Y. Wang, M. A. Hillmeyer, L. F. Francis, Processing and properties of porous poly(L-lactide)/bioactive glass composites, *Biomaterials* 25 (2004) 2489–500.
- [96] R. Y. Zhang, P. X. Ma, Poly(alpha-hydroxyl acids)/hydroxyapatite porous composites for bone-tissue engineering. I. Preparation and morphology. *J. Biomed. Mater. Res.* 44 (1999) 446–455.
- [97] L. Guan, J. E. Davies, Preparation and characterisation of a highly macroporous biodegradable composite tissue engineering scaffold. *J. Biomed. Mater. Res.* 71A (2004) 480–487.
- [98] P. Colombo, G. Mera, R. Riedel, G. D. Sorarù, Polymer-derived ceramics: 40 years of research and innovation in advanced ceramics, *J. Am. Ceram. Soc.* 93 (2010) 1805–1837.
- [99] M. Birot, J. P. Pillot, J. Dunoguès, Comprehensive chemistry of polycarbosilanes, polysilanzanes, and polycarbosilanzanes as precursors of ceramics, *Chem. Rev.* 95 (1995) 1443–1477.
- [100] M. Scheffler, T. Takahashi, J. Kaschta, H. Muensted, P. Buhler et al., “Pyrolytic Decomposition of Pre-ceramic Organo Polysiloxanes”; pp. 239–50 in *Innovative Processing and Synthesis of Ceramics, Glasses, and Composites IV: Ceramic Transactions*, Vol. 115, Edited by N. Bansal and J. P. Singhe, The American Ceramic Society, 2000, Westerville.
- [101] G. D. Sorarù, Q. Liu, L. V. Interrante, T. Apple, Role of precursor molecular structure on the microstructure and high temperature stability of silicon oxycarbide glasses derived from methylene-bridged polycarbosilanes, *Chem. Mater.* 10 (1998) 4047–4054.
- [102] R. M. Prasad, G. Mera, K. Morita, M. Müller, H. J. Kleebe et al., Thermal decomposition of carbon-rich polymer-derived silicon carbonitrides leading to ceramics with high specific surface area and tunable micro- and mesoporosity. *J. Eur. Ceram. Soc.* 32 (2012) 477–484.
- [103] H. Schmidt, D. Koch, G. Grathwohl, P. Colombo, Micro-/macroporous ceramics from pre-ceramic precursors, *J. Am. Ceram. Soc.* 84 (2001) 2252–2255.
- [104] Y. Z. Zhu, D. Wang, L. Jiang, J. Jin, Recent progress in developing advanced membranes for emulsified oil/water separation, *NPG Asia Mater.* 6 (2014) 1–11.
- [105] F. Ferrero, Wettability measurements on plasma treated synthetic fabrics by capillary rise method, *Polym. Test.* 22 (2003) 571–578.
- [106] T. Prenzel, M. Wilhelm, K. Rezwani, Pyrolyzed polysiloxane membranes with tailorable hydrophobicity, porosity and high specific surface area, *Micropor. Mesopor. Mater.* 169 (2013) 160–167.

- [107] G. Barroso, Q. Li, G. Motz, R. K. Bordia, Polymer-derived ceramic and ceramic-like coating: Innovative solution for real problems, *Am. Ceram. Soc. Bull.* 96 (2017) 42–49.
- [108] H. Morozumi, K. Sato, A. Tezuka, H. Kaya, T. Isoda, Preparation of high strength ceramic fiber reinforced silicon nitride composites by a preceramic polymer impregnation method, *Ceram. Int.* 23 (1997) 179–184.
- [109] P. Greil, Polymer derived engineering ceramics, *Adv. Eng. Mater.* 2 (2000) 339–348.
- [110] R. Riedel, G. Mera, R. Hauser, A. Klonczynski, Silicon-based polymer-derived ceramics: synthesis properties and applications- A review, *J. Ceram. Soc. Jpn.* 114 (2006) 425–444.
- [111] Y. Katoh, L. L. Snead, C. H. Henager Jr. A. Hasegawa, A. Kohyama et al., Current status and critical issues for development of SiC composites for fusion applications, *J. Nucl. Mater.* 367-370 Part A (2007) 659–671.

### 3. Aim of the work and approach

Wicking of cryogenic liquid into porous materials requires the porous medium to have adjustable surface characteristics and a pore size range of tens of micrometers, which allows the liquid to permeate but blocks out gas below a critical differential pressure. Fast wicking process also requires a macroporous monolith to have a high permeability. Additionally, the practical use of such porous materials in wicking application requires a geometry size easy to scale up (eg. cylinder shape: diameter 3 cm, height at least 5 cm). Satisfying all these requirements propose a great challenge for the material design and preparation.

The critical working conditions of cryogenic wicking require the materials to be robust and the thermal properties influence the heat transfer during the wicking process. Besides, the thermal properties and mechanical properties of ceramic monoliths at cryogenic temperatures can be quite different from room temperature. Therefore, the mechanical properties and thermal properties at both temperatures need to be investigated.

The aim of this work can therefore be divided into two parts: The first part is to develop the macroporous polymer derived ceramic monolith which meets the requirements for capillary transport of cryogenic liquids. The second part is to investigate the mechanical and thermal properties of such porous materials under cryogenic temperatures and improve their mechanical strength by optimizing the preparation parameters.

To achieve the above mentioned aim, the following approach was adopted, which was divided into several steps.

1. For preparing macroporous materials, there are a few methods available: direct foaming, sacrificial template, replica method etc. The requirements of small pore size and relatively large monoliths size limit the methods that can be employed; therefore freeze casting (sacrificial template) was chosen. Freeze casting method allows the pore size to be controlled from 1 to 100  $\mu\text{m}$  and monolith size easy to scale up. By using water instead of organic solvents as solvent and partially pyrolyzed preceramic precursor (fillers) as solid phase, the shrinkage of PDCs and the possibility of cracks formation can be greatly reduced. The high permeability (open porosity) can also be achieved by controlling the solid loading in the slurry. The surface characteristics can be adjusted by preparation parameters, such as solid loading, pyrolysis temperatures and different precursors etc.

To use polysiloxanes in a water-based process, the surface characteristics in terms of hydrophobicity/hydrophilicity need to be modified, so that the solid particles can be well dispersed in the slurry for freeze casting. In case of H44 as precursor, low temperature pyrolysis was chosen to improve the hydrophilicity. While for MK, it was composited with hydrophilic APTES to achieve the hydrophilic surface.

2. To investigate mechanical (compressive strength) and thermal properties, unidirectional freeze casting was applied to prepare unidirectional porous monoliths. Their properties in both directions, parallel and perpendicular to the pores, were investigated.

Investigation on the compressive strength at cryogenic temperatures was achieved by immersing the samples inside liquid nitrogen, which represented similar conditions as the cryogenic wicking. Different liquids and different low temperatures were studied to find out the influence of liquid and low temperature on the compressive strength. To optimize preparation parameters for high compressive strength monolith, influence of different precursors (H44 and MK) and different pyrolysis temperatures (600, 700, 1000 °C) on compressive strength was investigated.

The thermal properties at cryogenic temperature were focused on coefficients of thermal expansion, thermal conductivity and specific heat capacity. For better understanding the relation between porous structure and thermal properties, the experimental results and predictions from theory models were compared.

## 4. Characterization methods

The characterization of surface charges, particle size distribution, specific surface areas, porosity, thermal and mechanical properties etc. has been done in this work. Some background information of characterization methods regarding their principles as well as alternative methods are given here, and further detailed information about samples characterizations is given in the chapters 5, 6 and 7.

### 4.1 Zeta potential and particle size analysis

#### 4.1.1 Zeta potential

A colloidal dispersion consists of a dispersion medium (often water) and dispersion particles. Due to the surface charges on the particles, particles adsorb ions of opposite charges, forming a stern layer. Furthermore, ions of the same charges as the particles are also adsorbed outside the stern layer, forming a slipping plane. In Guoy-Chapman model, the stern layer and slipping plane together are called the double layer [1], as shown in Figure 4.1. The zeta potential ( $\zeta$ -potential) is the electric potential at the location of the slipping plane relative to a point in the bulk fluid away from the interface [2]. It is largely used to qualify the magnitude of the charges, which influences the colloidal dispersion stability greatly. Suspensions with low zeta potential tend to coagulate or flocculate, while suspensions possessing absolute zeta potential values higher than 30 mV are considered as stable [3]. Zeta potential measurements are useful for ceramics manufacturing, preparation of colloidal dispersion for cosmetics [4] and destroy undesirable colloidal dispersion during water and sewage treatment [5], etc.

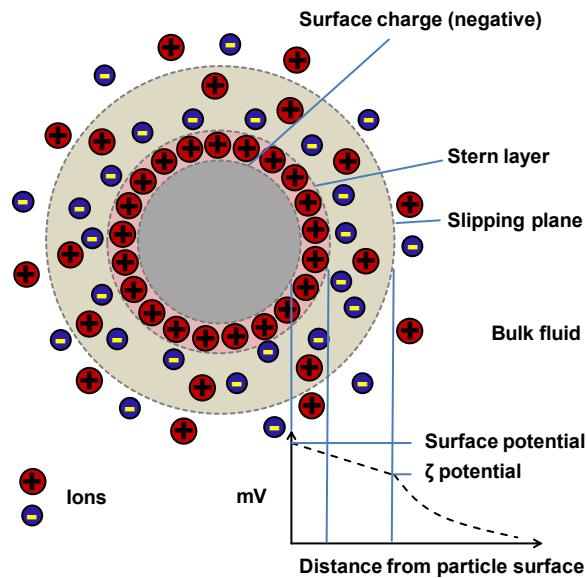


Figure 4.1: Schematic representation of zeta potential: ionic distribution and potential differences as a function of distance from the charged surface of a particle suspended in a medium, modified from [1]

### 4.1.2 Particle size analysis

Particle size of a real system usually ranges from nanometers to millimeter and the shape deviates from the ideal spherical particle. In most cases, the so called equivalent diameters are measured for determination of the particle size distribution. Particle size analyzers could be roughly organized in three groups according to the underlying methods used: counting, fractionation methods and macroscopic fitting methods. Counting methods count individual particles, including electrozone counter, microscopy counting or optical counter etc. Fractionation methods use an additional process or force to separate particles according to its size distribution and the quantities of separated different sizes are then detected by light or other detectors. Dynamic light scattering (DLS) and acoustic particle sizing are both macroscopic fitting methods. Dynamic light scattering utilizes time variation of scattered light from suspended particles under Brownian motion to obtain their hydrodynamic size distribution [6], which measures particles smaller than 1  $\mu\text{m}$ . Acoustic particle sizing is based on calculation of particle size distribution from the attenuation frequency spectra in the MHz range. During the measurement, ultrasound pulses are sent through the dispersions to be analyzed and the attenuated signal is then picked up by a sound transducer. It can measure particle size from 10 nm to 1000  $\mu\text{m}$  and is suitable to measure concentrated systems (often up to 50 wt %) [7].

### 4.2 Characterization of specific surface area

The specific surface area of a solid is defined as total surface area of a material per unit of mass ( $\text{m}^2\cdot\text{g}^{-1}$ ) or volume ( $\text{m}^2\cdot\text{m}^{-3}$  or  $\text{m}^{-1}$ ). It can be calculated from nitrogen adsorption and desorption data. The measurement is carried out at 77 K. Precise doses of nitrogen gas are consecutively introduced into the glass capillary tube. When the equilibrium is achieved for each dosage, the data is collected. The adsorbed volume of nitrogen (273.15 K and 101.3 kPa) versus relative pressure ( $P/P_0$ ) is recorded, where  $P_0$  is the vapor pressure of nitrogen at 77 K ( $P_0=101.3$  kPa). According to International Union of Pure and Applied Chemistry (IUPAC), adsorption isotherms in physical adsorption can be classified as one of 6 types [8] shown in Figure 4.2



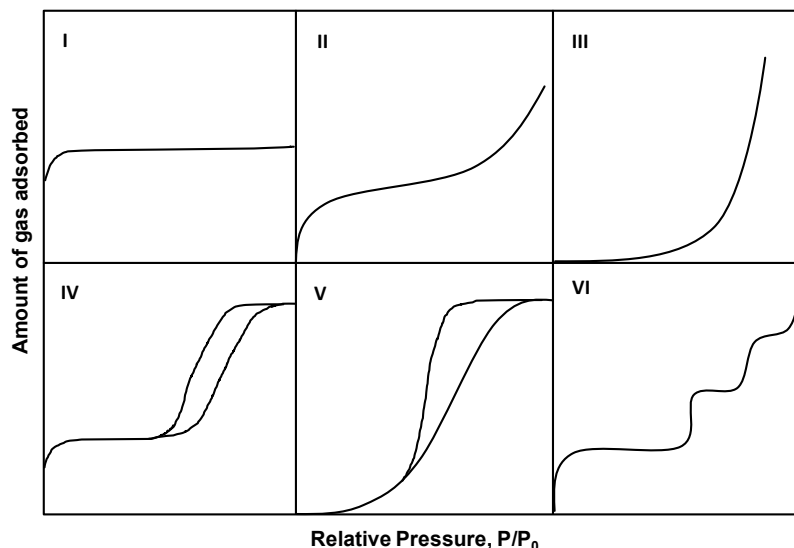


Figure 4.2: IUPAC classifications of adsorption isotherms.

Each type of isotherm reflects the interaction between samples surface and adsorbate and represents different porous structure. Type I is typical for materials with micropores (zeolites, active carbons and preceramic polymer pyrolyzed at low temperatures), representing a relatively strong interaction between nitrogen with the solid surface at low relative pressure. Type II isotherms represent nonporous materials, in which a relatively strong interaction between nitrogen with solid surface occurs. Type III isotherms describe nonporous material, but here the gas-surface interaction is weak. Type IV isotherms are typical for materials possessing mesopores, where the interaction is relatively strong, such as mesoporous silica SBA-15, etc. A hysteresis occurs during adsorption and desorption process, due to capillary condensation of nitrogen gas in mesopores, leading to differences of meniscus between adsorption and desorption process. Type V isotherms represent mesoporous materials, in which the interaction between gas and the surface is weaker than that between gas molecules. Type VI represents a stepwise monolayer adsorption of gas molecules on nonporous materials.

The specific surface area (SSA) can be calculated based on Brunauer–Emmett–Teller (BET) theory [9], which extended the Langmuir’s monolayer theory to multilayer adsorption. The BET equation (4.1) was derived on the basis of following hypotheses:

1. Surface is energetically homogeneous, which means that all the adsorption sites on the bare solid surface have the same adsorption energy.
2. There is no lateral interaction between adsorbed molecules.
3. The adsorption energies in all layers are the same and equal to the condensation energy of the adsorbate.

$$\frac{P}{v(P_0 - P)} = \frac{1}{v_m c} + \frac{c - 1}{v_m c} \left( \frac{P}{P_0} \right) \quad (4.1)$$

Where  $P$  is the pressure,  $c$  and  $v_m$  are two constants,  $P_0$  is the vapor pressure of nitrogen at 77K ( $P_0=101.3$  kPa) and  $v$  is volume of adsorbed adsorbate. For many adsorbents, the BET plot gives a good linear line in relative pressure range of 0.05 ~0.35, but deviates from the linear line in low or high pressure range. Usually,  $c$  and  $v_m$  are evaluated from the BET plots in the pressure range ( $P/P_0$ ) from 0.05 to 0.35, but the starting point and ending point of the BET should be carefully selected according to the character of the adsorbent.

### 4.3 Characterization of porous structure

According to International Union of Pure and Applied Chemistry (IUPAC) notation, micropores are defined as pore sizes smaller than 2 nm, mesopores sizes are between 2 to 50 nm, and macropores are larger than 50 nm. Specific methods are adopted for measuring pore sizes of different categories.

#### 4.3.1 Micro/mesoporosity measurement

Nitrogen adsorption and desorption measurement can be used to calculate the micropore and mesopore size distributions. For example, non-localized density functional theory (NLDFT) is used to calculate the pore distribution for micropores and mesopore [10]. In NLDFT, it is assumed that the adsorption density periodically changes from solid surface. Pore structure model (slit or cylindrical, cage) needs to be selected to determine parameters related to adsorptive and adsorbent ( $N_2$ ).

Mesopores are more commonly calculated by Barrett-Joyner-Halenda (BJH) model [11]. In type IV adsorption isotherms, hysteresis occurs, which means the equilibrium adsorption amount during desorption is larger than the one during adsorption. The hysteresis shape depends on the shape of mesopores. In case of cylinder shaped pore, pore radius can be obtained from equation (3.2)

$$r_p = t + r_k \quad (4.2)$$

Where  $t$  is the thickness of adsorption layer at the arbitrary pressure and  $r_k$  is the core radius of meniscus part, as shown in Figure 4.3. Pore volume can be calculated from equation (4.3)

$$V_{pn} = R_n \Delta V_n - R_n \Delta t_n c \sum_{j=1}^{n-1} A_{pj} \quad (4.3)$$

where  $A_p$  is the area of each pore,  $c$  is a value selected according to a peak position of pore size distribution curve,  $\Delta V$  is the certain amount of gas being desorbed between two equilibrium pressure,  $R_n = r_{pn}^2 / (r_{k1} + \Delta t_1)^2$ . Pore size distribution curve can be obtained by plotting  $\Delta V / \Delta r$  against pore radius.

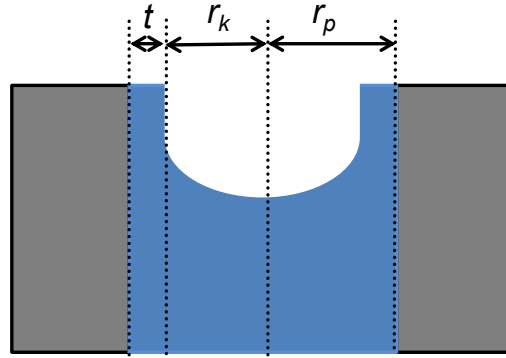


Figure 4.3: Nitrogen adsorption inside capillary.

### 4.3.2 Macroporosity measurement

Macroporosity can be measured with many methods, such as Archimedes method or Hg-intrusion porosimetry. Archimedes method only gives the value of open porosity, while Hg-intrusion porosimetry can measure porosity and pore size distribution.

In Archimedes method, the dry mass of sample ( $m_1$ ), the buoyancy mass ( $m_2$ ) and the wet mass ( $m_3$ ) are used to calculate open porosity ( $p_{op}$ ):

$$p_{op} = \frac{(m_3 - m_1)}{(m_3 - m_2)} \quad (4.4)$$

Mercury intrusion porosimetry allows measuring the volume and size of macropores (up to several hundreds of micrometers) and mesopores in solid porous substances [12]. The technique is based on the non-wetting behavior of mercury referring to a lot of solid materials. During the measurement, pressure is applied to let mercury penetrate through the open pores, as shown in Figure 4.4. The pore volume distribution as a function of their radius is calculated by measuring the quantity of mercury penetrated in the sample pores and the equilibrium pressure at which intrusion occurs. The pore size is inversely proportional to the applied pressure according to Washburn equation.

$$r = -2\pi\gamma \cos \theta \quad (4.5)$$

Where  $r$  is the pore radius (cylindrical shape),  $\gamma$  is the surface tension and  $\theta$  is the contact angle. Mercury has a surface tension from 0.473 to 0.485 N·m<sup>-1</sup> and a contact angle ranging from 117 to 141°. The purity of mercury influences the contact angle greatly, and can therefore affect the pore radii by as much as a factor of two [13]. When a pore has narrow openings but wider inner body, sufficient pressure needs to be applied to force mercury into the narrow openings. Therefore, only narrow open pore sizes are measured which is called ink-bottle effect. Notably, porous materials containing metals cannot be measured with this method due to the reaction of metals with mercury (amalgamation). Compressible materials cannot be used in this technique directly, due to incorrect pressure values.

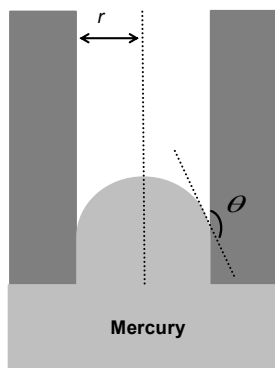


Figure 4.4: Mercury penetration into capillary.

### 4.4 Characterization of surface characteristics

The chemical composition of the surface can influence the properties of materials greatly. Therefore, it is very important to investigate the surface characteristics of the materials. Depending on the functional groups/atoms, the surface can be hydrophilic or hydrophobic.

Normally, surface characteristics are characterized by measuring contact angle. During the contact angle measurement with water as liquid, the solid is more hydrophilic when the contact angle is smaller than  $90^\circ$ . When the contact angle is larger than  $90^\circ$ , the solid is more hydrophobic. The contact angle is also influenced by the porous structure and the roughness of the surface [14].

Vapor sorption isotherms with polar and non-polar solvents can also be used to characterize the hydrophilicity or hydrophobicity. In this work, the surface characteristics were characterized by a simple vapor adsorption method. A polar solvent (water) and non-polar solvent (*n*-heptane) were used as solvents in closed Erlenmeyer flasks, the ratio of water adsorption to *n*-heptanes adsorption after equilibrium revealed the hydrophilic or hydrophobic property of the surface.

### 4.5 Compressive strength analysis

The strength of material deals with the behavior of solid materials subjected to stress and strain. Most common strengths are compressive strength (compression strength), tensile strength and flexural strength (bending strength). Compressive strength is the capacity of a material to withstand loads tending to reduce size, as opposed to tensile strength, which withstands loads tending to elongate. For ceramics, the tensile strength is usually less than the flexural strength, since the maximum stress acts in the whole volume of the body, while during bending it acts only in a thin region adjacent to the tension side of the bent sample. The compressive strength of ceramic materials is much stronger than the tensile strength, which is partly due to the brittle nature of ceramics, resulted from low mobility of the dislocation [15]. Therefore ceramics are largely used as structural components which stand the compression. The compressive strength is usually obtained from compression test by a universal testing machine, during which the

relation between stress and strain is recorded. A typical stress-strain curve of ceramic materials is shown in Figure 4.5.

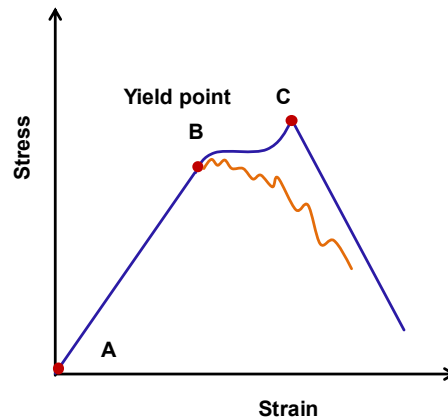


Figure 4.5: Typical stress-strain curve of ceramic materials.

During the loading, the material deforms elastically from the point A to B, which means the relation of stress and strain follows the Hooke's law:

$$\sigma = E \epsilon \quad (4.6)$$

Where  $\sigma$  is the stress,  $E$  is Yong's Modulus, and  $\epsilon$  is the strain. Point B is called yield point, where the material does not follow Hooke's law anymore, and the deformation is permanent. The compressive strength is calculated based on the highest stress (point C). Above this point, the stress will decrease sharply for ceramic material. However, for porous ceramics, pore deflection occurs, which makes the stress decrease gradually as shown by the orange line.

Compressive strength is influenced greatly by the testing parameters, such as sample size and strain rate. Therefore, compressive strengths are only comparable when testing parameters are the same.

The test value of compressive strength becomes smaller with the increasing specimen size, called size effect of compressive strength. It also varies with the geometries of the specimen, which can be explained by the different crack propagation patterns [16].

Additionally, the test values of compressive strength increase with increasing strain rate. This can be seen as that, the influence of defects inside the ceramics on compressive strength decreases with increasing strain rate [17]. For the identical specimen with identical crack size, the crack propagation gets limited during a high loading speed, while the crack grows larger at a low strain rate.

## 4.6 Characterization of thermal properties

### 4.6.1 Thermal conductivity

Thermal conductivity can be measured by steady-state and non-steady-state (or transient) techniques. The steady-state methods measure thermal properties by establishing a temperature difference that does not change with time, while transient techniques usually measure time-dependent energy dissipation process of a sample. The transient methods include  $3\omega$  method [18] and hot-wire method [19], and laser flash method, etc.

Taking laser flash method as an example, it measures thermal diffusivity directly. Thermal conductivity can be calculated based on the equation:

$$k_S = C_p \alpha \rho \quad (4.7)$$

Where  $k_S$  is the thermal conductivity,  $\alpha$  is the thermal diffusivity,  $C_p$  is the specific heat capacity, and  $\rho$  is the density of solid material [20]. Different techniques are chosen based on the materials' thermal conductivity and geometry (bulk or thin film) [21]. The size range of specimen and its corresponding measurement range of each method are shown in Figure 4.6 and Table 4.1.

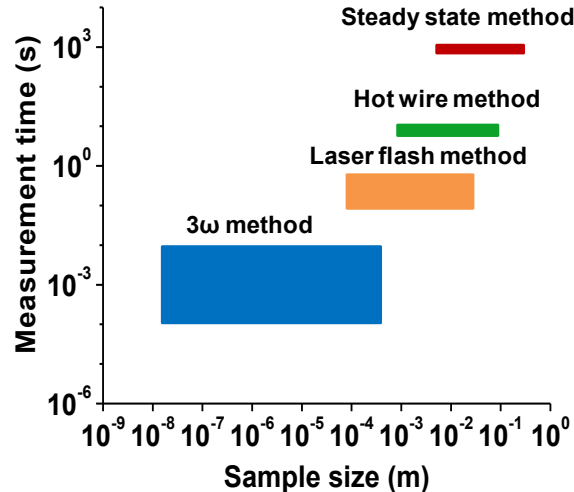


Figure 4.6: The size range of specimen and its corresponding measurement range for each method, modified from [21].

#### 4. Characterization methods

Table 4.1: Thermal conductivity range of each method [22]

Methods	Thermal conductivity at RT ( $W \cdot m^{-1} \cdot K^{-1}$ )	Temperature range	Materials
Laser Flash	$10^{-2}$ – $10^3$	-150–2800 °C	Polystyrene, wood, porous ceramics, refractory, silicon nitride, silver, copper, silicon carbide, diamond
Hot Wire-1	$10^{-2}$ – $10^3$	RT–1500 °C	Wood, porous ceramics, refractory, silicon nitride
Hot Wire-2	$10^{-3}$ – $10^0$	-160–250 °C	Vacuum isolation  Air, Microporous isolation, Polystyrene, wood, porous ceramics, refractory
Heat Flow Meter	$10^{-3}$ – $10^0$	-30–100 °C	Vacuum isolation  Air, Microporous isolation, Polystyrene, wood, porous ceramics, refractory

In this thesis, the thermal conductivity was measured by a steady-state technique, which is based on Fourier's Law. The scheme of the measurement cell in this work is shown in Figure 4.7. In the steady-state measurement, the thermal conductivity and interfacial thermal conductance are determined by measuring the temperature difference at a separation (distance) under the steady-state heat flow  $Q$  through the sample. The following shows one-dimensional Fourier conduction:

$$Q = -kA \frac{dT}{dx} \quad (4.8)$$

Where  $Q$  is the rate of heat flow,  $k$  is the thermal conductivity,  $A$  is the cross-sectional area, and  $dT/dx$  is the temperature gradient [23].

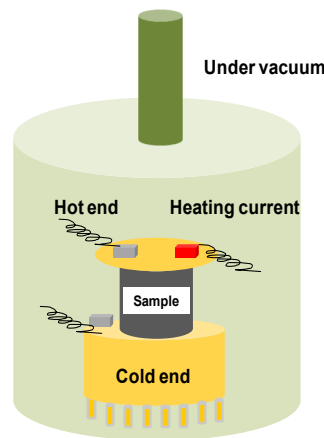


Figure 4.7: Scheme of measurement cell of a steady-state technique.

### 4.6.2 Specific heat capacity

Specific heat capacity at constant pressure ( $C_p$ ) can be measured directly by differential scanning calorimetry (DSC). The principle is shown in the following equation (4.9).

$$\frac{dQ}{dt} = mC_p \frac{dT}{dt} \quad (4.9)$$

Where  $dQ/dt$  is the heat flow rate,  $m$  is the sample mass,  $C_p$  is the specific heat and  $dT/dt$  is the heating rate.

In conventional DSC,  $C_p$  is generally calculated from the difference in heat flow between a blank run (empty pan, reference) and a sample run under identical conditions, based on equation (4.10). Sapphire is the traditional material used to calibrate a DSC for  $C_p$  measurements, due to its linear behavior of specific heat to temperature rise, with values ranging from about  $0.4 \text{ J}\cdot\text{g}^{-1}\cdot\text{K}^{-1}$  at  $-173.15 \text{ K}$  to around  $1.04 \text{ J}\cdot\text{g}^{-1}\cdot\text{K}^{-1}$  at  $373.15 \text{ K}$  [24].

$$C_p = K_{C_p} \times \frac{Q_s - Q_r}{\left(\frac{dT}{dt}\right)} \quad (4.10)$$

Where  $K_{C_p}$  is the  $C_p$  cell calibration constant, which can be obtained from the measurement with sapphire, and  $Q_s$ ,  $Q_r$  are the heat flow of the sample and reference.

### 4.6.3 Coefficient of thermal expansion

The degree of expansion divided by the change in temperature is called the coefficient of thermal expansion (CTE), and it varies with temperature. Several types of coefficients have been developed: volumetric, area and linear. The linear thermal expansion coefficient is defined as:

$$\alpha_L = \frac{1}{L} \frac{dL}{dT} \quad (4.11)$$

Where  $L$  is a particular length measurement and  $dL/dT$  is the rate of change of linear dimension per unit change in temperature.

Determining CTE requires measuring of displacement and temperature when the material is undergoing a thermal cycle. There are various ways to measure the displacement, such as mechanical or capacitance dilatometers, optical imaging, x-ray diffraction patterns or strain gauge, etc. [25].

In this thesis, CTEs were measured with strain gauge. A picture of the sample cell and strain gauge used in this thesis is shown in Figure 4.8. For this method, quartz or vitreous silica of known thermal expansion should be used as the reference, and the measurement cell is put



inside oven or liquid bath to get the desired temperature range [26]. A resistance strain gauge is glued on the surface of a specimen, and the instantaneous strain is measured during the temperature change. The temperature is measured by a thermocouple, the tip of which is embedded in the vacuum cement. During the measurement, temperature change results in the output of gauge changes accordingly.

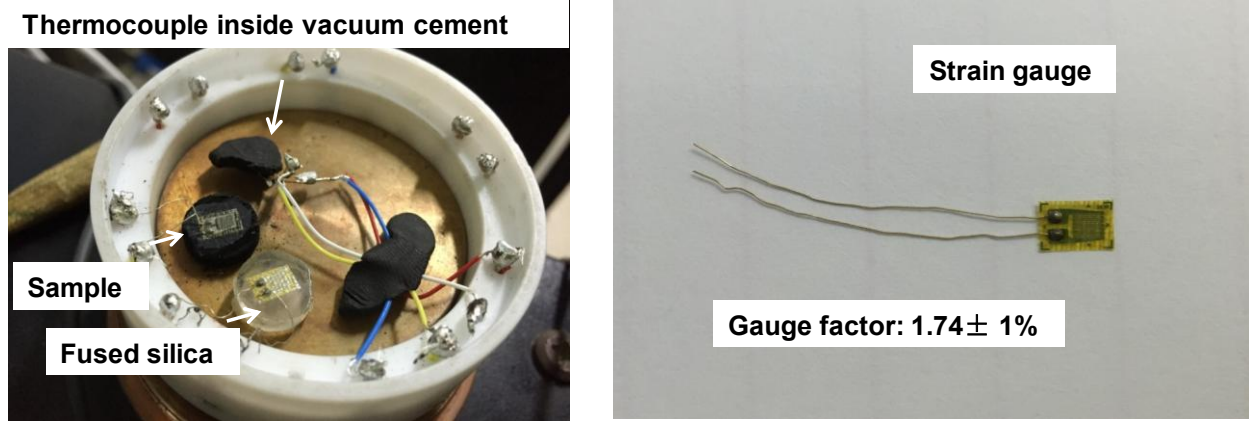


Figure 4.8: Sample cell and strain gauge for CTE measurement.

The relative change in length between the sample and fused silica is calculated directly from the following equation:

$$\frac{\Delta l}{l} = \frac{R_g \Delta R}{FR^2} \quad (4.12)$$

Where  $R_g$  is the resistance of the gauge,  $R$  is a large resistance connected in parallel with  $R_g$ ,  $\Delta R$  is the change of this resistance required to maintain the bridge balance and  $F$  is the gauge factor of the strain gauge [26].

#### 4.7 Permeability measurement

Permeability reflects the effectiveness of the interaction between the property of a fluid and the property of a medium. Permeability is part of the proportionality constant in Darcy's law which relates flow rate and fluid physical properties (e.g. viscosity) to a pressure gradient applied to the porous media, as shown in equation (4.13).

$$K_p = v\mu \frac{\Delta x}{\Delta P} \quad (4.13)$$

Where  $v$  is the superficial fluid flow velocity through the medium,  $k$  is the permeability of a medium,  $\mu$  is the dynamic viscosity of the fluid,  $\Delta P$  is the applied pressure difference, and  $\Delta x$  is the thickness of the bed of the porous medium [27].

Besides Darcy's law, Forchheimer's equation is also commonly used to calculate permeability. The Darcy's law considers only the viscous effects on the fluid pressure drop and establishes the linear dependence between the pressure gradient and the fluid velocity through the medium, and is accurate at very low velocities. Forchheimer's equation considers that the pressure gradient displays a parabolic trend with an increase in fluid velocity due to the contributions of inertia and turbulence [28]. In this thesis, permeability is calculated based on Darcy's law.

Permeability to gases can be very different from the permeability to liquids, which can be explained by the compressibility of the liquid or gas. Comparing with liquids, the gas flow velocity at the exit of the porous medium becomes higher than at the entrance, which affects the pressure drop profile. The molecular mean free path of gas is much higher than liquid due to the compressibility. When the gas mean free path is comparable to the pore size, Knudsen diffusion happens, and the permeability equation (4.13) should be corrected [29]. The permeability constant determined with gas depends upon the nature of gas; however, the permeability constant of a porous medium is generally independent of the fluid used as long as the flow rate is proportional to the pressure gradient [30]. Most of the SiOC materials synthesized in this thesis have mesopores as well as macropores; therefore, using gases to measure permeability may make the measurement error larger than actual value, although the Knudsen diffusion effect should not play a great role in the permeability.

The permeability can be measured by falling head permeability test or stand head permeability test [31]. In this thesis, the set-up was modified: water was used as the penetrating medium, and the pressure was adjusted by using compressed air. The compressed air was connected to the water reservoir. Before the measurement, the sample trapped inside a rubber jacket was put at the bottom of the container. Then certain amount of water was added, the set up was sealed and the gas pressure was applied. Pressure meter showed the pressure relative to the ambient pressure. The weight of the water dripping out was measured by a balance and the time consumed was used to calculate the filter velocity of water. The pressure controller was used to adjust the pressure applied on the surface of water; therefore, permeability at different pressures can be measured. A scheme of the set-up is shown in Figure 4.9.

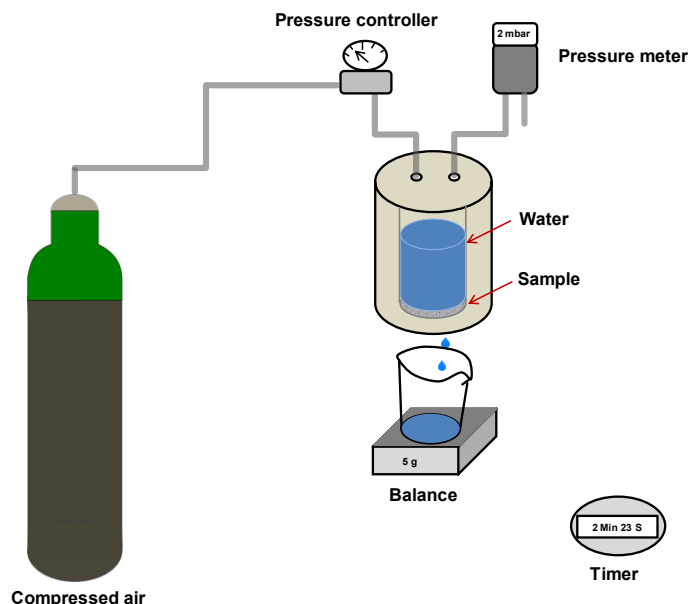


Figure 4.9: Modified drop head permeability measurement set up.

The error of the measurement comes from hydraulic pressure, since the relative pressure was measured above the water surface instead of the sample surface. Due to the limited amount of water (height < 13 cm), the hydraulic pressure can be neglected at the high relative pressure. Therefore, the permeability results have relatively large error at low pressure (relative pressure < 250 mbar), and have a high accuracy at high pressure (relative pressure > 250 mbar).

Due to the anisotropic structure of the monoliths prepared in the thesis, the permeability is also expected to show anisotropy. Only the directional permeability (temperature gradient direction during freezing) was measured in this work.

## References

- [1] A. Liese, L. Hilterhaus, Evaluation of immobilized enzymes for industrial applications, *Chem. Soc. Rev.* 42 (2013) 6236–6249.
- [2] B. J. Kirby, *Micro- and nanoscale fluid mechanics: Transport in microfluidic devices*, ISBN 978-0-521-11903-0, Cambridge University Press, 2010, New York.
- [3] N. Gibson, O. Shenderova, T. J. M. Luo, S. Moseenkov, V. Bondar et al., Colloidal stability of modified nanodiamond particles, *Diamond Relat. Mater.* 18 (2009) 620–626.
- [4] S. Kokura, O. Handa, T. Takagi, T. Ishikawa, Y. Naito et al., Silver nanoparticles as a safe preservative for use in cosmetics, *Nanomedicine: Nanotechnology, Biology, and Medicine* 6 (2010) 570–574.

- [5] X. H. Guan, G. H. Chen, C. Shang, Re-use of water treatment works sludge to enhance particulate pollutant removal from sewage, *Water Res.* 39 (2005) 3433–3440.
- [6] R. L. Xu, Progress in nanoparticles characterization: Sizing and zeta potential measurement, *Particuology* 6 (2008) 112–115.
- [7] D. J. McClements, Ultrasonic measurements in particle size analysis, encyclopedia of analytical chemistry, ISBN 0471976709, John Wiley & Sons Ltd, 2006, Chichester.
- [8] K. S. W. Sing, Reporting physisorption data for gas/solid systems with special reference to the determination of surface area and porosity, *Pure Appl. Chem.* 57 (1985) 603–619.
- [9] S. Brunauer, P. H. Emmett, E. Teller, Adsorption of gases in multimolecular layers, *J. Am. Chem. Soc.* 60 (1938) 309–319.
- [10] J. Landers, G. Y. Gor, A. V. Neimark, Density functional theory methods for characterization of porous materials, *Colloids and Surf. A Physicochem. Eng. Asp.* 437 (2013) 3–32.
- [11] E. P. Barrett, L. G. Joyner, P. P. Halenda, The determination of pore volume and area distributions in porous substances. I. computations from nitrogen Isotherms, *J. Am. Chem. Soc.* 73 (1951) 373–380.
- [12] H. Giesche, Mercury porosimetry: a general (practical) overview, *Part. Part. Syst. Charact.* 23 (2006) 1–11.
- [13] F. Moro and H. Böhni, Ink-bottle effect in mercury intrusion porosimetry of cement-based materials, *J. Colloid Interface Sci.* 246 (2002) 135–149.
- [14] A. B. D. Cassie, S. Baxter, Wettability of porous surfaces, 1944, *Trans. Faraday Soc.* 40 (1944) 546–551.
- [15] A. Koller, Structure and properties of ceramics, Materials science monographs 80, ISBN 0-444-98719-3, Elsevier, 1994, Amsterdam.
- [16] J. R. Viso, J. R. Carmona, G. Ruiz, Shape and size effects on the compressive strength of high-strength concrete, *Cem. Concr. Res.* 38 (2008) 386–395.
- [17] J. Lankford, Mechanisms responsible for strain-rate-dependent compressive strength in ceramic materials, *J. Am. Chem. Soc.* 64 (1981) C33–C34.
- [18] S. A. Putnam, D. G. C. J. Ash, L. S. Schadler, High-precision thermal conductivity measurements as a probe of polymer/nanoparticle interfaces, *J. Appl. Phys.* 94 (2003) 6785–6788.
- [19] Y. A. Landa, E. Y. Litovskii, B. S. Glazachev, N. A. Puchkelevich, A. V. Klimovich, Hot-wire method of determining the thermal conductivity of refractory materials, *Refractories*, 19 (1978) 561–565.
- [20] W. J. Parker, R. J. Jenkins, C. P. Butler, G. L. Abbott, Flash method of determining thermal diffusivity, heat capacity, and thermal Conductivity, *J. Appl. Phys.* 32 (1961) 1679–1684.
- [21] D. L. Zhao, X. Qian, X. K. Gu, R. G. Yang, Measurement techniques for thermal conductivity and interfacial thermal conductance of bulk and thin film materials, *J. Electron. Packag.* 138 (2016) 040802 (1–19).
- [22] Netzsch, n.d., retrieved from <https://www.netzsch-thermal-analysis.com/en/products-solutions/thermal-diffusivity-conductivity/lfa-457-microflash/>
- [23] F. Kreith, W. Z. Black, Basic heat transfer, Harper and Row Publishers, 1980, New York.

- [24] D. A. Ditmars, S. Ishihara, S. S. Chang, G. Bernstein, Enthalpy and heat-capacity standard reference material: synthetic sapphire ( $\alpha$ -Al<sub>2</sub>O<sub>3</sub>) from 10 to 2250 K, *J. Res. Nat. Bur. Stand.* 87 (1982) 159–163.
- [25] J. D. James, J. A. Spittle, S. G. R. Brown, R. W. Evans, A review of measurement techniques for the thermal expansion coefficient of metals and alloys at elevated temperatures, *Meas. Sci. Technol.* 12 (2001) R1–R15.
- [26] A. E. Clark, B. F. Desavage, R. Bozorth, Anomalous thermal expansion and magnetostriction of single-crystal dysprosium, *Phys. Rev.* 138 (1965) A216–A224.
- [27] J. F. Siau, *Transport processes in wood*, ISBN 978-3-642-69213-0, Springer, 1984, Berlin.
- [28] M. Scheffler, P. Colombo, *Cellular ceramics: structure, manufacturing, properties and applications*, ISBN 978—527-31320-4, Wiley-VCH Verlag, 2005, Weinheim.
- [29] A. S. Ziarani, R. Aguilera, Knudsen's permeability correction for tight porous media, *Transp. Porous Med.* 91 (2012) 239–260.
- [30] L. J. Klinkenberg, *The permeability of porous media to liquids and gases*, American Petroleum Institute, 1941, New York.
- [31] H. W. Olsen, R. W. Nichols, T. L. Rice, Low gradient permeability measurements in a triaxial system, *Geotechnique* 35 (1985) 145–157.

## 5. Adjusting hydrophilicity of polysiloxane by thermal decomposition for freeze casting

*Adapted from: Hierarchically ordered micro/meso/macroporous polymer-derived ceramic monoliths fabricated by freeze casting*

*Published in: Journal of the European Ceramic Society 36 (2016) 51–58*

*Received 1 July 2015, Revised 11 September 2015, Accepted 13 September 2015, Available online 26 September 2015.*

*Authors: Huixing Zhang, Pedro D'Angelo Nunes, Michaela Wilhelm\* and Kurosch Rezwani  
University of Bremen, Advanced Ceramics, Am Biologischen Garten 2, IW3, Germany*

*\* Corresponding author. E-mail address: mwillhelm@uni-bremen.de*

*DOI: 10.1016/j.jeurceramsoc.2015.09.018*

*Reprint (adapted) with permission from Elsevier Ltd., license number: 4151390851285*

### Abstract

A hierarchically-ordered macro/meso/microporous SiOC monolith was obtained via freeze casting using commercial polysiloxane as a raw material and silica sol as a binder and template source. The pre-ceramic polymer polysiloxane was pyrolyzed at 600 °C to produce a hydrophilic surface; higher temperatures would fully decompose the organic groups. When silica sol and polysiloxane precursor were combining freeze casting method, after pyrolysis a polymer-derived SiOC ceramic monolith with lamellar pore morphology and a hierarchically-ordered pore structure was obtained. Decomposition of the polysiloxanes results in the development of micropores, and particle packing bound by silica sol is believed to be responsible for the mesopore formation. Macro/mesoporous hierarchically-ordered ceramics with a specific surface area of 74 m<sup>2</sup>·g<sup>-1</sup> are preserved at pyrolysis temperatures as high as 1000 °C. The influence of H44-derived filler amount (10-40 wt%), freezing temperature (-20 °C, -80 °C, -150 °C), and pyrolysis temperature (600 °C, 700 °C, 1000 °C) on open porosity, pore size distribution, and surface characteristics were investigated.

### 5.1 Introduction

Macroporous monolithic ceramics may possess a high permeability with respect to gases and liquids and have found uses in a wide variety of industrial applications, including catalysis support [1], scaffolding for bone replacement [2], continuous flow capillary microreactors [3], filters for diesel soot [4], and liquid metal [5]. The incorporation of micropores (pore size <2 nm) and mesopores (2 nm < pore size < 50 nm) into a macroporous structure (pore size >50 nm) can combine improved mass transport with high surface area and large pore volumes, significantly broadening a material's range of applicability [6]. Fabrication of hierarchically-ordered porous ceramics normally involves the introduction of pores during preparation via some combination of the following methods: natural templating, surfactant templating, foaming, or freeze casting [7–10].

Freeze casting is a special kind of sacrificial templating method; the solvent solidifies and crystallizes (eg. ice) during the freezing process, sublimates, and leaves pores behind [11]. Freezing rate, solvents used, and precursor particle size will all have an influence on the final macroporous structure [12]. Water and organic solvents, like camphene and *tert*-butyl alcohol, are commonly used for freeze casting; the solvent used will influence the pore shape resulting from crystallization (eg. lamellar, cellular, or dendritic) [11, 13, 14]. Water is often used with inorganic ceramic powder suspensions (eg.  $\text{Al}_2\text{O}_3$ , SiC,  $\text{SiO}_2$ ,  $\text{ZrO}_2$ ) [11, 15] and the green body obtained is then sintered to get a final macroporous monolith. For the preparation of SiC monolith using inorganic precursors, in order to get a mechanically strong monolith, sintering temperatures higher than 1400 °C are normally required [16, 17]. For preceramic precursors, camphene and *tert*-butyl alcohol have also been used to fabricate macroporous SiOC and SiC monoliths by freeze casting and pyrolysis [13, 14].

The pre-ceramic precursors are polymers which can be converted into a ceramic material (SiC, SiCN, SiOC, etc.) by heat treatment in an inert atmosphere at temperatures in the range of 1000 to 1400 °C [18]. Polymer-derived ceramics, which are prepared at lower pyrolysis temperatures (500–1000 °C), have porosities at all pore diameter scales and surface characteristics [19, 20]. Some studies on dendritic or cellular pore morphologies of SiOC or SiC ceramics by freeze casting using preceramic polymer as precursor using camphene and *tert*-butyl alcohol has been performed [13,14]. However, the degree of cross-linking needs to be carefully monitored. Insufficient cross-linking will lead to poor mechanical integrity, and excessive cross-linking of polymer solution will cause gelation before freezing. To the best of our knowledge, as of this writing, there are no studies combining pre-ceramic precursors with  $\text{H}_2\text{O}$  to prepare porous SiOC materials with a lamellar structure.

Hierarchical micro/macroporous SiOC monoliths have been fabricated by using a direct foaming method with polysiloxane in the authors' working group [21]. However, in this work, water is used as the pore templating agent, and polysiloxane is used as the precursor for the fabrication of lamellarly structured porous SiOC monoliths via freeze casting. A trimodal micro-/meso-/macroporous structure were created by combination of decomposition of preceramic precursor with particle packing porosity and with ice templating. First, the surface characteristics of the polysiloxane precursor H44 was altered from hydrophobic to more hydrophilic by partially decomposed polysiloxane in an atmosphere of inert gas to "H44-derived filler" [22]. Then, this filler is mixed with silica sol, which is used as the binder and water-containing phase. The influences of the pyrolysis temperature, freezing temperature, and precursor composition on specific surface area, porosity, pore size distribution, and surface characteristics were studied. This method should enable the fabrication of large amounts of bulk monolith by reducing the very high volumetric shrinkage and an appreciable density increase during polymer to ceramic conversion. Adapting the water-based freeze casting method to the fabrication of polymer-derived ceramic monoliths offers the possibilities of generating a hierarchical pore structure with tailorable properties for different applications.

## 5.2 Experimental details

### 5.2.1 Material

A commercial methyl phenyl polysiloxane powder (Silres<sup>®</sup> H44, Wacker Chemie AG) was used to prepare the H44-derived filler. Silica sol (SiO<sub>2</sub> nanoparticles, 8 nm, 30%wt BegoSol<sup>®</sup> K, BEGO) was used as the binder and water-containing phase. Polyacrylic acid (PAA, Syntran 8140, Interpolymer) was added to adjust the pH value to ensure the complete condensation reaction of silica sol during the freezing process.

### 5.2.2 Processing

#### 5.2.2.1 H44-derived fillers

The H44 was pre-cross-linked using a multi-stage heat treatment in air at 80 °C, 140 °C and 200 °C (all dwell times 2 h), with a heating rate of 60 °C·h<sup>-1</sup> in between dwell times. The pre-cross-linked polysiloxane pieces were then pyrolyzed at 600 °C under a nitrogen atmosphere. The pyrolyzed samples were then ground with a grinder drive (MF 10 basic Microfine grinder drive, IKA) equipped with a 250 µm sieve grating. The resulting powder was then transferred to a planetary ball milling machine (PM 400, Retsch) and ground at 350 r·min<sup>-1</sup> for 4 h to produce a very fine powder.

#### 5.2.2.2 Macroporous polymer-derived ceramic monolith

H44-derived fillers were added to silica sol in amounts as given in Table 5.1, and mixed with a rotating mixer. The pH of this suspension was adjusted to 6–7 by the addition of polyacrylic acid. The resulting slurry was then placed under vacuum to remove bubbles created during stirring, then quickly transferred to aluminium moulds and placed in freezers at various temperatures (given in Table 5.1) until completely frozen. In order to reduce thermal stress induced by heating, the frozen body was transferred to a -20 °C freezer for 1 hour and then to a -4 °C freezer for 3 hours before drying in a climate chamber. The climate chamber was set to room temperature, with humidity between 85% and 95% for 5 days. During the drying step, more than 90% of water in the sample is removed, and residual water can be removed further during the cross-linking step. The “green o dies” were then cross-linked using a multi-stage heat treatment in air at 80 °C, 140 °C, and 200 °C (all dwell times 2 h), with a heating rate of 60 °C·h<sup>-1</sup> in between dwell times. Finally, the samples were pyrolyzed at various temperatures (given in Table 5.1) under an atmosphere of nitrogen. The preparation steps of the macroporous polymer-derived ceramic monoliths are shown in Figure 5.1.



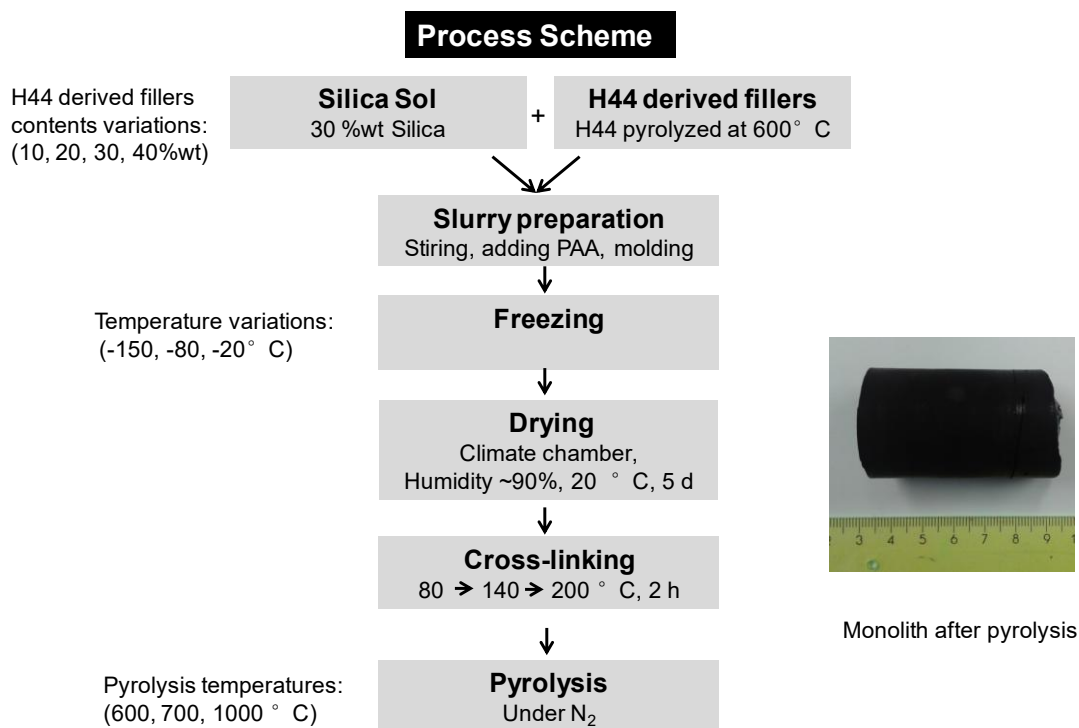


Figure 5.1: Process scheme, parameter variation of synthesized samples and monolithic structure of pyrolyzed sample.

Sample compositions were varied during preparation by varying the weight ratio of H44-derived fillers (10–40 wt%) to silica sol (90–60 wt%). Three freezing temperatures and three pyrolysis temperatures were investigated: -150, -80 and -20 °C; and 600, 700, and 1000 °C, respectively. Full information, including sample nomenclature is given in Table 5.1. For example, the name H44-10wt-150-xxx means that the weight percentage of H44-derived filler is 10%, the remaining 90% is silica sol, freezing temperature is -150 °C, and the sample was pyrolyzed at a temperature of xxx.

Table 5.1: Prepared materials and their composition, process, and pyrolysis parameters. Note that the solid contents in final monolith also include silica nanoparticles in silica sol. (\*Water content was calculated based on the water content in silica sol. The solid phase includes H44-derived filler and silica nano-particles, and for samples with 10, 20, 30, and 40wt% of H44-derived filler, solid loading equals to 37, 44, 51 and 58wt%, respectively.)

Material Denotation	H44-derived filler [wt%]	Silica sol* [wt%]	Freezing temperature [°C]	Pyrolysis temperature [°C] (xxx)
H44-10wt-150-xxx	10	90	-150	600/700/1000
H44-20wt-150-xxx	20	80	-150	600/700/1000
H44-30wt-150-xxx	30	70	-150	600/700/1000

H44-40wt-150-xxx	40	60	-150	600/700/1000
H44-40wt-80-xxx	40	60	-80	600/700/1000
H44-40wt-20-xxx	40	60	-20	600/700/1000

### 5.2.3 Characterization

Zeta potential was measured in order to get information on surface charges and to evaluate the stability of the suspension. Zeta potential of the H44-derived filler was analysed using Dispersion Technology Zeta & Size 1200 (Dispersion Technology Inc). The morphology of the H44-derived filler and pyrolyzed samples was analysed via scanning electron microscopy (SEM, Camscan Series 2, Obducat CamScan Ltd.); sample specimens were first sputtered with gold (K550, Emitech, Judges Scientific plc.). Macroporosities of the monoliths were determined via mercury intrusion porosimetry (Pascal 140/440, POROTEC GmbH). Specific BET surface areas and BJH pore size distributions were determined by nitrogen adsorption and desorption isotherms measured at 77 K using a Belsorp-Mini (Bel Japan, Inc.). The samples were degassed at 120 °C for 3 hours. Before degassing, the monolith materials were ground and sieved with a 300 µm mesh sieve in order to minimize nitrogen diffusion effects during the measurements. Water vapour and *n*-heptane adsorption measurements were carried out by placing vessels with ~0.5 g of sample powder (particle sizes ≤ 300 µm) inside closed Erlenmeyer flasks filled with the solvent at equilibrium with its vapour phase at room temperature. Samples were weighed at the start and end of a 24 hour measurement period in order to determine the vapour uptake of the material. Later, the uptake was recalculated into g·m<sup>-2</sup> using the BET surface of the materials.

## 5.3 Results

### 5.3.1 Properties of H44-derived fillers

The H44 precursor, which contains phenyl and methyl groups, is very hydrophobic. Thus, the properties of H44-derived fillers had to be modified in order to allow them to mix with water during freeze casting. When the H44 precursor is pyrolyzed at 600 °C, the decomposition of phenyl group occurs, resulting in a hybrid material. Pre-pyrolyzed H44, which would not cross-links further (only if are some –OH groups remaining), and act to fill the space, is therefore referred to as H44-derived filler.

The planetary ball milling machine was used to reduce the particle size of the H44-derived filler; in freeze casting, the filler particle size greatly influences the pore structure [12]. Dynamic light scattering measurements indicated a particle size range from 100 to 1000 nm, however, they display a tendency to aggregate, as shown in Figure 5.2a.

A surface charge on the particle was created predominantly by the decomposition of phenyl groups during pyrolysis at 600 °C. When the particles are mixed with water, the absolute value of the zeta potential can be used to indicate the stability of the suspension. Values between 1

and 10 mV indicate unstable suspensions, values between 10 and 30 mV indicate that the suspension exhibits initial, temporary particle stability in de-ionized water [23, 24], and values above 30 mV suggest that the suspension is very stable. For the H44-derived filler suspended in water, the absolute value of zeta potential is found to be more than 10 mV, shown in Figure 5.2b, indicating a initial stability (up to 1 hour; the freezing process takes only a few minutes at  $-150\text{ }^{\circ}\text{C}$ ).

Compared to water, the negatively charged H44-derived fillers had higher stability in anionic colloidal silica, due to stronger inter-particle repulsion. The pH value of the slurry also influences the zeta potential of particles, and thus the suspension stability. A slurry pH value of 6 to 7 was experimentally determined to produce the mechanically strongest monoliths after freezing. The cross-linking (condensation) rate between silica particles is greatly influenced by the pH of the slurry; this effect allows silica to act as a binder during the preparation process. A pH value below 6 led to suspensions having very low stability, while pH values of 8 to 11 lead to insufficient cross-linking of silica sol during freezing process. When the slurry was prepared with a  $\text{pH} > 11$ , gelation occurred before freezing could commence. Radial shrinkage of samples pyrolyzed at  $600\text{ }^{\circ}\text{C}$ ,  $700\text{ }^{\circ}\text{C}$ , and  $1000\text{ }^{\circ}\text{C}$ , was observed to be 3%, 4%, and 11% respectively.

Powder XRD analysis (Appendix Figure A1) confirms that the final product is structurally amorphous (no SiC or  $\text{SiO}_2$  peaks are detected). SiOC is not a single stoichiometric phase, but instead built from nanodomains of amorphous  $\text{SiO}_2$  and carbon; the material produced in this work is a SiOC material, having varying carbon contents and domain sizes. Wherein the sample contains especially for high contents of silica particles, it may also be described as  $\text{SiO}_2$  nanoparticles embedded in a SiOC ceramic matrix.

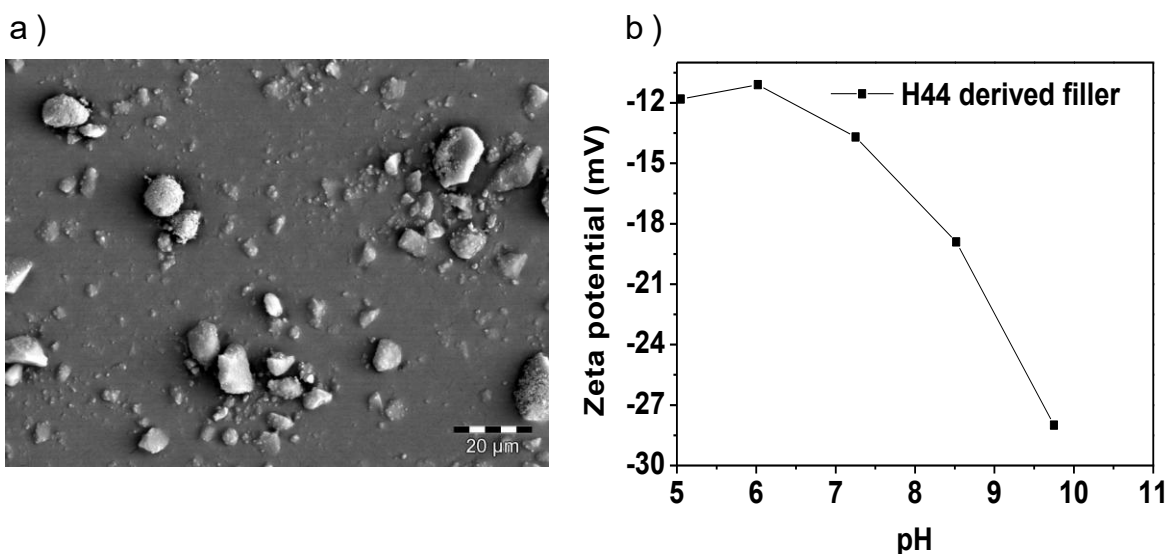


Figure 5.2: a) SEM images of H44-derived fillers after planetary milling at  $350\text{ r}\cdot\text{min}^{-1}$  for 4 hours, b) Zeta potential of the H44-derived filler in de-ionized water.

### 5.3.2 Pore structure and porosity

#### 5.3.2.1 Effect of freezing temperature on pore structure

The pore structure and porosity depends heavily on the freezing process. During freezing, the ice crystals tend to nucleate at the bottom surface of the cylindrical mould, growing upwards along the axis. However, due to the low thermal conductivity of the H44-derived filler materials, ice crystal growth inward from the circumference of the mould quickly comes to dominate the growth structure of the monolith. The ice growth forms anisotropic pore structures [25].

a) H44-40wt-150-1000

b) H44-40wt-80-1000

c) H44-40wt-20-1000

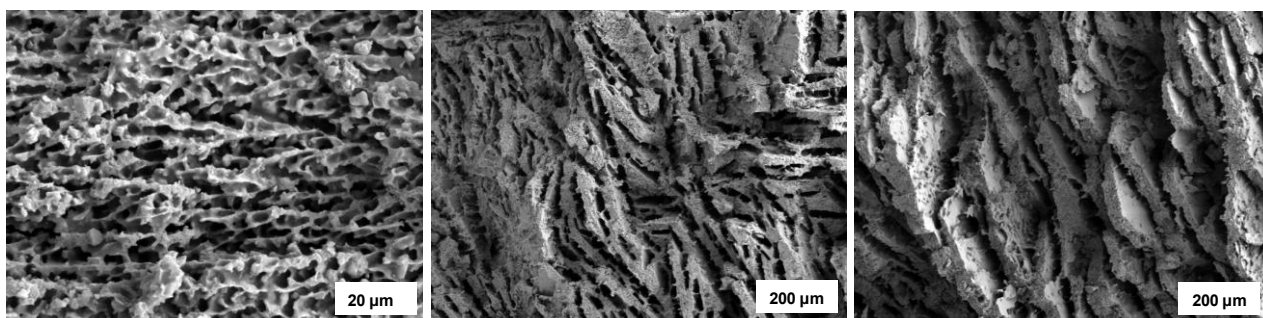


Figure 5.3: SEM images of pyrolyzed monoliths with different freezing temperatures. Horizontal length of the white boxes represents the sizes given therein.

The pore structures of the monolith are shown in Figure 5.3. The pore morphologies of pyrolyzed monoliths differ with changes in freezing temperature (varied freezing rates). The samples, which were frozen at  $-150\text{ }^{\circ}\text{C}$ , display a tubular (also described in other literature as “columnar”) pore structure, while the samples frozen at  $-80\text{ }^{\circ}\text{C}$  and  $-20\text{ }^{\circ}\text{C}$ , and show a lamellar pore structure. The pore sizes increase with increasing freezing temperature (decreased freezing rate). The pore diameters of H44-derived samples range from less than  $10\text{ }\mu\text{m}$  ( $-150\text{ }^{\circ}\text{C}$ ), to  $20\text{ }\mu\text{m}$  ( $-20\text{ }^{\circ}\text{C}$ ). Figure 5.3c shows how the wall is constructed from particles, which are the H44-derived filler materials. The macropore size can also be analyzed with Hg intrusion porosimetry, which provides additional information about the porosity.

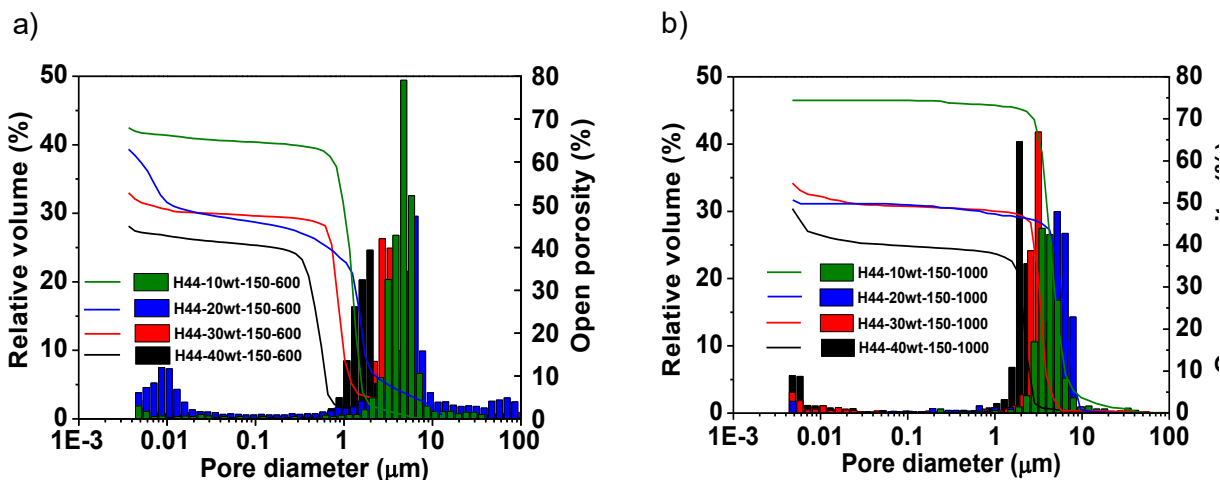


Figure 5.4: Pore size distribution versus relative pore volume (coloured columns) and open porosity curves (coloured lines) obtained from Hg-porosimetry of pyrolyzed samples: a) Samples with different H44-derived filler amounts, pyrolyzed at 600 °C; b) Samples with different precursor ratios, pyrolyzed at 1000 °C.

Figure 5.4 shows the results of the Hg-intrusion porosimetry of pyrolyzed samples having various amounts of H44-derived filler. The detected macropore sizes exhibit very narrow distributions, and the entire pore sizes fall into the range of 1 to 10  $\mu\text{m}$ . This indicates that a very uniform pore size is produced by freeze casting, similar to other pore sizes found in literature [26]. The increase in H44-derived filler amounts (and simultaneous decrease in water content) leads to lower porosity and smaller pore size. When the filler amounts varied from 10 wt% (further decreases lead to poor monolith structure) to 40 wt% (further increases result in an inhomogeneous suspension), open porosity decreases from 70% to 45%. Additionally, pore diameters shift to a lower average value; around 5 to 1  $\mu\text{m}$ . Similar trends occur with samples pyrolyzed at 700 and 1000 °C, and pore size distribution and porosity of samples pyrolyzed at 1000 °C are shown in Figure 5.4b. Notably, the solid phase includes H44-derived filler and silica nanoparticles; samples having 10, 20, 30, and 40 wt% H44-derived filler content, silica nanoparticles constitute 37, 44, 51 and 58 wt%, respectively. Since porosity is determined by the solid volume, it will decrease with increasing H44-derived filler. Figure 5.4a and Figure 5.4b demonstrate that the pyrolysis temperatures used had no obvious influence on the macroporous structure in terms of pore size and porosity.

### 5.3.3 Specific surface area and hierarchical structure

#### 5.3.3.1 Effects of solid loading and pyrolysis temperature

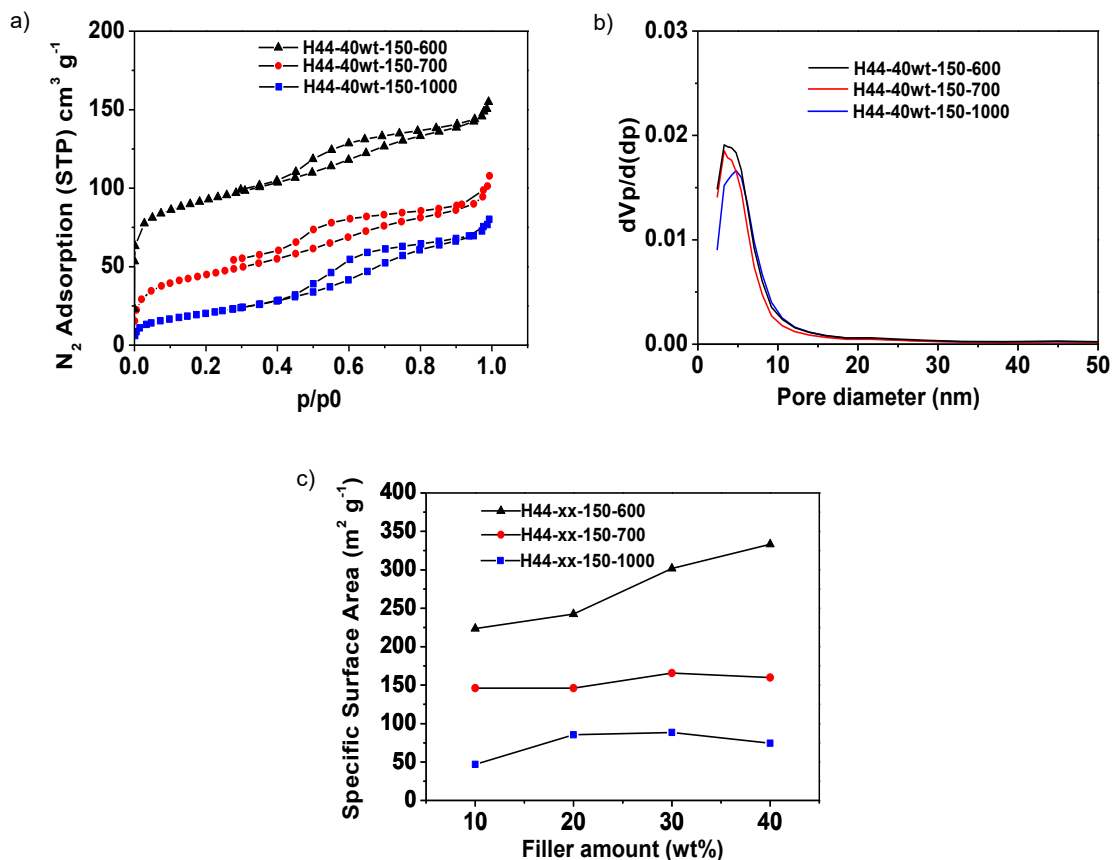


Figure 5.5: a) Nitrogen adsorption-desorption isotherms for samples with 40 wt% H44-derived filler, pyrolyzed at different temperatures. b) BJH analysis of pore size distribution. c) Specific BET surface areas of pyrolyzed (600/700/1000 °C) monoliths as determined by nitrogen adsorption for samples with varied H44-derived filler loadings.

The presence of hysteresis loops in the nitrogen adsorption and desorption isotherms in Figure 5.5a indicates a mesoporous structure in all of the samples even after pyrolysis at 1000 °C. However, the microporous component of the structure is only stable up to 700 °C; pyrolysis at 1000 °C results in an almost complete collapse of the micropores. Macroporosity is normally preserved at higher pyrolysis temperatures [27]. BJH analysis (Figure 5.5b) indicates mesopore diameters between 2 and 12 nm. Interestingly, mesopore size and count seem not to be influenced significantly by pyrolysis temperature, as can be observed by the shape of the hysteresis loop in Figure 5.5a, and the BJH plots in Figure 5.5b.

The influence of H44-derived filler amounts on specific surface area (SSA) was also studied (Figure 5.5c). It can be seen that the SSA could be influenced by changes in the amounts of

added filler, and varied from 46.8 to 350  $\text{m}^2\cdot\text{g}^{-1}$ . At a pyrolysis temperature of 600 °C, with the H44-derived filler amounts increasing from 10 to 40 wt%, the SSA increased from 220 to 350  $\text{m}^2\cdot\text{g}^{-1}$ . Using a pyrolysis temperature of 700 °C, the SSA rose from 146.2 to 159.8  $\text{m}^2\cdot\text{g}^{-1}$  with increasing H44-derived filler amounts. After a pyrolysis at 1000 °C, the SSA still increased, rising from 46.8 to 74.4  $\text{m}^2\cdot\text{g}^{-1}$  with increasing filler amount.

### 5.3.4 Surface characteristics

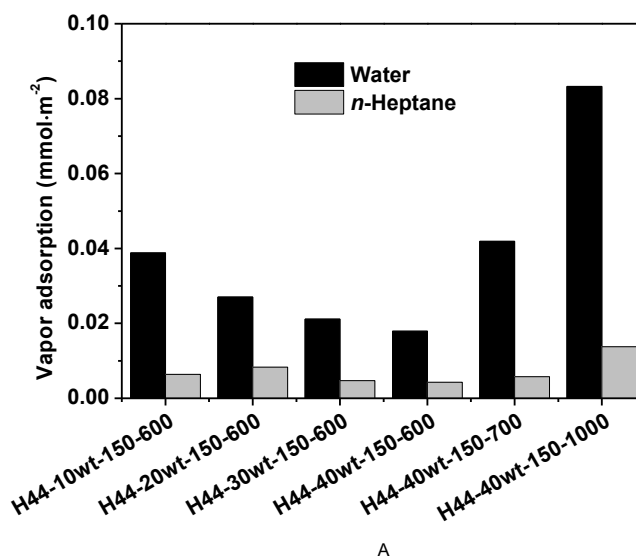


Figure 5.6: Water and *n*-heptane vapor adsorption at 25 °C for samples with different H44 derived filler amounts pyrolyzed at 600 and 700 °C. The sorption data were recalculated using the specific surface area from N<sub>2</sub> adsorption.

Hydrophilicity and hydrophobicity characteristics of the pyrolyzed samples are indicated by water and *n*-heptane vapour adsorption at 22 °C (Figure 5.6). All of the samples obtained display hydrophilic surface characteristics. Depending on the pyrolysis temperature and the H44-derived filler amounts, the hydrophilicity varies. Higher pyrolysis temperatures (1000 °C) lead to the decomposition of methyl groups in the precursor, resulting in improved surface hydrophilicity of the pyrolyzed sample. This is indicated by greater amounts of water vapour adsorbed per SSA, compared to the *n*-heptane adsorption. The water vapour adsorption greatly increased with increasing pyrolysis temperature, from 0.019 to 0.084  $\text{mmol}\cdot\text{m}^{-2}$ , compared to *n*-heptane adsorption: 0.005 to 0.015  $\text{mmol}\cdot\text{m}^{-2}$ . For samples pyrolyzed at 600 °C, when the filler amount increases from 10wt % to 40wt %, the more hydrophilic silica content decreases, resulting in an overall decrease in the water adsorption with increasing filler content.

## 5.4 Discussion

### 5.4.1 Lamellar morphology of SiOC materials

The surface characteristics of polymer precursors can be adjusted by preliminary pyrolysis. Initial work has shown that H44 precursor pyrolyzed at 500 °C still exhibits a very hydrophobic surface based on water and *n*-heptane adsorption results. After pyrolysis at 600 °C, the resultant filler material's surface displays more hydrophilic characteristics (Figure A2 in Appendix A1). This enables the formation of the suspension with water. Pyrolysis at higher temperatures would increase the hydrophilicity slightly, but lead to a higher degree of decomposition of the H44 precursor. This would reduce the carbon content in the final SiOC material and monolith mechanical strength.

Unlike polysiloxane dissolving in an organic solvent, such as camphene, in which the pore structure is created by a thermally-induced phase separation of solvent from solute [28], the pore structure is created by H44-derived filler material pushed aside by ice crystals as they grow. During the freezing process, the particles in the slurry are repelled by the moving ice solidification front, concentrated, and trapped in between the growing ice crystals. The now-agglomerated silica particles will undergo a cross-linking reaction and act as a binder, forming a mechanically strong monolith. It has been reported that at high solid contents, a tubular (or columnar) pore structure is produced during the freeze casting process [12, 29]. The pore morphologies of pyrolyzed monoliths differ when frozen at different temperatures; structures varied from tubular pores to lamellar pores. Macropore structures did not change during pyrolysis.

Water crystallizes in the hexagonal crystal system, with the ice crystals having a growth velocity approximately 100 times faster in the *a*-direction of the hexagonal base than in the perpendicular *c*-direction [30]. As a result, ice crystals develop a lamellar microstructure parallel to the *a*-direction, resulting in a lamellar spacing. Lower freezing temperatures result in higher freezing front velocities. For the samples freezing at -150 °C, the higher freezing velocity leads to smaller ice lamellae. The ice growth along the *c*-axis bridged lamellar pores and resulted in a tubular channel structure. Conversely, wall thickness increased greatly with warmer freezing temperatures, due to lower numbers of ice crystal nucleation and a lower ice front velocity at slower freezing rates [12].

### 5.4.2 Hierarchical structure

The freeze casting method by itself can only produce macroporous structures. However, by combining freeze casting with the pre-ceramic polymer, micropores were introduced via decomposition of the pre-ceramic polymer [22]. Additionally, the packing geometry of the H44-derived filler with silica particles and itself results in the formation of a mesoporous structure [31]; the sizes of the particles directly influence the pore size. The H44-derived filler particles fall into the sub-micron range, which normally should produce pores in the same size range. However,



during the pyrolysis of the green body, the silica particles and H44-derived filler may still react [32]. This allows the particles to bind together, reducing the ‘particle packing’ pore size, and maximizing the mechanical strength of the final monolith. Thus, it is important that the preliminary pyrolysis temperature not exceed 600 °C to get mechanically strong monolith. As shown in Figure 5.5, mesopores appeared to be unaffected by pyrolysis temperatures from 600 to 1000 °C, likely due to the relative stability of the H44-derived filler material at these temperatures (TGA results in Appendix Figure A3). Additionally, silica particles are well embedded in the ceramic matrix, which suppresses silica particle growth (silica particles not embedded in a ceramic matrix are expected to coarsen greatly at the applied temperature of 1000 °C). This phenomenon is often observed for particles embedded in a carbon matrix [33]. The usage of silica sol also plays an important role in the mechanical strength of the monolith.

### 5.4.3 Influences of the process parameters

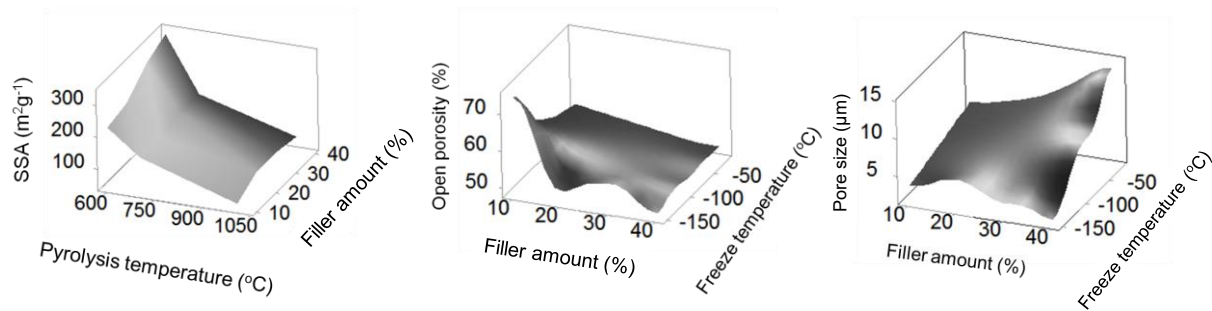


Figure 5.7: a) 3D representation of the influence of filler amount and pyrolysis temperatures on SSA. b) Influence of filler amounts and freezing temperatures on porosity. c) Influence of factors from 5.7b on pore size.

SSA measured by nitrogen adsorption and desorption, open porosity and pore size measured by Hg intrusion were plotted against pyrolysis temperature, H44-derived filler amount, and freezing temperature, respectively. The 3D visualization in Figure 5.7 shows that the pyrolysis temperature has more influence on SSA than amounts of H44-derived filler. The highest SSA is obtained for materials with a filler amount of 40 wt % pyrolyzed at 600 °C. The freezing temperature was found to have very little impact on SSA (not shown). The adjustable SSA is due to the H44-derived filler, which exhibits a SSA of around 500 m<sup>2</sup>·g<sup>-1</sup> for the pristine material pyrolyzed at 600 °C [22, 34]. Due to the relatively high amount of H44-derived filler in the monolith, increasing the filler amount can, to a point, increase the SSA. At pyrolysis temperatures of 1000 °C, micropores are destroyed, and mesopores are still preserved, the less contribution of mesopores to SSA resulting in a reduction of SSA gains with increasing filler percentages.

The main factors influencing the resultant morphology and porosity are the freezing temperature and solid loading; also observed for materials derived from inorganic powders [12]. Increases in solid content of the suspension at the same freezing temperatures result in slightly smaller ice

crystals, due to a lowered water content. Both H44-derived filler amount and freezing temperature influence the open porosity and pore size. For porosity, filler amount plays a major role. However, for the sample H44-10wt-xx-1000, when frozen at -20 °C, a much larger pore size and thicker pore walls resulted. The extremely high water content led to a very fragile monolith structure, which collapsed easily into powder. The pore structure might be partially destroyed during the drying process, leading to the low porosity. In some studies that have used camphene and *tert*-butyl alcohol as the solvent, solid loading influenced pore size dramatically [13]. However, in this study, pore size was not strongly influenced by filler amount, likely due to the rapid crystallization of water compared to other solvents. The highest porosity can be achieved with lowest filler amounts at lowest freezing temperature.

### 5.5 Conclusion

Polymer-derived ceramic monoliths with hierarchically-ordered micro-/meso-/macroporous structures have been fabricated for the first time using a water-based freeze casting method and polysiloxane-based filler as the solid phase. The hierarchically-ordered pore structure, pore size distribution, porosity, SSA, surface characteristics can be adjusted by varying pyrolysis temperatures, solid loadings, and freezing temperatures. The combination of polymer-derived filler materials with freeze casting not only results in lamellar SiOC structures (pore sizes from a few up to ca. 20  $\mu\text{m}$ ), but is also responsible for a relatively high SSA (46.8 to 350  $\text{m}^2\cdot\text{g}^{-1}$ ) in the presence of mesopores (diameters of 2 to 12 nm). Using H44-derived filler material as the solid phase enables the fabrication of bulk monoliths, free of cracks. The hierarchically-ordered structure, in combination with adjustable material properties, like surface characteristics, could be enormously advantageous for applications such as gas separation and liquid filtration.

### Acknowledgments

This work was supported by German Research Foundation (DFG) within the Research Training Group GRK 1860 “Micro-, meso- and macroporous nonmetallic Materials: Fundamentals and Applications” (MIMENIMA).

### References

- [1] U. F. Vogt, L. Györfy, A. Herzog, T. Graule, G. Plesch, Macroporous silicon carbide foams for porous burner applications and catalyst supports, *J. Phys. Chem. Solids* 68 (2007) 1234–1238.
- [2] H. Seitz, W. Rieder, S. Irsen, B. Leukers, C. Tille, Three-dimensional printing of porous ceramic scaffolds for bone tissue engineering, *J. Biomed. Mater. Res. B Appl. Biomater.* 74B (2005) 782–788.
- [3] K. F. Bolton, A. J. Canty, J. A. Deverell, R. M. Guijt, E. F. Hilder et al., Macroporous monolith supports for continuous flow capillary microreactors, *Tetrahedron Lett.* 47 (2006) 9321–9324.

- [4] J. Adler, Ceramic diesel particulate filters, *Int. J. Appl. Ceram. Technol.* 2 (2005) 429–439.
- [5] Z. Taslicukur, C. Balaban, N. Kuskonmaz, Production of ceramic foam filters for molten metal filtration using expanded polystyrene, *J. Eur. Ceram. Soc.* 27(2007) 637–640.
- [6] P. Colombo, C. Vakifahmetoglu, S. Costacurta, Fabrication of ceramic components with hierarchical porosity, *J. Mater. Sci.* 45 (2010) 5425–5455.
- [7] Y. Shin, C. Wang, G. J. Exarhos, Synthesis of SiC ceramics by the carbothermal reduction of mineralized wood with silica, *Adv. Mater.* 17 (2005) 73–77.
- [8] Y. S. Shin, J. Liu, J. H. Chang, Z. M. Nie, G. J. Exarhos, Hierarchically ordered ceramics through surfactant-templated sol–gel mineralization of biological cellular structures, *Adv. Mater.* 13 (2001) 728–732.
- [9] X. J. Mao, S. W. Wang, S. Shimai, Porous ceramics with trimodal pores prepared by foaming and starch consolidation, *Ceram. Int.* 34 (2008) 107–112.
- [10] A. Z. Lichtner, D. Jauffrès, D. Roussel, F. Charlot, C. L. Martin et al., Dispersion, connectivity and tortuosity of hierarchical porosity composite SOFC cathodes prepared by freeze-casting, *J. Eur. Ceram. Soc.* 35 (2015) 585–595.
- [11] A. R. Studart, U. T. Gonzenbach, E. Tervoort, L. J. Gauckler, Processing routes to macroporous ceramics: A review, *J. Am. Ceram. Soc.* 89 (2006) 1771–1789.
- [12] S. Deville, Freeze-casting of porous ceramics: A review of current achievements and issues, *Adv. Eng. Mater.* 10 (2008) 155–169.
- [13] M. Naviroj, S. M. Miller, P. Colombo, K. T. Faber, Directionally aligned macroporous SiOC via freeze casting of preceramic polymers, *J. Eur. Ceram. Soc.* 35 (2015) 2225–2232.
- [14] B. H. Yoon, E. J. Lee, H. E. Kim, Highly aligned porous silicon carbide ceramics by freezing polycarbosilane/camphene solution, *J. Am. Ceram. Soc.* 90 (2007) 1753–1759.
- [15] L. F. Hu, C. A. Wang, Y. Huang, C. C. Sun, S. Lu et al., Control of pore channelsize during freeze casting of porous YSZ ceramics with unidirectionally aligned channels using different freezing temperatures, *J. Eur. Ceram. Soc.* 30 (2010) 3389–3396.
- [16] M. Fukushima, M. Nakata, Y. Zhou, T. Ohji, Y. Yoshizawa, Fabrication and properties of ultra highly porous silicon carbide by the gelation–freezing method, *J. Eur. Ceram. Soc.* 30 (2010) 2889–2896.
- [17] B. H. Yoon, C. S. Park, H. E. Kim, In situ synthesis of porous silicon carbide (SiC) ceramics decorated with SiC nanowires, *J. Am. Ceram. Soc.* 90 (2007) 3759–3766.
- [18] P. Colombo, M. Modesti, Silicon oxycarbide ceramic foams from a preceramic polymer, *J. Am. Ceram. Soc.* 82 (1999) 573–578.
- [19] P. Colombo, G. Mera, R. Riedel, G. D. Sorarù, Polymer-derived ceramics: 40 years of research and innovation in advanced ceramics, *J. Am. Ceram. Soc.* 93 (2010) 1805–1837.
- [20] P. Colombo, Engineering porosity in polymer-derived ceramics, *J. Eur. Ceram. Soc.* 28 (2008) 1389–1395.
- [21] H. Schmidt, D. Koch, G. Grathwohl, P. Colombo, Micro-/macroporous ceramics from preceramic precursors, *J. Am. Ceram. Soc.* 84 (2001) 2252–2255.

- [22] T. Prenzel, M. Wilhelm, K. Rezwan, Pyrolyzed polysiloxane membranes with tailorable hydrophobicity, porosity and high specific surface area, *Micropor. Mesopor. Mater.* 169 (2013) 160–167.
- [23] R. W. O'Brien, B. R. Midmore, A. Lamb, R. J. Hunter, Electroacoustic studies of moderately concentrated colloidal suspensions, *Faraday Discuss. Chem. Soc.* 90 (1990) 301–312.
- [24] D. Hanaor, M. Michelazzi, C. Leonelli, C. C. Sorrell, The effects of carboxylic acids on the aqueous dispersion and electrophoretic deposition of  $ZrO_2$ , *J. Eur. Ceram. Soc.* 32 (2012) 235–244.
- [25] J. W. Moon, H. J. Hwang, M. Awano, K. Maeda, Preparation of NiO–YSZ tubular support with radially aligned pore channels, *Mater. Lett.* 57 (2003) 1428–1434.
- [26] S. Blindow, M. Pulkin, D. Koch, G. Grathwohl, K. Rezwan, Hydroxyapatite/SiO<sub>2</sub> composites via freeze casting for bone tissue engineering, *Adv. Eng. Mater.* 11 (2009) 875–884.
- [27] J. H. Eom, Y. W. Kim, S. Raju, Processing and properties of macroporous silicon carbide ceramics: a review, *J. Asian Ceram. Soc.* 1 (2013) 220–242.
- [28] T. Nishi, T. T. Wang, T. K. Kwei, Thermally induced phase separation behavior of compatible polymer mixture, *Macromolecules* 8 (1975) 227–234.
- [29] B. Wicklein, A. Kocjan, G. Salazar-Alvarez, F. Carosio, G. Camino et al., Thermally insulating and fire-retardant lightweight anisotropic foams based on nanocellulose and grapheme oxide, *Nat. Nanotechnol.* 10 (2015) 277–283.
- [30] U. G. K. Wegst, M. Schecter, A. E. Donius, P. M. Hunger, Biomaterials by freeze casting, *Phil. Trans. R. Soc. A* 368 (2010) 2099–2121.
- [31] J. H. Eom, Y. W. Kim, S. Raju, Processing and properties of macroporous silicon carbide ceramics: a review, *J. Asian Ceram. Soc.* 1 (2013) 220–242.
- [32] P. Greil, Polymer derived engineering ceramics, *Adv. Eng. Mater.* 2 (2000) 339–348.
- [33] R. Dominko, D. E. Conte, D. Hanzel, M. Gaberscek, J. Jamnik, Impact of synthesis conditions on the structure and performance of  $Li_2FeSiO_4$ , *J. Power Sour.* 178 (2008) 842–847.
- [34] M. Adam, M. Wilhelm, G. Grathwohl, Polysiloxane derived hybrid ceramics with nanodispersed Pt, *Micropor. Mesopor. Mater.* 151 (2012) 195–200.

## 6. Adjusting hydrophilicity of polysiloxane by composition for freeze casting

*Adapted from: Water-based freeze casting: Adjusting hydrophobic polymethylsiloxane for obtaining hierarchically ordered porous SiOC*

*Published in: Journal of the American Ceramic Society, 100 (2017) 1907–1918*

*Received 25 July 2016 Accepted 12 January 2017 Available online 7 March 2017*

*Authors: Huixing Zhang, Clara Lana Fidelis, Ana Luiza Teixeira Serva, Michaela Wilhelm\*, Kurosch Rezwan*

*University of Bremen, Advanced Ceramics, Am Biologischen Garten 2, IW3, Germany*

*\* Corresponding author. E-mail address: mwillhelm@uni-bremen.de*

*DOI: 10.1111/jace.14782*

*Reprint (adapted) with permission from John Wiley and Sons, license number: 4151391318381*

### Abstract

The hydrophobic properties of methyl poly siloxane (MK) were pushed into the “hydrophilic” range by cross-linking it with (3-aminopropyl)triethoxysilane (APTES) and subsequent pyrolysis to enable water-based freeze casting. Filler properties are investigated by varying the ratios of MK to APTES (1:1, 2:1, 3:1, 4:1, 5:1), and pyrolysis temperatures (400, 500, 600 °C) for the purpose of determining an optimal set of characteristics for freeze casting. Additionally, filler selection for this purpose is facilitated by analysis of zeta potential values and vapor adsorption. It was found that water-based freeze casting with hybrid fillers, followed by a pyrolysis step (600–700 °C), leads to a SiOC ceramic monolith with a lamellar pore morphology and a hierarchically-ordered micro/meso/macropore structure. Samples pyrolyzed at 1000 °C contain mesopores, having a SSA as high as 51.6 m<sup>2</sup>·g<sup>-1</sup>. The hierarchically porous structure is very promising for applications involving gas or liquid transportation.

### Keywords

Freeze casting, Polymer derived ceramics, Surface characteristics, Micro/meso/macropore, Silicon oxycarbide

### 6.1 Introduction

Applications like catalysis, gas adsorption, water filtration, molten metal filtration, bone tissue engineering, and energy storage/conversion involving the gas or liquid transportation processes normally require that the material has a high permeability to avoid mass transportation problems. These problems can be mitigated by introducing macroporosity into the materials' structure [1–7]. Depending on the specific applications, hierarchical porous structures (meso/micropore) and/or a high specific surface area may be required. There are several techniques for

fabricating macroporous monoliths, such as sacrificial templating, direct foaming, replica method, and additive manufacturing [8–11]; each of these techniques have various benefits and drawbacks. These methods have often been combined with other techniques to produce macroporous monolith of hierarchical structures [12–13].

Freeze casting techniques (a special sacrificial templating method) create porosity by freezing a stable suspension at low temperatures during which the freezing solvent pushes the suspended ceramic particles away from the frozen front [14]. This near-net shape and powerful technique has been widely used to produce bulky macroporous monoliths having different pore shapes by using water, camphene, or *tert*-butyl alcohol or mixtures as the sublimate medium [14–18]. Additionally, additives can influence the final pore morphology of the monolith [19].

Polymer-derived ceramics (normally SiC, SiCN, SiOC, etc.) are prepared by pyrolyzing pre-ceramic polymers at relatively low pyrolysis temperatures: 1000 to 1400 °C [20]. When pre-polymers are pyrolyzed at even lower temperatures (500–700 °C), microporosity, and occasionally mesoporosity, can be obtained [21]. Sacrificial templating, direction foaming, and additive manufacturing methods have been applied to shape porous polymer-derived ceramics (foams, membranes, components with hierarchical porosity). Meso/macroporous SiOC monoliths were obtained by embedding periodic mesoporous organosilica (PMO) particles into foamed siloxane preceramic polymer [22]. Micro/macropore SiOC monoliths have been prepared by adding polymer-derived fillers and controllable pyrolysis by direct foaming and sacrificial templating [23–25].

Inorganic powders, mainly ( $\text{Al}_2\text{O}_3$ ,  $\text{ZrO}_2$ , SiC,  $\text{Si}_3\text{N}_4$  etc.), have been mixed with water, camphene, or *tert*-butyl alcohol to form stable suspensions for freeze casting to produce macroporous monoliths [15, 16, 26–28]. Organic precursors, such as polycarbosilane were mixed with camphene to get a homogenous polymer solution; the pores formed by thermally-induced phase separation (TIPS) during freezing [29]. Poly(methyl-silsesquioxane) has also been used with *tert*-butyl alcohol, camphene, and cyclohexane to get SiOC porous material; precise control of cross-linking is required to prevent early gelation or poor mechanical integrity [30]. Polymer-derived ceramics have the advantages of adjusting pore sizes at different scales and altering surface characteristics via processing parameters, while freeze casting can be used to adjust the pore structure and permeability of the macroporous monolith. The combination of polymethylsiloxane with water-based freeze casting renders open the possibility of producing a hierarchically-ordered porous monolith; however, few studies have been done, due to the strong hydrophobicity of most preceramic polymers.

Methyl phenyl polysiloxane (H44) has been “hydrophilicized” by thermal decomposition in an inert gas atmosphere, and has been successfully applied in water-based freeze casting in our group, resulting in hierarchically-ordered micro/meso/macroporous SiOC monoliths [31]. However, in case of methyl polysiloxane (MK), the hydrophilicization by thermal decomposition will not be practical due to high decomposition temperature of methyl groups, therefore, other

methods are required for modifying surface characteristics (hydrophilicity/hydrophobicity). For example, hydrophilic sodium silicate-based gels have been composited with silylating agents to produce hydrophobic aerogels [32]. The wettability of polydimethylsiloxane has been improved by plasma treatment, producing a thin, brittle, oxidized surface layer [33]. And, a thin film composite (TFC) polyamide (PA) nanofiltration (NF) membrane has been chemically modified by graft polymerization and functional group substitution to increase the negative charge and hydrophilicity of the raw membrane [34]. In this work, we develop a way to modify the surface characteristics of methyl polysiloxane to use it as a filler for water-based freeze casting by cross-linking it with (3-aminopropyl)triethoxysilane (APTES) and subsequent pyrolysis. The optimization of hydrophilicity was achieved by varying the ratios of methyl polysiloxane to APTES and pyrolysis temperatures. The obtained hybrid material was mixed with silica sol (which served as both a binder and water phase) during freeze casting. After pyrolysis, hierarchically-ordered micro/meso/macropore SiOC ceramic monoliths with lamellar macropores were obtained. This work not only renders applying hydrophobic polysiloxane to water-based freeze casting for producing hierarchically-ordered porous monoliths by combining freeze casting with preceramic precursors, but also offers multiple possibilities in terms of surface characteristics, and microstructures on different scales.

### 6.2 Experimental procedure

#### 6.2.1. Materials

A silicone resin poly(methyl-silsesquioxane) was acquired from Silres<sup>®</sup> MK, Wacker Chemie AG, Germany. Silica sol (30 wt% SiO<sub>2</sub> nanoparticles, 8nm, BegoSol<sup>®</sup> K) was acquired from Bremer Goldschlägerei Wilh. Herbst GmbH & Co. KG., Germany. Polyacrylic acid (PAA, Syntran 8140) was purchased from Interpolymer GmbH, Germany. (3-aminopropyl)triethoxysilane (APTES) was purchased from Abcr GmbH, Germany.

#### 6.2.2 Processing

The silica sol acts as a binder and water source during the freezing process. There are some criteria for choosing the precursors applicable for water (silica sol)-based freeze casting. The particles need to be hydrophilic to mix with water, and negatively charged, due to the negatively-charged silica particles, and have a zeta potential (Zeta potential <-30 mV) high enough to form a stable suspension [35]. The hydrophobic MK is altered to hydrophilic material via cross-linking with APTES and a following pyrolysis process. These hydrophilic materials prepared with varied MK: APTES ratios and pyrolysis temperatures were screened for fillers usable for freeze casting.

##### 6.2.2.1 Preparation of fillers

70.3 g (1 mol) of MK was dissolved in 70 ml ethanol. APTES was added into the above solution. The molar ratios of MK: APTES were varied (1:1; 2:1; 3:1; 5:1). Water was used to catalyze the cross-linking, added dropwise to the solution. The mixture obtained was stirred until the

solidification was complete. The amount of water added was calculated based on the active groups of MK and APTES [36]. The solid was then transferred to the cross-linking oven using a multi-stage heat treatment in air at 80 °C, 140 °C, and 200 °C (all dwell times 2 h), with a heating rate of 60 °C·h<sup>-1</sup> in between dwell times. The pre-cross-linked polysiloxane pieces were then pyrolyzed at various temperatures (400, 500 or 600 °C) under a nitrogen atmosphere. The heating rate was set to 120 °C·h<sup>-1</sup> up to 100 °C below the target temperature and then 30 °C·h<sup>-1</sup> to the final temperature, with a dwell time of 4 hours. The powders were then transferred to a planetary ball milling machine (PM 400, Retsch) and ground at 350 r·min<sup>-1</sup> for 6h to produce fine powders. These hybrid fillers are used for the following freeze casting process.

### 6.2.2.2 Preparation of porous monolith

30 wt% precursor powders were added to 70 wt% silica sol under stirring. The pH was adjusted to 6–7 using PAA to ensure the complete condensation reaction of silica sol. Compared to water, the negatively charged MK-APTES-derived fillers had higher stability in anionic colloidal silica, due to stronger interparticle repulsion. The pH value of the slurry also influences the zeta potential of particles, and thus the suspension stability. A slurry pH value of 6 to 7 was experimentally determined to produce the mechanically strongest monoliths after freezing. The cross-linking (condensation) rate between silica particles is greatly influenced by the pH of the slurry; this effect allows silica to act as a binder during the preparation process. A pH value below 6 led to suspensions having very low stability, while pH values of 8 to 11 lead to insufficient condensation. The obtained slurry was then placed under vacuum at 300 mbar for 5 min to remove bubbles created during stirring. Then it was poured into a 120 mm (adjustable to account for slurry amount) ×70 mm ×25 mm mold, made of 2 aluminium plates (high heat conduction), and a polyvinyl chloride (PVC) U-shaped plate (relatively insulating). Then the mold was quickly transferred to a freezer (-150 °C) for 2 h to produce a completely frozen body. The samples were then transferred to a freeze dryer for 5 d at -30 °C for sublimation. Finally, the samples were pyrolyzed at different pyrolysis temperatures (600, 700, 1000 °C) under a nitrogen atmosphere. A scheme of the preparation process is shown in Figure 6.1. The fillers followed the nomenclature “xMK-yAPTES-xxx” and the post-pyrolysis freeze cast samples followed the nomenclature “xMK-yAPTES-xxx-yyy”; the molar ratio of MK: APTES is x/y, the first value xxx is the pyrolysis temperature of the filler material (200 °C means the samples were only cross-linked with the heating program: 80, 140, and 200 °C), and the second value yyy describes the pyrolysis temperature of the monolith.



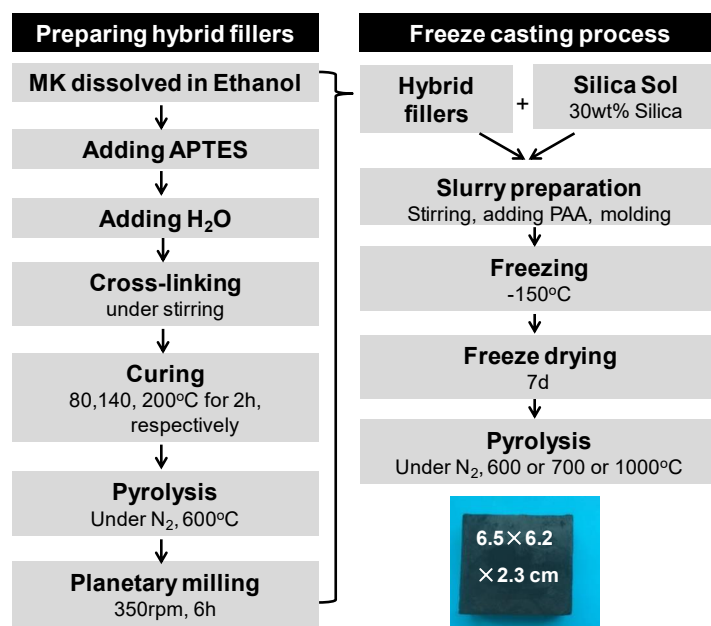


Figure 6.1: Process scheme, parameter variations of synthesized samples, and sample monolith pyrolyzed at 1000 °C.

### 6.2.3. Characterizations

Thermogravimetric analysis (TGA, STA503, Bähr, Germany) was performed at a temperature range of 20 – 1000 °C under flowing nitrogen ( $2 \text{ L} \cdot \text{h}^{-1}$ ) with a heating rate of  $10 \text{ }^\circ\text{C} \cdot \text{min}^{-1}$ . Zeta potentials of the hybrid fillers were measured (Dispersion Technology Zeta & Size 1200, Dispersion Technology Inc, US) to evaluate the surface charges of particles and the stability of the suspension. Specific surface areas and pore size distributions were determined by nitrogen adsorption and desorption isotherms (Belsorp-Mini, Bel Japan, Inc., Japan). The monolith materials were ground and sieved with a  $300 \mu\text{m}$  mesh sieve in order to minimize nitrogen diffusion effects during the measurements, and were degassed at  $120 \text{ }^\circ\text{C}$  for 3 h before the analysis. Water vapour and *n*-heptane adsorption measurements were carried out by placing vessels with  $\sim 0.5 \text{ g}$  of sample powder (particle sizes  $\leq 300 \mu\text{m}$ ) inside of closed Erlenmeyer flasks filled with the solvents at equilibrium with their vapour phase at room temperature. Samples were weighed at the start and end of a 24 h measurement period in order to determine the vapour uptake of the material. The uptake was then recalculated into  $\text{g} \cdot \text{m}^{-2}$  using the specific surface area of the materials (measured by nitrogen adsorption). The particle size and pore morphology of samples was analyzed via scanning electron microscopy (SEM, Camscan Series 2, Obducat CamScan Ltd., Germany). Samples were sputtered with gold (K550, Emitech, Judges Scientific plc., UK) before measurements. Mercury intrusion porosimetry (Pascal 140/440, POROTEC GmbH, Germany) was used to determine the macroporosities.

## 6.3 Results

### 6.3.1 Fillers

#### 6.3.1.1 Thermal decomposition of fillers

The cross-linked APTES, MK, and cross-linked xMK-yAPTES-xxx samples were investigated by TGA, as shown in Figure 6.2, to determine the pyrolysis temperature to produce the fillers. The cross-linked MK shows less than 3% decomposition before 700 °C, due to the high thermal stability of methyl groups in the resin [36]. Decomposition of amino groups in the cross-linked APTES begins around 400 °C; the majority of the decomposition happens before 600 °C.

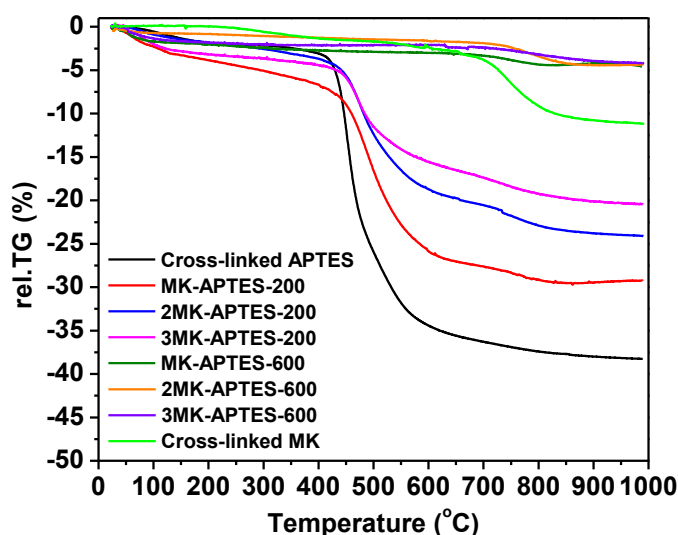


Figure 6.2: TGA of cross-linked xMK-yAPTES-xxx and cross-linked APTES and cross-linked MK.

Mass loss of cross-linked xMK-yAPTES-200 shows thermal decomposition behaviours similar to 'pure' APTES. The decomposition starts at 400 °C, and proceeds to 900 °C. Pyrolysis temperatures of 400, 500 and 600 °C were chosen for pyrolyzing xMK-yAPTES-200, after the observation that 600 °C was high enough to decompose the  $-NH_2$  group while preserving a certain number of  $-CH_3$  groups, which can help to bonds formation between the pre-pyrolyzed granulates. The thermal decomposition of resultant hybrid filler xMK-yAPTES-600 was also investigated. It was shown that the decomposition of xMK-yAPTES-600 was negligible even up to 1000 °C, which highly reduces the gas produced during pyrolysis.

#### 6.3.1.2 Specific surface areas of fillers

The specific surface areas (SSA) of the hybrid fillers were investigated in order to determine the influence of their SSA on the final monoliths. The specific surface areas (SSA) of the hybrid fillers in Table 6.1 show that both the pyrolysis temperature and MK: APTES molar ratios have

an influence on the SSA. The SSA of the fillers ranged from 164 to 321  $\text{m}^2\cdot\text{g}^{-1}$ . This high specific surface area is due to micropores produced during pyrolysis, which can be inferred from the nitrogen adsorption isotherms. For the pure (unmixed) precursors, a SSA of 350  $\text{m}^2\cdot\text{g}^{-1}$  was observed for APTES, while MK showed a SSA of 280  $\text{m}^2\cdot\text{g}^{-1}$  after cross-linking and pyrolysis at 600 °C [37–38]. However, the SSAs of xMK-yAPTES-600 filler prepared with different MK: APTES ratios (from 5:1 to 1:1) decreased with the increasing APTES content. Interestingly, SSA at the ratio 1:2 is 281  $\text{m}^2\cdot\text{g}^{-1}$ , which is also the highest value. That means a linear relation between the SSAs and the MK/APTES ratio was not observed. A possible explanation is that the SSA are not only influenced by the MK/APTES ratio, but also by the cross-linking behavior, which was also influenced by other factors, the stirring rate or the ambient temperature, or even different batches of MK from the same supplier, etc. Both APTES and MK needed to be hydrolyzed to cross-link. 1 mol MK has only 4% of active groups that can be cross-linked, while 1 mol of APTES can be easily hydrolyzed and has 3 mol hydroxyl groups after hydrolysis that can cross-link fully. The cross-linking between hydrolyzed APTES molecules is much faster than with hydrolyzed MK, which can be influenced by the stirring rate or the ambient temperature, etc. accordingly resulting in different networks and SSA. Pyrolysis of different cross-linked products at different temperatures resulted in different SSA. The SSAs of single material cross-linked APTES and MK at pyrolysis temperature of 500 °C are 440  $\text{m}^2\cdot\text{g}^{-1}$  and smaller than 25  $\text{m}^2\cdot\text{g}^{-1}$ , respectively [37–38]. Higher SSAs were achieved at 500 °C for APTES and at 600 °C for MK, which explains the relation of SSA with pyrolysis temperature. The SSA of 1MK-1APTES-xxx at 400, 500, 600 °C are 124, 321 and 164  $\text{m}^2\cdot\text{g}^{-1}$ , respectively. At 500 °C, the molar ratio MK: APTES = 1 produced the highest SSA among all the fillers.

Table 6.1: Prepared material, MK: APTES molar compositions, pyrolysis parameters and resultant specific surface area.

Sample	MK: APTES molar ratio	Pyrolysis temperature [°C]	Specific surface area [ $\text{m}^2\cdot\text{g}^{-1}$ ]
5MK-1APTES-600	5:1	600	283
3MK-1APTES-600	3:1	600	227
2MK-1APTES-600	2:1	600	224
1MK-1APTES-600	1:1	600	164
1MK-1APTES-500	1:1	500	321
1MK-1APTES-400	1:1	400	124
1MK-2APTES-600	1:2	600	281

### 6.3.1.3 Surface characteristics of fillers

The applicability of preceramic polymers for water-based freeze casting will be greatly influenced by hydrophobicity. Thus, the influence of the pyrolysis temperature and the MK: APTES molar ratios on the surface characteristics were investigated. Hydrophilicity and hydrophobicity of the pyrolyzed samples are determined using water and *n*-heptane vapour

adsorption at 22 °C (Figure 6.3). The vapour adsorption ( $\text{mmol}\cdot\text{m}^{-2}$ ), recalculated based on the SSA values, were influenced by the specific surface area. However, the hydrophilicity was reflected by the ratio of water/heptane adsorption, instead of the absolute value of the water or vapour adsorption. All of the samples except 1MK-APTES-400 have a much higher water vapour adsorption than *n*-heptane adsorption, displaying hydrophilic surface characteristics, which might be applicable for freeze casting. However, only 1MK-1APTES-600 in Figure 6.3a shows anomalously high hydrophilicity. The pyrolysis temperature was fixed to 600 °C, at which most of the  $-\text{NH}_2$  groups are decomposed.

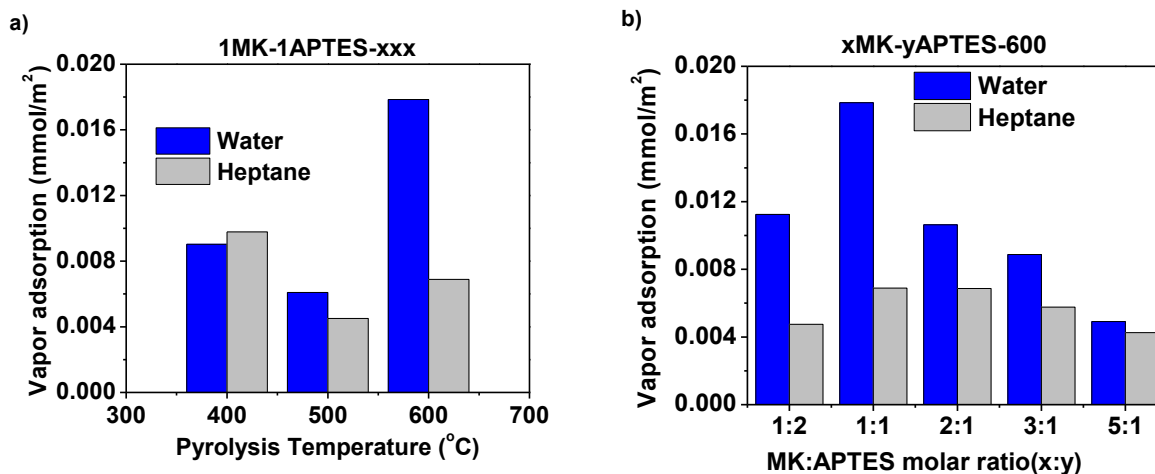


Figure 6.3: Water and *n*-heptane vapor adsorption at 22 °C for precursors pyrolyzed a) at varied temperature and b) with varied MK to APTES amount pyrolyzed at 600 °C. The sorption data were recalculated using the specific BET surface area from N<sub>2</sub> adsorption.

Hydrophilicity varies with the molar ratio of MK: APTES. The highest hydrophilicity was obtained with the sample 1MK-1APTES-600. Higher MK content normally produces fillers having more hydrophobic groups, resulting in a less hydrophilic material. Higher APTES content results in higher hydrophilicity, due to the hydrophilic SiO<sub>2</sub> formed by decomposition of APTES. 1MK-2APTES-600 (MK: APTES=2) shows lower adsorption than 1MK-1APTES-600 (MK: APTES=1). This can be explained by the difference of SSAs. 1MK-1APTES-600 has a SSA of 164 m<sup>2</sup>·g<sup>-1</sup> and 1MK-2APTES-600 has a SSA of 281 m<sup>2</sup>·g<sup>-1</sup>. Therefore, the vapor adsorption of 1MK-1APTES-600 is higher than 1MK-2APTES-600. The ratios of water/heptane adsorption are 1.2, 1.5, 1.6, 2.5 and 2.4, respectively when the MK:APTES ratios were changing from 5:1, 3:1, 2:1, 1:1, 1:2. This showed the increase of the hydrophilicity with increasing APTES contents (The ratios of water/heptane 1MK-1APTES-600 and 1MK-2APTES-600 are 2.5 and 2.4, respectively, which means that the hydrophilicity is very similar). The surface characteristics of the fillers produce predictable surface characteristics in the final porous monolith.

The zeta potentials of the xMK-yAPTES-xxx fillers were measured by dispersing the precursor particles into water to form a suspension. Normally an absolute value of zeta potential greater

than 30 mV is considered to be stable suspension [35]. As seen from Figure 6.4, the particles are mostly negatively charged. At the pH value higher than 6, it was observed that, the absolute values of zeta potential of 1MK-1APTES-600, is higher than 30 mV, which can form stable suspension. During freeze casting, the pH is adjusted to 6–7 to improve the condensation of silica sol.

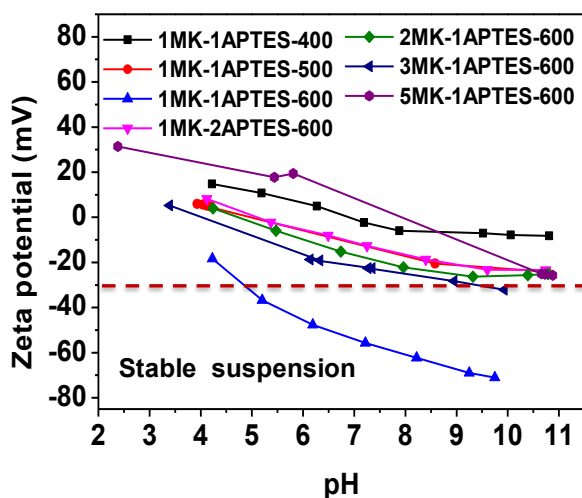


Figure 6.4: Zeta potential of the hybrid fillers with different compositions at various temperatures in de-ionized water.

Due to inadequate hydrophilicity, the other fillers can only be partially wetted by water, forming an unstable suspension, which would not be useful in water-based freeze casting.

At almost the whole pH range, 1MK-1APTES-400 fillers are positively charged, still having considerable numbers of surficial  $-NH_2$  groups due to incomplete thermal decomposition. Fillers with more organic groups (higher MK: APTES ratios) also produced unstable suspensions. Except for forming a stable suspension, the filler should have as much as possible organic groups to form more bonds during pyrolysis. After accounting for surface charge, hydrophilicity, of fillers and mechanical strength of final monolith, 1MK-1APTES-600 was determined to be the optimal precursor for freeze casting.

### 6.3.2 Monoliths prepared by freeze casting

SEM images of pyrolyzed monoliths and fillers are shown in Figure 6.5a. Figure 6.5 (a–b) are two cross sections perpendicular to each other, showing the most unidirectional pore structure. The ice front propagation will follow the temperature gradient, which was controlled by the configuration of the mold in this work. The ice will grow simultaneously from both metal plates to the center and joined in the middle of the sample, which structure was seen with double-size freezing as well [39]. Figure 6.5a shows that the pores are composed of parallel lamellae up to several mm long. Figure 6.5b shows typical pore sizes in the range of 20 – 50  $\mu m$ . Shrinkage in

pore direction after the second pyrolysis is calculated to be around 8%, and the direction perpendicular to it is less than 7%. Since the macropores were created before the final pyrolysis at 1000 °C, gases, by-products of the MK decomposition, can escape easily from the porous structure. Moreover, the macropores acted as a buffer for the thermal shrinkage, which assisted in the production of crack free monoliths.

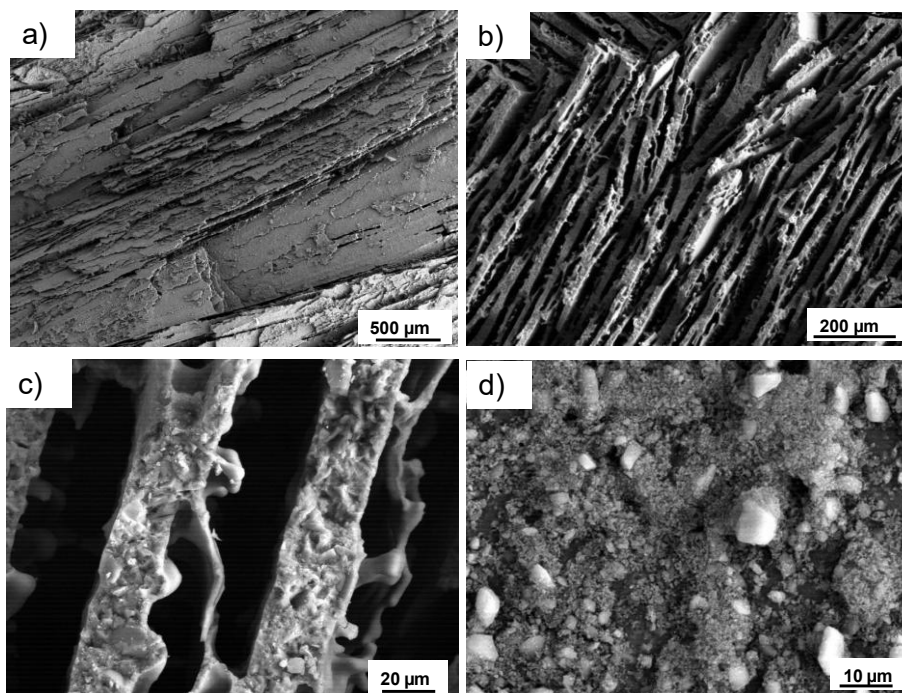


Figure 6.5: SEM images of pyrolyzed monoliths. a) Cross-section parallel to the lamellar pores, b–c) cross sections perpendicular to the lamellar pores, d) SEM image of hybrid filler after planetary milling at 350r/min for 6 hours.

Figure 6.5c shows the hierarchically-ordered pore structure of the monoliths, and how the packing of the particles results in a secondary pore size distribution. It has been reported that the sintering necks of SiOC had formed at pyrolysis temperatures around 1400 °C [40]. Due to lower pyrolysis temperatures and the low organic content of the fillers, pre-pyrolyzed granulates are not completely jointed together. The same hierarchical structure has also been observed for freeze-cast monoliths using methyl-phenyl polysiloxane [31]. Figure 6.5d shows that the particles were mostly below 1 μm, and aggregated, however, unable to be sieved due to the high surface charges and surface area. Therefore, the particle size distribution may be inhomogeneous due to limitations of the planetary ball milling process.

The Hg intrusion porosimetry of the monolith 1MK-APTES-600-1000 shown in Figure 6.6 indicates an open porosity around 55%, a pore size range around 20–50 μm, in agreement with the pores' sizes observed with SEM. A secondary pore size distribution was also observed in the Hg intrusion porosimetry; however, it was of very low relative volume. Thus, nitrogen adsorption and desorption were needed for further information about secondary porosity.

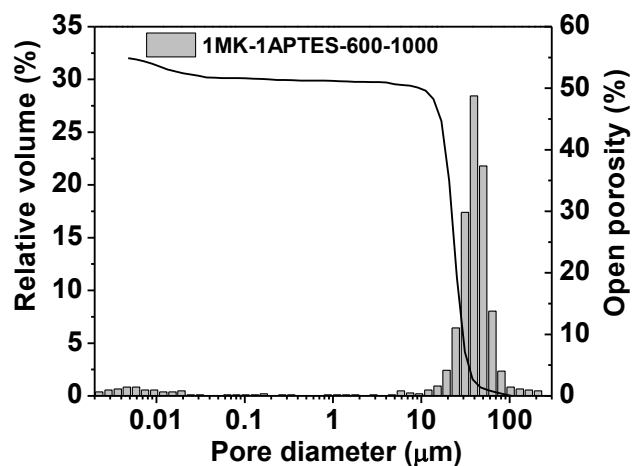


Figure 6.6: Pore size distribution versus relative pore volume and open porosity curves obtained from Hg-porosimetry of pyrolyzed samples.

The nitrogen adsorption and desorption isotherms for samples pyrolyzed at various temperatures are shown in Figure 6.7. Filler MK-APTES-600 has IUPAC type I isotherms, indicating large numbers of micropores (Fig. 6.7a). Monoliths prepared with this filler contain micropores and mesopores after a second pyrolysis at 600 or 700 °C. At pyrolysis temperatures around 1000 °C, the micropores structures collapsed; however, mesoporosity is still observed - inferred from the type IV isotherms of MK-APTES-600-1000, with a SSA as high as  $51.6 \text{ m}^2 \cdot \text{g}^{-1}$ .

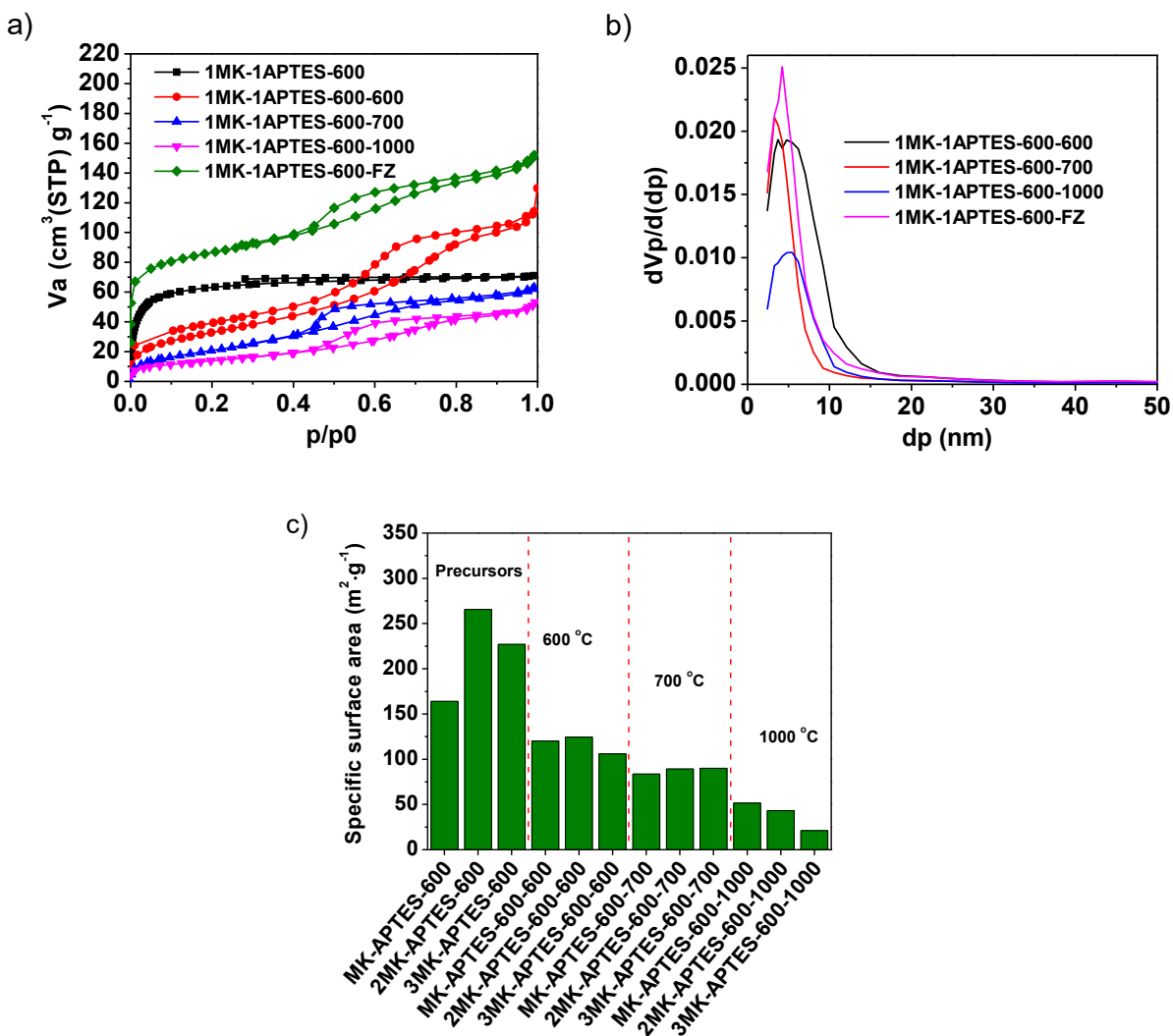


Figure 6.7: a) The nitrogen adsorption and desorption isotherms, b) the BJH analysis of samples pyrolyzed at various temperatures or only freeze-cast, c) SSAs of all precursors and samples pyrolyzed at various temperatures.

The mesoporosity was further analyzed using the BJH model; as shown in Figure 6.7b, the mesopore diameter is around 4–10 nm. Pyrolysis temperatures between 600 and 700 °C result in similar mesopore distributions, indicating few mesopores collapse; however, pyrolysis at 1000 °C resulted in a reduction in the number of mesopores. The specific surface area of samples prepared with xMK-yAPTES-600 and pyrolyzed at various temperatures were investigated (Figure 6.7c) and the influence of MK: APTES ratio on SSA was much less comparing to the pyrolysis temperature.

Compared to the 1MK-APTES-600 filler, water adsorption of the pyrolyzed monoliths was greatly improved, indicating increased hydrophilicity, shown in Figure 6.8. This improvement is likely due to the significant incorporation of hydrophilic silica (by silica sol) and further



decomposition of the organic groups during the second pyrolysis. The higher pyrolysis temperatures lead to higher hydrophilicity, due to the higher degree of decomposition of the fillers.

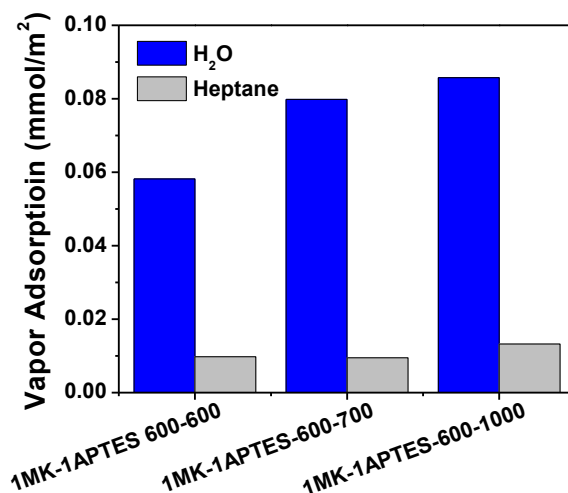


Figure 6.8: Water and *n*-heptane vapor adsorption at 25 °C for monoliths pyrolyzed at various temperatures, compared with those for 1MK-1APTES-600 fillers. The sorption data were recalculated using the specific BET surface area from N<sub>2</sub> adsorption.

## 6.4 Discussion

### 6.4.1 Modification of surface characteristics of fillers

In this work, silica sol went through freeze gelation by condensation during the freezing process. The reason of using silica sol as water source is to improve the mechanical properties of the green body as well as the pyrolyzed monolith, for example, combination of freeze casting Al<sub>2</sub>O<sub>3</sub> with freeze gelation of the acrylamide has been used to improve the mechanical properties [16]. Due to the negative charge of the silica particles, only other negative and hydrophilic particles should be additionally used in the freezing process.

Thermal decomposition of the phenyl groups in methyl-phenyl polysiloxane produced an easily-wetted hydrophilic, at the same time, negatively charged surface. Thermal decomposition is an easy way to alter the surface characteristics of methyl phenyl polysiloxane; however, it does not work for the methyl polysiloxane (MK). The release of methane take place at pyrolysis temperatures around 700–800 °C [36]; a hydrophobic surface is still preserved at a pyrolysis temperature of 600 °C. Thus, other methods are required to alter the surface characteristics of the methyl polysiloxane, eg. compositing or cross-linking with hydrophilic components.

Compositing polysiloxane with SiO<sub>2</sub> particles (1 μm) was investigated (results not presented here), however, inadequate hydrophilicity was observed, limiting its application in our water-based freeze casting. Cross-linking MK with tetraethyl orthosilicate (TEOS, molar ratios MK:

## 6. Adjusting hydrophilicity of polysiloxane by composition for freeze casting

TEOS=1:1) also produces a hydrophobic surface after pyrolysis (Figure A4 in Appendix A2), thus cannot be used in water-based freeze casting. There has been significant work done using 3-(triethoxysilyl)propylsuccinic anhydride (TESPSA) to alter the surface of the silica [41], which results in materials with carboxyl groups. Thus, it is possible that fillers prepared with MK cross-linked with TESPSA (negatively charged in the basic pH range) could coexist with silica sol, at a pH around 10. Therefore, cross-linking of MK with TESPSA was also carried out; however, the resultant material is a solid elastomer, very elastic, and unable to be ball milled to produce powders. This might be due to the structure of the TESPSA, which might have steric hindrance during cross-linking, resulting in less bonds formation. For example, one evidence of the steric hindrance was found to be between the anhydride groups and approaching TESPSA species during immobilizing TESPSA on the surface of nanoparticles [42].

As shown in Figure 6.9, the surface modification of MK from hydrophobic to hydrophilic was achieved by compositing it with APTES, however, at pH range 6–7, amino groups on the surface of the cross-linking product should attract protons. This results in a positive charge on cross-linking product particles, making it incompatible with negative silica particles, thus resulting in an unstable suspension. Therefore, a following pyrolysis step is necessary to decompose the amino group in the cross-linked materials to get negatively charged and water-insoluble fillers. As seen from the TGA in Figure 6.2, APTES in 1MK-1APTES-200 underwent significant decomposition at 600 °C, producing hydrophilic SiO<sub>2</sub> nano-domains and the resultant MK-APTES-600 displayed considerable hydrophilicity. Another advantage of cross-linking MK with APTES is that APTES has a potential use for helping with dispersion of metal ions to produce catalytic centers in the matrix [25].

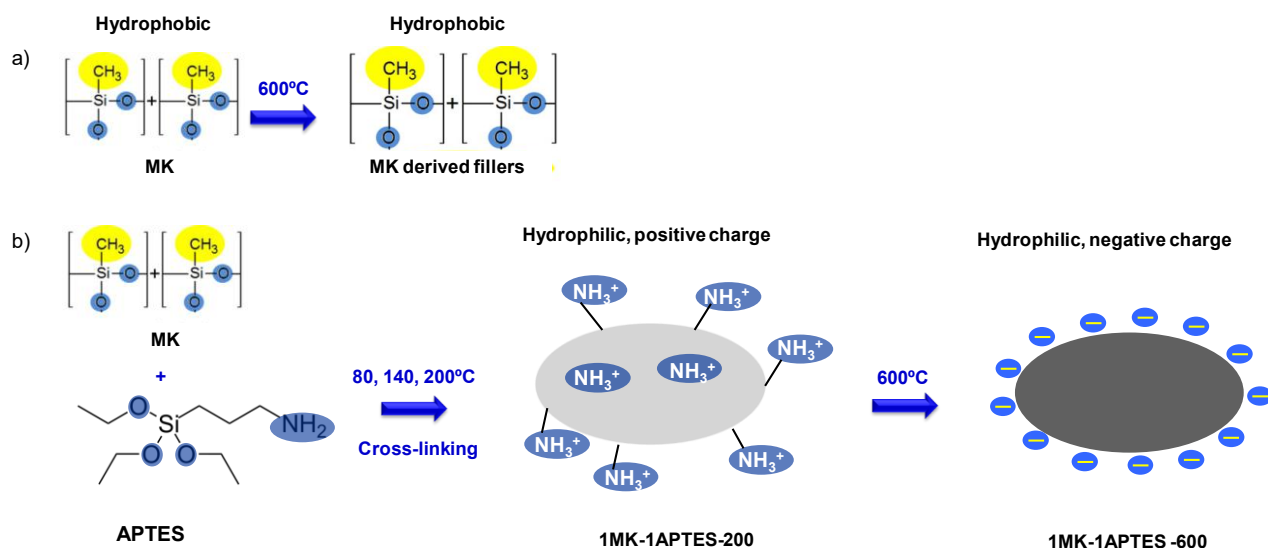


Figure 6.9: Change of chemical structure during pyrolytic conversion. Coloring of functional groups according to [43]: yellow color and blue color represent hydrophobic interactions and hydrophilic interactions, respectively. Decomposition products are not completely released, but

hydrocarbons remain partly in the matrix. a) Surface modification by thermal decomposition and b) Surface modification by compositing and thermal decomposition.

### 6.4.2 The hierarchical porous structure

The pore structure of freeze cast samples are characterized by nitrogen adsorption and Hg intrusion porosimetry, and micro-, meso- as well as macropores were observed. The macropores are created during the freeze casting process, and the mesopores are produced were formed after freeze casting and the following pyrolysis. Introducing solid filler particles into the matrix should hinder the elimination of porosity and shrinkage during pyrolysis, due to its negligible volume change [44]. As shown in Figure 6.7a, nitrogen adsorption and desorption confirmed that 1MK-1APTES-600 fillers had only micropores while 1MK-1APTES-600-FZ (only freeze cast, without pyrolysis) had micropores as well as mesopores, and the mesopores survived the following pyrolysis. During the freeze casting, the packed granulates were consist of silica nanoparticles (8 nm, silica sol) and sub-micrometer hybrid filler (xMK-yAPTES-600 filler). The pressure generated by repulsion from ice and silica condensation between the particles formed the mesopores. There has been some work using binders with nanoparticles to get mesoporous or close to mesopore range materials. Brandes et al [45] have used 200 nm alumina and alginate as binder to get mono-sized 71 nm pores after sintering and Besser [46] and Bartels et al [47] have used 30 nm and 90 nm yttria-stabilized zirconia with PVA as binder to produce 30 nm mesopores and 5–200 nm meso/macropores, respectively. This process is very similar to our silica condensation to get mesopores. The mesopores were highly influenced by the initial particle size. The filler sizes are mostly smaller than 1  $\mu\text{m}$ , and have a relatively broad particle size distribution. This broad particle size distribution and the silica nanoparticles (8 nm) made the packing much denser, resulted in mesopores. During the pyrolysis, the bonds formation of fillers and the sintering of silica particles did not affect the mesopore size obviously as shown in Figure 6.7b.

During thermal decomposition, sintering necks between nanosilica (melting temperature 1600 °C) were formed due to diffusion, and bonds were also formed between hybrid fillers. This allows the particles to ind together, reducing the 'particle packing' pore size, and maximizing the mechanical strength of the final monolith. At the same time, the filler decomposed further, forming more bonds. Since filler has been prepyrolyzed, the reaction during the second pyrolysis was very limited; therefore, mesopores can be preserved. In case of higher pyrolysis (1000 °C or even higher) temperature, mesopores collapsed as shown in Figure 6.7b. The development of micropores is ascribed to the thermal decomposition of the cross-linked polymer. The hierarchical porous structure was produced by combining the preceramic polymer with the water-based freeze casting. Similar micro/meso/macrostructures can be formed when 1MK-APTES-200 particles are suspended in pure water (as they were positively charged, they were not compatible with silica sol) for freeze casting and finally pyrolyzed at 600 °C (Figure A5–A7 in Appendix A2). The use of 1MK-APTES-200 with water led to the similar porous structure, which may simplify the preparation by excluding the pyrolysis steps, however, during the slurry

preparation, the surface of 1MK-1APTES-200 particles are only mostly wetted (not completely wetted, since there will be dry powders floating on the slurry surface), even after a very long stirring times and high speed, which gives relatively inhomogeneous slurry. Besides, the wetted particles were found to be partially dissolvable in water, due to the complexity of this system, it was not investigated further.

### 6.4.3 Influences of silica sol

When silica sol was used during the freeze casting process with filler, the suspension stability of the slurry can be improved. Due to the more negative zeta potential value of silica nanoparticles, the repulsion between the negative particles are stronger, therefore the filler in silica sol were more stable than in water.

The use of silica sol affects the monoliths in terms of surface characteristics (vapor adsorption), and SSA (nitrogen adsorption/desorption) and mesopores. Due to the high hydrophilicity of the silica particles in the sol, the resulting monolith is more hydrophilic. Since silica sol acts as binder, the condensation of silica particles will influence the packing of the filler particles by the binding force, therefore influenced mesopores. The amounts of mesopores and the pore size accordingly influenced SSAs. The use of silica sol was expected to have no obvious influence on micropores and macropores size, however, the silica particles contributed to the solid content, which decreased the macroporosity.

### 6.4.4 Influences of process parameters

The microstructure (pore size, pore morphology, porosity, unidirectional or radial pore structure, etc.) of a monolith can be varied by the altering the freeze casting conditions (freezing rate, temperature gradient directions, solid loading) [10]. The filler powders were produced by planetary ball milling; there is the possibility that some particles may not be ground down smaller than 1  $\mu\text{m}$ . Due to the high specific surface area and surface charges on the surface, particle sizes separation by sieving is unsuccessful. However, even the bigger particle sizes are much smaller than the pore sizes, given that they are small in quantity, they could hardly disturb the ice growth. The freezing process was done in a deep freeze, and the temperature gradient and lamellae growth direction are controlled by the mold configuration; thermal isolation (PVC) versus conducting aluminum. Thus, the temperature gradient may not be perfectly linear along the freeze direction. If a copper cold finger with an accurately controllable temperature gradient is used, a highly unidirectional structure can be obtained [48]. In this work, the ice tends to grow along the temperature gradient, but heterogeneous nucleation results in the formation of randomly oriented lamellar domains perpendicular to the ice front propagation. There has been at least one report using the unidirectional pattern on the cooling surface to manipulate the ice lamellae direction and obtain long-range ordering with well-oriented structures on the length scale of the sample [19].

## 6.5 Conclusion

Altering surface characteristics by compositing hydrophobic methyl polysiloxane with hydrophilic agent and a pyrolysis step turned out to be a strategy, which not only enlarges methods for preparing PDCs using various kinds of polysiloxanes, but also may extend the usage of polysiloxanes in aqueous system. The hydrophobic MK was successfully altered to hydrophilic fillers by introducing APTES and a pyrolysis to apply in water-based freeze casting. The hierarchically-ordered micro/meso/macroporous SiOC macroporous monoliths were created due to thermal decomposition of precursors and freeze casting process. This method enables the adjustment of porosity at different scales, alteration of surface characteristics, and maximization of specific surface areas of final monoliths by varying precursor ratios and pyrolysis temperatures. The incorporation of APTES also raises the possibility to introduce metal salts into the structure; especially useful for catalysis applications.

## Acknowledgments

This work was supported by German Research Foundation (DFG) within the Research Training Group GRK 1860 “Micro-, meso- and macroporous nonmetallic Materials: Fundamentals and Applications” (MIMENIMA).

## References

- [1] J. Zhang, Y. Jin, C. Y. Li, Y. N. Shen, L. Han et al., Creation of three-dimensionally ordered macroporous Au/CeO<sub>2</sub> catalysts with controlled pore sizes and their enhanced catalytic performance for formaldehyde oxidation, *Appl. Catal. B* 91 (2009) 11–20.
- [2] R. P. Ribeiro, T. P. Sauer, F. V. Lopes, R. F. Moreira, C. A. Grande et al., Adsorption of CO<sub>2</sub>, CH<sub>4</sub>, and N<sub>2</sub> in activated carbon honeycomb monolith, *J. Chem. Eng. Data* 53 (2008) 2311–2317.
- [3] G. R. Aiken, D. M. Mcknight, K. A. Thorn, E. M. Thurman, Isolation of hydrophilic organic acids from water using nonionic macroporous resins, *Org. Geochem.* 18 (1992) 567–573.
- [4] Z. Taslicukur, C. Balaban, N. Kuskonmaz, Production of ceramic foam filters for molten metal filtration using expanded polystyrene, *J. Eur. Ceram. Soc.* 27 (2007) 637–640.
- [5] J. Wei, J. F. Jia, F. Wu, S. C. Wei, H. J. Zhou et al., Hierarchically microporous/macroporous scaffold of magnesium–calcium phosphate for bone tissue regeneration, *Biomaterials* 31 (2010) 1260–1269.
- [6] Y. Chen, J. Bunch, T. S. Li, Z. P. Mao, F. L. Chen, Novel functionally graded acicular electrode for solid oxide cells fabricated by the freeze-tape-casting process, *J. Power Sources* 213 (2012) 93–99.
- [7] L. Estevez, R. Dua, N. Bhandari, A. Ramanujapuram, P. Wang et al., A facile approach for the synthesis of monolithic hierarchical porous carbons – high performance materials for amine based CO<sub>2</sub> capture and supercapacitor electrode, *Energy Environ. Sci.* 6 (2013) 1785–1790.

- [8] Y. W. Kim, Y. J. Jin, Y. S. Chun, I. H. Song, H. D. Kim, A simple pressing route to closed-cell microcellular ceramics, *Scripta Mater.* 53 (2005) 921–925.
- [9] U. T. Gonzenbach, A. R. Studart, E. Tervoort, L. J. Gauckler, Macroporous ceramics from particle-stabilized wet foams, *J. Am. Ceram. Soc.* 90 (2007) 16–22.
- [10] A. R. Studart, U. T. Gonzenbach, E. Tervoort, L. J. Gauckler, Processing routes to macroporous ceramics: A review, *J. Am. Ceram. Soc.* 89 (2006) 1771–1789.
- [11] U. G. K. Wegst, H. Bai, E. Saiz, A. P. Tomsia, R. O. Ritchie, Bioinspired structural materials, *Nature Mater.* 14 (2015) 23–36.
- [12] P. Colombo, C. Vakifahmetoglu, S. Costacurta, Fabrication of ceramic components with hierarchical porosity, *J. Mater. Sci.* 45 (2010) 5425–5455.
- [13] T. Ohji, M. Fukushima, Macro porous ceramics: processing and properties, *Int. Mater. Rev.* 57 (2012) 115–131.
- [14] S. Deville, Freeze-casting of porous ceramics: A review of current achievements and issues, *Adv. Eng. Mater.* 10 (2008) 155–169.
- [15] T. Fukasawa, Z. Y. Deng, M. Ando, Pore structure of porous ceramics synthesized from water-based slurry by freeze-dry process, *J. Mater. Sci.* 36 (2001) 2523–2527
- [16] R. F. Chen, C. A. Wang, Y. Huang, L. G. Ma, W. Y. Lin, Ceramics with special porous structures fabricated by freeze-gelcasting: using tert-butyl alcohol as a template, *J. Am. Ceram. Soc.* 90 (2007) 3478–3484.
- [17] Y. F. Tang, S. Qiu, C. Wu, Q. Miao, K. Zhao, Freeze cast fabrication of porous ceramics using tert-butyl alcohol–water crystals as template, *J. Eur. Ceram. Soc.* 36 (2016) 1513–1518.
- [18] T. Fukasawa, M. Ando, T. Ohji, S. Kanzaki, Synthesis of Porous Ceramics with Complex Pore Structure by Freeze-Dry Processing, *J. Am. Ceram. Soc.* 84 (2001) 230–232.
- [19] E. Munch, E. Saiz, A. P. Tomsia, Architectural control of freeze-cast ceramics through additives and templating, *J. Am. Ceram. Soc.*, 92 (2009) 1534–1539.
- [20] P. Colombo, M. Modesti, Silicon oxycarbide ceramic foams from a preceramic polymer, *J. Am. Ceram. Soc.* 82 (1999) 573–578.
- [21] M. Hojamberdiev, R. M. Prasad, K. Morita, Y. F. Zhu, M. A. Schiavon et al., Template-free synthesis of polymer-derived mesoporous SiOC/TiO<sub>2</sub> and SiOC/N-doped TiO<sub>2</sub> ceramic composites for application in the removal of organic dyes from contaminated water, *Appl. Catal. B* 115–116 (2012) 303–313.
- [22] C. Vakifahmetoglu, P. Colombo, A. Pauletti, C. F. Martin, F. Babonneau, SiOC ceramic monoliths with hierarchical porosity, *Int. J. Appl. Ceram. Technol.* 7 (2010) 528–535.
- [23] H. Schmidt, D. Koch, G. Grathwohl, P. Colombo, Micro-/macroporous ceramics from preceramic precursors, *J. Am. Ceram. Soc.* 84 (2001) 2252–2255.
- [24] C. Vakifahmetoglu, I. Menapace, A. Hirsch, L. Biasetto, R. Hauser et al., Highly porous macro- and micro-cellular ceramics from a polysilazane precursor, *Ceram. Int.* 35 (2009) 3281–3290.
- [25] M. Adam, S. Kocanis, T. Fey, M. Wilhelm, G. Grathwohl, Hierarchically ordered foams derived from polysiloxanes with catalytically active coatings, *J. Eur. Ceram. Soc.* 34 (2014) 1715–1725.

- [26] C. Q. Hong, X. H. Zhang, J. C. Han, J. C. Du, W. B. Han, Ultra-high-porosity zirconia ceramics fabricated by novel room-temperature freeze-casting, *Scripta Mater.* 60 (2009) 563–566.
- [27] B. H. Yoon, C. S. Park, H. E. Kim, Y. H. Koh, In situ synthesis of porous silicon carbide (SiC) ceramics decorated with SiC nanowires, *J. Am. Ceram. Soc.* 90 (2007) 3759–3766.
- [28] T. Fukasawa, Z.Y. Deng, M. Ando, T. Ohji, S. Kanzaki, Synthesis of porous silicon nitride with unidirectionally aligned channels using freeze-drying process, *J. Am. Ceram. Soc.* 85 (2002) 2151–2155.
- [29] B. H. Yoon, E. J. Lee, H. E. Kim, Y. H. Koh, Highly aligned porous silicon carbide ceramics by freezing polycarbosilane/camphene solution, *J. Am. Ceram. Soc.* 90 (2007) 1753–1759.
- [30] M. Naviroj, S. M. Miller, P. Colombo, K. T. Faber, Directionally aligned macroporous SiOC via freeze casting of preceramic polymers, *J. Eur. Ceram. Soc.* 35 (2015) 2225–2232.
- [31] H. X. Zhang, P. D. Nunes, M. Wilhelm, K. Rezwan, Hierarchically ordered micro/meso/macroporous polymer-derived ceramic monoliths fabricated by freeze-casting, *J. Eur. Ceram. Soc.* 36 (2016) 51–58.
- [32] A. P. Rao, A. V. Rao, Modifying the surface energy and hydrophobicity of the low-density silica aerogels through the use of combinations of surface-modification agents, *J. Mater. Sci.* 45 (2010) 51–63.
- [33] M. J. Owen, P. J. Smith, Plasma treatment of polydimethylsiloxane, *J. Adhesion Sci. Technol.* 8 (1994) 1063–1075.
- [34] J. H. Kim, P. K. Park, C. H. Lee, H. H. Kwon, Surface modification of nanofiltration membranes to improve the removal of organic micro-pollutants (EDCs and PhACs) in drinking water treatment: graft polymerization and cross-linking followed by functional group substitution, *J. Memb. Sci.* 321 (2008) 190–198.
- [35] O. Duman, S. Tunc, Electrokinetic and rheological properties of Na-bentonite in some electrolyte solutions, *Micropor. Mesopor. Mat.* 117 (2009) 331–338.
- [36] M. Scheffler, T. Gambaryan-Roisman, T. Takahashi, J. Kaschta, H. Muenstedt et al., Pyrolytic decomposition of preceramic organo polysiloxanes, *Ceram. Trans.* 115 (2000) 239–250.
- [37] T. Prenzel, M. Wilhelm, K. Rezwan, Tailoring amine functionalized hybrid ceramics to control CO<sub>2</sub> adsorption, *Chem. Eng. J.* 235 (2014) 198–206.
- [38] T. Prenzel, M. Wilhelm, K. Rezwan, Pyrolyzed polysiloxane membranes with tailorable hydrophobicity, porosity and high specific surface area, *Micropor. Mesopor. Mat.* 169 (2013) 160–167.
- [39] S. Deville, E. Saiz, A. P. Tomsia, Ice-templated porous alumina structures, *Acta Mater.* 55 (2007) 1965–1974.
- [40] M. Esfahanian, R. Oberacker, T. Fett, M. J. Hoffmann, Development of dense filler-free polymer-derived SiOC ceramics by field-assisted sintering, *J. Am. Ceram. Soc.* 91 (2008) 3803–3835.
- [41] T. Halfer, A. Rei, L. C. Ciacchi, L. Treccani, K. Rezwan, Selective covalent immobilization of ferritin on alumina, *Biointerphases* 9 (2014) 031018(1–9).

- [42] A. I. Baranova, T. A. Pryakhina, E. S. Afanas'ev, B. G. Zavin, Ya. S. Vygodskii et al., Anhydride modified silica nanoparticles: preparation and characterization, *Appl. Surf. Sci.* 258 (2012) 3168–3172.
- [43] B. Jastorff, R. Störmann, J. Ranke, Thinking in structure-activity relationships - A way forward towards sustainable chemistry, *Clean* 35 (2007) 399–405.
- [44] G. Jean, V. Sciamanna, M. Demuyne, F. Cambier, M. Gonon, Macroporous ceramics: novel route using partial sintering of alumina-powder agglomerates obtained by spray-drying, *Ceram. Int.* 40 (2014) 10197–10203.
- [45] C. Brandes, L. Treccani, S. Kroll, K. Rezwan, Gel casting of free-shapeable ceramic membranes with adjustable pore size for ultra- and microfiltration, *J. Am. Ceram. Soc.* 97 (2014) 1393–1401.
- [46] B. Besser, T. Veltzke, J. A. H. Dreyer, J. Bartels, M. Baune et al., A comparative experimental study on the deviation of the ideal selectivity in DTMS-functionalized and untreated ceramic structures with pores in the upper mesoporous range, *Micropor. Mesopor. Mat.* 217 (2015) 253–261.
- [47] J. Bartels, M. N. Souza, A. Schaper, P. Árki, S. Kroll et al., Amino-functionalized ceramic capillary membranes for controlled virus retention, *Environ. Sci. Technol.* 50 (2016) 1973–1981.
- [48] B. Wicklein, A. Kocjan, G. Salazar-Alvarez, F. Carosio, G. Camino et al., Thermally insulating and fire-retardant lightweight anisotropic foams based on nanocellulose and graphene oxide, *Nat. Nanotech.* 10 (2015) 277–283.



## 7. Cryogenic properties of unidirectional porous SiOC ceramics

**Adapted from:** *Macro/mesoporous SiOC ceramics of anisotropic structure for cryogenic engineering*

**Published in:** *Materials & Design*, 134 (2017) 207–217.

**Authors:** Huixing Zhang<sup>1</sup>, Clara Lana Fedelis<sup>1</sup>, Michaela Wilhelm<sup>1\*</sup>, Zhipeng Xie<sup>2</sup> and Kurosch Rezwan<sup>1,3</sup>

1. University of Bremen, Advanced Ceramics, Am Biologischen Garten 2, IW3, Germany

2. State Key Laboratory of New Ceramics and Fine Processing, Department of Materials Science & Engineering, Tsinghua University, Beijing 100084, PR China

3. MAPEX – Centre for Materials and Processes, University of Bremen, Am Fallturm 1, 28359 Bremen, Germany

\* Corresponding author. E-mail address: [mwillhelm@uni-bremen.de](mailto:mwillhelm@uni-bremen.de)

DOI: 10.1016/j.matdes.2017.08.039

Reprint (adapted) with permission from Elsevier, license number: 4180321197359

### Abstract

Macro/mesopore SiOC ceramic monoliths of anisotropic structure were prepared by freeze casting, using methy phenyl polysiloxane (H44) or methy polysiloxane (MK) and (3-aminopropyl)triethoxysilane (APTES) as precursors. Influence of pyrolysis and testing temperature on compressive strength was investigated. Monoliths pyrolyzed at 700 °C had the highest compressive strength both at 77 K ( $14.0 \pm 4.3$  MPa) and 293 K ( $7.7 \pm 1.8$  MPa), regardless of precursors. Compressive strength of monolith in parallel direction is around twice as much as perpendicular direction. Compressive strength of both monoliths in liquid nitrogen (77 K) was around twice of that in air (293 K) probably due to low temperature and liquid resistance. Anisotropic expansion was observed, and the shrinkage in parallel direction was almost twice of that in perpendicular direction, which can be verified by the Schapery equation. Monolith made from H44 showed a much higher coefficient of thermal expansion at 77 K than monolith made from MK and APTES, probably due to difference in composition and measurement condition. Thermal conductivities and specific heat capacities displayed an upward trend from low to warmer temperature. The minimum and maximum values for thermal conductivity are 0.2 and 0.9  $\text{W} \cdot \text{m}^{-1} \cdot \text{K}^{-1}$ . The maximum heat conductivities might be determined mainly by the macroporosity and the thermal conductivity of the hybrid material.

### Keywords:

Macropore, Polymer derived ceramics, Cryogenic temperature, Thermal properties, Compressive strength

### 7.1 Introduction

Solid ceramics have attracted a lot of attention in cryogenic engineering; as supporting materials for superconducting magnet systems [1], as fuel cladding in nuclear power applications [2], and as bearings working in pressurized cryogenic fluids in space technology [3]. In the space industry, not only solid materials, but also porous structures have useful applications; porous materials have been used for phase separation and transport of storable and cryogenic fluids, such as liquid acquisition devices and propellant management devices. They enable a gas-free propellant delivery to the spacecraft's engines via capillary pressure driven flows in porous elements and bubble point pressure [4–6]. The delivery of cryogenic propellants in propellant management devices, in a system such as one that uses liquid O<sub>2</sub> as the oxidizer (boiling point 90 K) and liquid H<sub>2</sub> as the fuel (boiling point 20 K), etc. by capillary transport via porous medium, such as metallic weave, allows propellants to be transported without gravitational force in space. Zhang et al. investigated wicking (capillary rising) of liquid nitrogen into a porous metal weave in an open cryogenic chamber [7]. Grebenyuk et al. studied the wicking of liquid nitrogen into glass frits under isothermal conditions (77 K) [8]. Compared to metallic weaves, macroporous monolithic ceramics have a low density, high mechanical strength, and excellent corrosion resistance, making them potentially excellent mediums for cryo-wicking. Considering the wicking pumping capability and the wick permeability, the macropore size for this application should be around several to tens of micrometers [7–8]. Notably, the wicking behaviours of macroporous ceramics have also been studied for capillary-based heat pipes [9]. Different propellant liquids have different surface energy, thus adjustable surface characteristics of materials are preferred. The use of preceramic polymers as precursors for producing polymer-derived ceramics enables the adjustment of surface characteristics and the microporous structure [10].

Fabrication of macroporous ceramic monoliths using preceramic polymers faces numerous challenges for the wicking process, due to the relatively large monoliths required (several centimetres to tens of centimetres). A few methods are commonly used to produce macroporous ceramic monoliths: sacrificial templating, direct foaming, the replica method, and additive manufacturing [11]. The sacrificial template method results in samples with narrow pore size distributions, however, this method may be limited to membranes or small size sample to avoid severe shrinkage and cracking caused by template evacuation, which is particularly noticeable for large, bulky monoliths [12]. The direct foaming method normally results in samples with relatively wide pore size distributions and larger pores [13]. The freeze casting method, which is a special sacrificial templating method, is a good option for the fabrication of macropore monoliths with narrow pore size distributions [14].

The ceramics are fabricated at room temperature, but operate at cryogenic temperature. Additionally, they carry loads between ambient and low temperature components. Thus, it is very important to investigate the thermal and mechanical properties of the ceramics at cryogenic to room temperatures. There has been extensive investigation of mechanical properties of the ceramics at room temperature or higher temperatures, however, mainly on nonporous materials,

like ceramic matrix composites (CMC) [15], yttria-stabilized zirconia [16] or bioceramics [17]. For porous ceramics, mechanical property investigations have also been focused mainly on room or high temperature behavior. Seuba et al. investigated that honeycomb out-of-plane model derived by Gibson and Ashby can be applied to describe the compressive behavior of unidirectional porous yttria-stabilized zirconia prepared by freeze casting [18], in their work, maximum compressive strength of 286 MPa was achieved for sample with 49.9% porosity and pore size of 3  $\mu\text{m}$ . Dey et al. investigated the porosity-dependent variation of fracture strength (9–34 MPa) and elastic modulus (7–28 GPa) of mullite-bonded porous SiC ceramics at room temperature [19]. The flexural strength ( $57\pm 6$  MPa) and fracture toughness ( $1.5\pm 0.1\text{MPa}\cdot\text{m}^{1/2}$ ) of freeze-cast porous  $\text{Si}_3\text{N}_4$  composites have also been investigated, and the mechanical properties can be improved with addition of polyacrylamide (PAM) [20]. Meille investigated the transition of elastic, brittle, and cellular behavior of porous ceramics when porosity (30%–75%) and pore size (hundreds microns to several microns) changed, maximum compressive strength  $170\pm 68$  MPa and minimum compressive strength of  $9\pm 1.2$  MPa [21] were found. Mechanical properties of silicon oxycarbide ceramic foams have also been investigated, compressive strength ranged from  $1.31\pm 0.51$  MPa ( $600\pm 145$   $\mu\text{m}$ ) to  $9.90\pm 1.78$  ( $100\pm 40$   $\mu\text{m}$ ) was obtained depending on the foam density, and longer exposure to 1200  $^\circ\text{C}$  led to the decrease of compressive strength [22].

Thermal properties of the crystalline and/or amorphous dense ceramics at cryogenic temperatures or higher have been examined. Normally the thermal conductivity of SiC is measured at 300 K. At this temperature single-crystalline SiC shows values in the range of 150 to 500  $\text{W}\cdot\text{m}^{-1}\cdot\text{K}^{-1}$  depending on the purity, polymorph, etc. High pure crystalline SiC measured from 3 K to 300 K showed a nonlinear thermal conductivity of 6–5200  $\text{W}\cdot\text{m}^{-1}\cdot\text{K}^{-1}$  and impurities decreased the conductivity greatly [23]. Thermal properties of ceramics for thermal barrier coatings have been reviewed by Cao et al., for example, at 1273 K thermal conductivities of  $\text{ZrO}_2$ , Mullite, and  $\text{Al}_2\text{O}_3$  are 1.56, 3.0 and 1.7  $\text{W}\cdot\text{m}^{-1}\cdot\text{K}^{-1}$  [24]. There are also work investigating thermal properties of porous ceramics at room or higher temperatures. Thermal conductivity of porous SiC (porosity  $\sim 70\%$ ) was observed to be  $\sim 2$   $\text{W}\cdot\text{m}^{-1}\cdot\text{K}^{-1}$  [25], a SiC foam with pore sizes between 0.4 and 2 mm showed 0.4–2.7  $\text{W}\cdot\text{m}^{-1}\cdot\text{K}^{-1}$  [26] and porous nano-SiC showed 2  $\text{W}\cdot\text{m}^{-1}\cdot\text{K}^{-1}$  at 300 K [27]. Ultra-low thermal conductivity 0.06  $\text{W}\cdot\text{m}^{-1}\cdot\text{K}^{-1}$  was achieved for porous yttria-stabilized zirconia (porosity 52–76%, pore size 0.7–1.8  $\mu\text{m}$ ) fabricated by tert-butyl alcohol (TBA)-based gel-casting process [28]. Thermal conductivity of porous alumina (porosity 6–47%, pore size 5–50  $\mu\text{m}$ ) was investigated from room temperature to 500  $^\circ\text{C}$  and the temperature dependence of different porosity was fitted with second-order polynomials and  $1/T$ -type relations [29]. The effective thermal conductivity of macroporous SiOC ceramics is 0.041 to 0.078  $\text{W}\cdot\text{m}^{-1}\cdot\text{K}^{-1}$  at room temperature, depending on the density [30]. There has been some theoretical work investigating the thermal conductivity bounds for isotropic porous materials [31] and analytical relations describing effective thermal conductivities with pore volume fractions [32]. Most of the work has focused on investigating the thermal properties of isotropic porous ceramics. Pappacena et al. studied the thermal conductivity of biomorphic anisotropic silicon

carbide at room and high temperatures [33]. However, little research has been performed on the thermal conductivity of anisotropic porous ceramics from cryogenic to room temperatures.

Our work intends to begin to fill this gap by investigating the thermal and mechanical properties of the anisotropic porous monoliths for cryogenic wicking. The derivation of porous ceramic monoliths of high permeability, low thermal conductivity and relatively high mechanical properties, provides a new horizon for porous materials for cryogenic applications, beginning with heat and mass transport.

## 7.2 Materials and methods

Macroporous ceramic monoliths were prepared by freeze casting, using hybrid fillers as the main solid phase. Two kinds of hybrid fillers were prepared, using different precursors: pure methyl phenyl polysiloxane (H44) and methyl polysiloxane (MK) together with (3-aminopropyl)triethoxysilane (APTES) by the following two different routes (A and B). These processes produced similar porous ceramics, however, different compositions. Two processes ( ) were chosen to investigate if the precursors and cross-linking will have an influence on the properties of final porous ceramics.

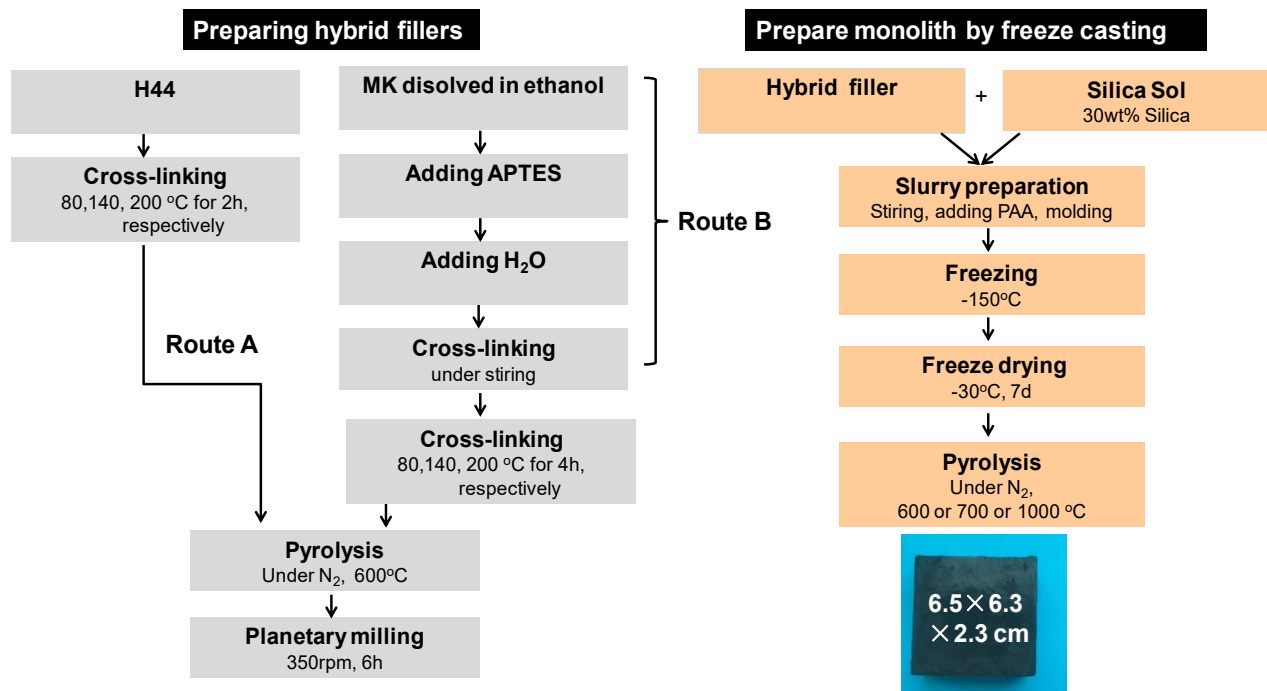


Figure 7.1: Process scheme, parameter variations of synthesized samples and the monolithic structure of the resulting pyrolyzed sample.

### 7.2.1 Preparation of hybrid filler

#### 7.2.1.1 Route A

H44 was pre-cross-linked using a multi-stage heat treatment in air at 353 K, 413 K, and 473 K (all dwell times 2 h), with a heating rate of  $60 \text{ K}\cdot\text{h}^{-1}$  between dwell times. The pre-cross-linked polysiloxane pieces were then pyrolyzed at  $600 \text{ }^\circ\text{C}$  (873 K) under nitrogen atmosphere. The heating rate was set to  $120 \text{ K}\cdot\text{h}^{-1}$ , up to  $500 \text{ }^\circ\text{C}$  (773 K), and then  $30 \text{ K}\cdot\text{h}^{-1}$  to the final temperature, with a dwell time of 4 h. These fillers were given the nomenclature “H44-600”.

#### 7.2.1.2 Route B

MK was first dissolved in ethanol, and then mixed with (3-aminopropyl)triethoxysilane (APTES) in a molar ratio of 1:1. Water is used to catalyze cross-linking. A solid was formed gradually and then transferred to a cross-linking oven using a multi-stage heat treatment in air, at 353, 413, and 473 K (all dwell times 4 h), with a heating rate of  $60 \text{ K}\cdot\text{h}^{-1}$  in between dwell times. The pre-cross-linked polysiloxane pieces were then pyrolyzed at  $600 \text{ }^\circ\text{C}$  (873 K) under a nitrogen atmosphere. The pyrolysis conditions were the same as route A (above). These fillers followed the nomenclature “MK-APTES-600”. More details about preparation can be found in previous literature [34]. Fillers obtained by both routes were ground by planetary ball milling at  $350 \text{ r}\cdot\text{min}^{-1}$  for 6 h to get fine powders. The particle sizes are mostly below  $1 \text{ }\mu\text{m}$ , [34] and due to the surface charges of the particles, particle separation by sieving was not possible. These powders were ready to be used in freeze casting steps.

### 7.2.2 Freeze casting process

30 wt% (weight percent) of precursor powders were added to 70 wt% of silica sol (with 30 wt%  $\text{SiO}_2$  nanoparticles, 8 nm, BegoSol® K, BEGO) under stirring. The silica sol acted as a binder and water source during the freezing process. The pH was adjusted between 6 and 7, using polyacrylic acid (PAA, Sigma) to ensure that the condensation reaction of the silica sol proceeded to completion. The obtained slurry was then placed under vacuum at 300 mbar for 5 min to eliminate bubbles created during stirring. It was then poured into a mold, which comprised of two aluminum plates and a PVC U-shaped mold (see Appendix Figure A8). This was quickly transferred to a deep freezer ( $-123 \text{ K}$ ) for half an hour. The samples were then dried in a freeze dryer for 7 days at 243 K. Finally, they were pyrolyzed at  $600 \text{ }^\circ\text{C}$  ( $\sim 873 \text{ K}$ ),  $700 \text{ }^\circ\text{C}$  ( $\sim 973 \text{ K}$ ) and  $1000 \text{ }^\circ\text{C}$  ( $\sim 1273 \text{ K}$ ) in an atmosphere of nitrogen. The monoliths were given the nomenclature “H44-600-xxx” and “MK-APTES-600-xxx”, depending on the fillers used.

### 7.2.3 Characterizations

The solid (true density) densities of both monoliths were measured by Helium pycnometer (Accupyc 1330, Micromeritics, USA). The particle sizes and pore morphologies of samples were analyzed with scanning electron microscopy (SEM, field-emission SEM SUPRA 40, Zeiss, Germany) operating at 2.00 kV mounted on carbon tape. Samples were embedded in resin and

polished and later sputtered with gold before measurements. Mercury intrusion porosimetry (Pascal 140/440, POROTEC GmbH, Germany) was used to determine macroporosities. Water vapour adsorption measurements were carried out by placing vessels with ~0.5 g of sample powder (particle sizes  $\leq 300 \mu\text{m}$ ) inside closed Erlenmeyer flasks filled with the solvents at equilibrium with their vapour phase at room temperature. Samples were weighed at the start and end of a 24 h measurement period in order to determine the vapour uptake of the material. Compression tests at 77 K and room temperature were performed on a universal testing machine (Zwick/Roell 2005, Zwick, Germany) universal testing machine, using cylinder monolith samples, at a constant displacement rate of 0.5 mm/min. The samples were cut in two different directions and two types of cylinder monoliths (Diameter: 9.4–9.5 mm, height 9.4–9.5 mm) were obtained for compression tests; the first with lamellar pores parallel to the cylinder axis, and the second with pores perpendicular to cylinder axis. The compression tests were carried out in liquid nitrogen (77 K), ethanol-dry ice bath (195 K), pure ethanol bath (293 K) and in air (293 K). Ten specimens were tested for each experimental condition. For the compression test at low temperatures, the samples were dried at 343 K for 7 days. Prior to and during the test, the samples were immersed under the liquid nitrogen/ethanol-dry ice bath and liquid nitrogen/ethanol-dry ice was added continuously so that the monoliths were always fully submerged in the liquids to avoid the formation of ice in the pores before and during the loading and equilibrate inner temperature with the liquids. A steel half sphere made of (diameter: 12 mm) was placed on the top of the monolith in order to minimize the effects of superficial defects and misalignment during the compression test. Compressive strength was calculated based on maximum load at the end of the elastic stage. The linear thermal expansions were measured using a strain gauge (Type: BB120-2AA-W250, Gauge Factor:  $1.74 \pm 1 \%$ , Zhonghang Electronic Measuring Instruments Co., LTD, China) over a temperature range of 80-300 K. The fused silica was measured at the same time, and its corresponding linear thermal expansion data was used as a reference. Before the measurement, the samples were glued to the strain gauge using epoxy and pressed between 2 plates to ensure the full contact of sample and strain gauge. The sample with the strain gauge was then dried for 24 h. The sample with the strain gauge was put inside a closed measurement cell, cooled by liquid nitrogen inside a thermal insulator, and the thermal expansion was measured during the warming up of the sample. Specific heat capacity was measured using differential scanning calorimetry (DSC, TA instruments) from 100 K to 293 K. The water content in the samples was investigated by thermogravimetric analysis (STA 503, Baehr), under a flow of nitrogen ( $2 \text{ L}\cdot\text{h}^{-1}$ ), using heating rates of  $2 \text{ K}\cdot\text{min}^{-1}$ . Thermal conductivities were measured under the condition of steady-state longitudinal heat flow in vacuum from 77 K to 293 K. Steady-state method measured the heat flux through a length in the directional normal to a surface area; under a steady-state temperature difference (temperature difference does not change with time). In this work, rectangular shaped samples were used and two sides of the sample were glued by silver conductive adhesive to the two copper plates, acting as a heat source and a heat sink with known power output, which resulted in temperature drop across a given length and the temperatures at both sides were recorded. Both thermocouples and thermometers were used in this apparatus, and the details about the

configuration and measurement can be found in the work of Liu et al. [35]. The steady-state technique used in this paper is an absolute technique, the sample was directly placed between a heat source and a heat sink, and therefore, no reference was used. The thermal conductivity was calculated by the software based on one-dimensional Fourier conduction equation.

$$Q = -\frac{AdT}{dx} \quad (7.1)$$

Where  $Q$  is the heat flow rate,  $\kappa$  is the thermal conductivity,  $A$  is the cross-sectional area, and  $dT/dx$  is the temperature gradient. Low temperatures were achieved via compressed argon. Prior to the thermal conductivity measurement, the sample was glued to a measurement plate using a thin layer of silver conductive adhesive (adhesive viscosity was high, in order to avoid penetration into the porous sample), then dried overnight.

### 7.3 Results

The polysiloxanes convert at 1000 °C completely from preceramic polymers to ceramics and the FTIR of the materials used in this work can be seen from the literature [36]. The compositions of SiOC materials prepared with different precursors are consisted of domains of SiO<sub>2</sub>, and free carbon [37]. The solid density (independent of porosity) of H44-600-1000 is 2.0763 ± 0.0048 g·cm<sup>-3</sup>, and the solid density of MK-APTES-600-1000 is 2.3145 ± 0.0055 g·cm<sup>-3</sup>. The solid density of H44-600-1000 is lower than that of MK-APTES-600-1000; therefore, the free carbon content is higher in H44-600-1000.

The macroporosity of the monoliths prepared with two different fillers were measured by Hg-porosimetry, as shown in Figure 7.2. The two monoliths have similar open porosities and pore size distributions; 58% and 20–50 μm for H44-600-1000, and 55% and 20–50 μm for MK-APTES-600-1000. The similarities in macroporosity are likely due to the same weights of solid loading and precursor particle sizes and freezing conditions. The slight differences in porosity and pore sizes might be due to solid volume differences of fillers, macrostructures changed slightly after pyrolysis.

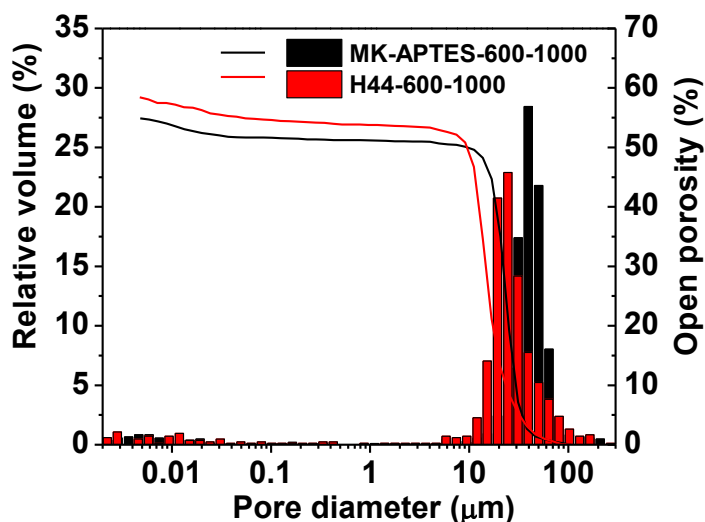


Figure 7.2: Pore size distribution versus relative pore volume and open porosity curves obtained from Hg-porosimetry of pyrolyzed samples prepared with two different precursors.

Figure 7.3 shows cross-sectional view of pores parallel to monolith axis. Both H44-600-1000 and MK-APTES-600-1000 show the similar structure. The geometry of the macroporosity is the negative replica of the ice crystals that formed during the freeze casting. Water crystallizes in the hexagonal crystal system, with the ice crystals having a growth velocity much faster in the *a*-direction of the hexagonal base than in the perpendicular *c*-direction. As a result, ice crystals develop a lamellar microstructure parallel to the *a*-direction, resulting in a lamellar spacing. The ice front propagation follows the temperature gradient, which was controlled by the configuration of the mold in this work. The SEM shows the unidirectional porous structure of the monolith. The lamellar pore size is defined as the distance between walls. Figure 7.3a shows that the lamellae length can be up to several millimetres. Figure 7.3b–c illustrates that the distance between lamellar walls is around 30  $\mu\text{m}$ , which agrees with the result of Hg intrusion porosimetry. Additionally, mesoporosity were observed in the samples, and were very similar for both samples, as shown in Figure A9 in Appendix A3.



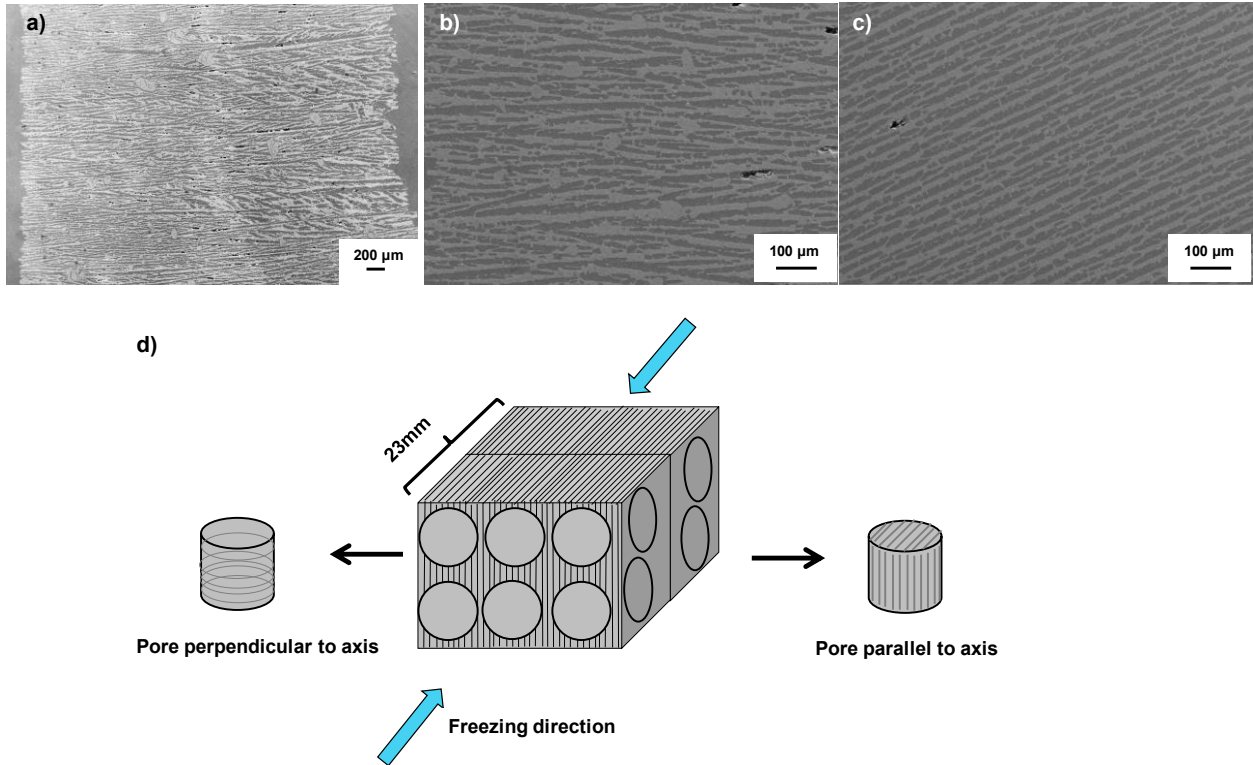


Figure 7.3: SEM images of pyrolyzed monoliths. a-b) Cross section showing pores parallel to H44-600-1000 monolith axis, c) Cross section showing pores parallel to MK-APTES-600-1000 monolith axis, d) schematic of monoliths cut from different directions.

During the freezing process, temperature gradients extended from the aluminum plates to the centre of the mold, as shown in Figure A8 in Appendix A3. This resulted in a monolith with unidirectional pores, however, a “stitching” structure would result in the very middle, as shown in Figure 7.3d. This was observed when using double-sided freezing [38]. This stitching line is avoided during sample cutting for the compression test.

Additionally, the samples were placed under SEM before and after a 3-day liquid nitrogen immersion test; no obvious structural changes were observed (not shown in the article). Furthermore, no obvious crack propagation during the liquid nitrogen treatment could be observed. Both monoliths showed anisotropic compressive strength (Figure 7.4), with “parallel” directions having the higher strength than the perpendicular directions. Compressive strength at 293 K was calculated to be  $5.9 \pm 2.5$  MPa (parallel) and  $2.0 \pm 0.3$  MPa (perpendicular) for MKAPTES-600-1000 and  $4.3 \pm 1.3$  MPa (parallel) and  $1.6 \pm 0.9$  MPa (perpendicular) for H44-600-1000. The parallel direction, with more continuous solid material, had higher strength.

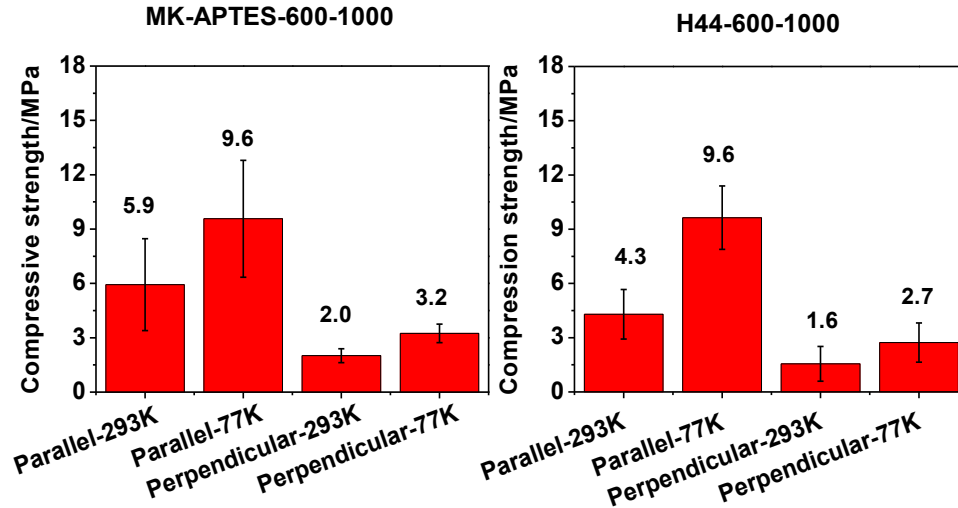


Figure 7.4: Compressive strength of monoliths pyrolyzed at 1000 °C, at 77 K inside liquid nitrogen and at room temperature in air.

Samples tested in liquid nitrogen (77 K) showed much higher compressive strength than those at 293 K in air. Compressive strength in parallel direction improved from 4.3 to 9.6 MPa and from 5.9 to 9.6 MPa for H44-600-1000 and MK-APTES-600-1000, respectively. The compressive strength of MK-APTES-600-1000 is slightly higher than that of H44-600-1000.

Statistical tests (t-test) were conducted with the resulting data. The compressive strength for parallel directions at two different temperatures 77 K and 293 K are statistically different ( $p < 5\%$ ) for both MKAPTES-600-1000 and H44-600-1000. For the perpendicular directions, however, the compressive strengths are not statistically different due to the relatively low compressive strength and high standard deviation. The lamellar porous structure makes it not possible to distinguish the cracks paths from the lamellar pores. Therefore, it cannot be determined if the temperature influence the fracture modes.

The influence of the pyrolysis temperature on compressive strength was investigated by pyrolysis at 600, 700, and 1000 °C, as shown in Figure 7.5. Anisotropic compressive strength was observed for all samples and compressive strength was influenced by pyrolysis temperature.

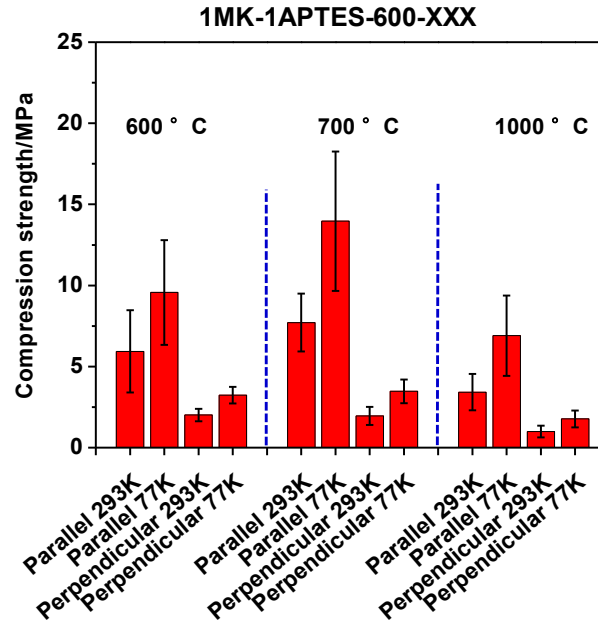


Figure 7.5: Compressive strength of the MK-APTES-600-xxx samples, pyrolyzed at 600, 700, and 1000 °C, tested at 77 K in liquid nitrogen and at 293 K in air.

Overall, samples pyrolyzed at 700 °C show higher compressive strengths than samples pyrolyzed at 600 °C and 1000 °C at both 77 K and 293 K. The compressive strength of MK-APTES-600-xxx monoliths (parallel) pyrolyzed at 600, 700, and 1000 °C were 5.94, 7.71, and 3.42 MPa at 293 K and 9.57, 13.96, and 6.90 MPa at 77 K, respectively. Pyrolysis temperature influenced not only the final composition, but also the porous structure of the ceramics.

Samples pyrolyzed at 600 °C were weaker due to the considerably higher numbers of mesopores compared to samples pyrolyzed at 700 and 1000 °C [34]. The lower compressive strengths of samples pyrolyzed at 1000 °C compared to those pyrolyzed at 700 °C might be ascribed to the lower fracture toughness of MK-APTES-600-1000, which is strongly related to the composition of the samples. The lower fracture toughness of ceramics led to monoliths being more sensitive to crack propagation during loading in the compression test, which resulted in lower compressive strength [39]. However, the toughness was not measured in this work.

The linear thermal expansions of the monoliths were investigated from 80 K to 293 K during the warming up of the sample, which were shown in Figure 7.6. Lattice contracted with decreasing temperature, which is typical for materials with positive coefficients of thermal expansion. The smooth plots indicated no phase transformations during the temperature variation and no detachment of strain gauge from sample surface. Both monoliths showed anisotropic coefficients of thermal expansion (CTE), and CTE in parallel direction is twice as that in perpendicular direction. The overall shrinkage of the MK-APTES-600-1000 at around 80 K

versus room temperature was 1.7 and 2.9‰, as well as 2.75 and 4.5‰ for H44-600-1000 in perpendicular and parallel directions, respectively.

The thermal expansion coefficients increased gradually with temperature from 80 K up to 250 K. From 250 K to 290 K, however, the measured CTEs increased substantially may be due to the large error introduced by the temperature drift of the sensor. The CTEs of MK-APTES-600-1000 increased from  $4.5 \times 10^{-6}$  to  $8.7 \times 10^{-6} \text{ K}^{-1}$  (perpendicular) and  $8.0 \times 10^{-6}$  to  $16.0 \times 10^{-6} \text{ K}^{-1}$  (parallel) in the temperature range of 80–250 K, while CTEs of H44-600-1000 increased from  $7.0 \times 10^{-6}$  to  $14.6 \times 10^{-6} \text{ K}^{-1}$  (perpendicular) and  $11.6 \times 10^{-6}$  to  $24.1 \times 10^{-6} \text{ K}^{-1}$  (parallel) in the temperature range of 80–250 K. It is worth mentioning that the thermal shrinkage of the H44-600-1000 samples was around twice as much as MK-APTES-600-1000.

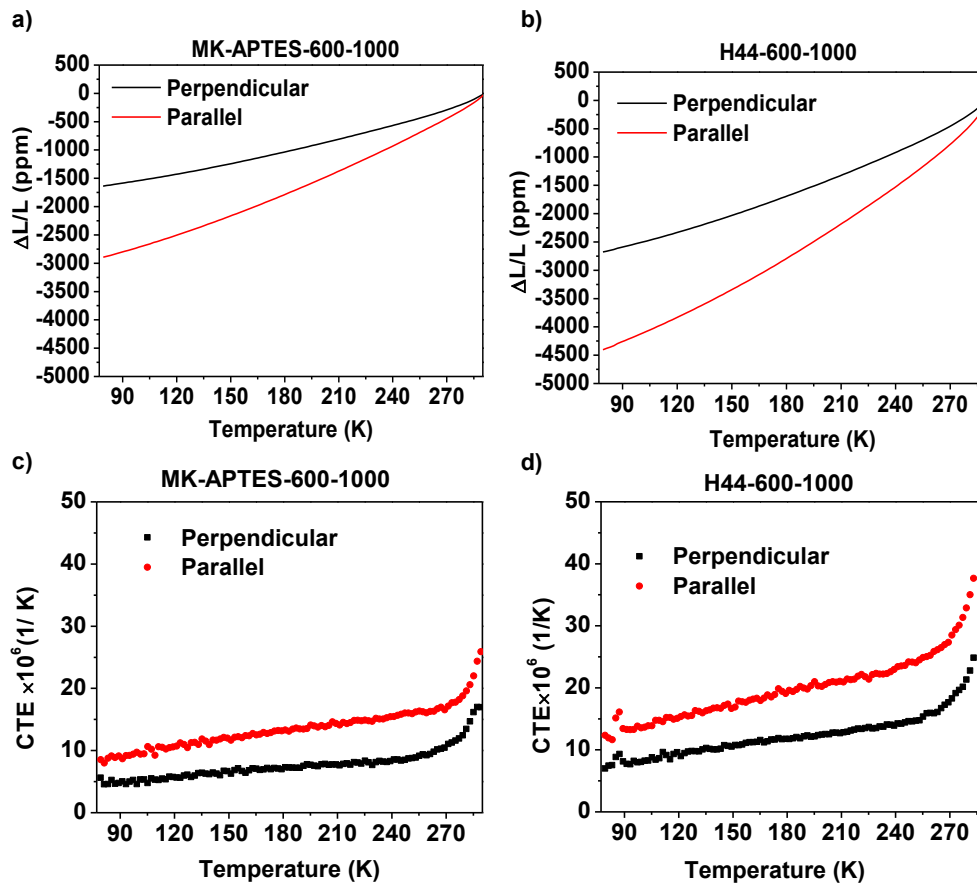


Figure 7.6: a–b) Linear thermal expansion and c–d) coefficient of thermal expansion (CET) of pyrolyzed monolith in two directions.

The thermal conductivity of the monoliths was measured with steady-state longitudinal heat flow from 77 K to room temperature (Figure 7.7). Anisotropic thermal conductivity was observed for both monoliths prepared with different fillers. With increasing temperature, thermal conductivity increased, analogous to similar amorphous materials, for which thermal conductivity is several orders of magnitude smaller than those of crystalline materials [40]. The minimum and

maximum values for thermal conductivity are  $0.2$  and  $0.9 \text{ W}\cdot\text{m}^{-1}\cdot\text{K}^{-1}$ ; comparable to nonporous SiOC ceramics (from  $153 \text{ K}$  to  $1200 \text{ K}$ ) [41]. The specific heat capacities of the samples were also investigated. Despite greatly differing compositions, the samples showed very similar  $C_p$  values: around  $0.319 \text{ J}\cdot\text{g}^{-1}\cdot\text{K}^{-1}$  at  $100 \text{ K}$  to  $0.740 \text{ J}\cdot\text{g}^{-1}\cdot\text{K}^{-1}$  at room temperature for H44-600-1000, and  $0.271 \text{ J}\cdot\text{g}^{-1}\cdot\text{K}^{-1}$  at  $100 \text{ K}$  to  $0.718 \text{ J}\cdot\text{g}^{-1}\cdot\text{K}^{-1}$  at room temperature for MK-APTES 600-1000-DSC. Specific heat capacity of MK-APTES-600-1000 increased with increasing temperature linearly from  $100 \text{ K}$  to room temperature. However, a little abnormality was observed for H44-600-1000 from  $90$  to  $160 \text{ K}$ , which cannot be explained so far.

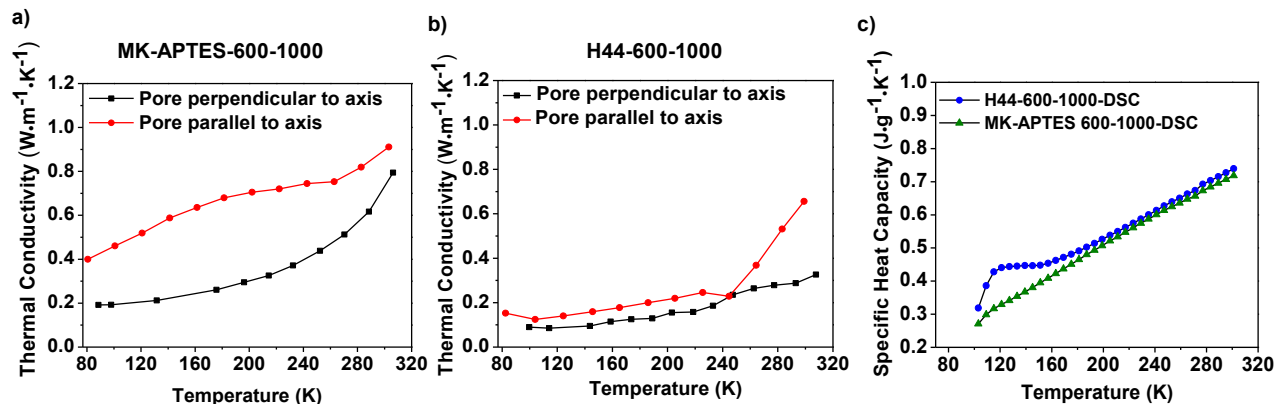


Figure 7.7: a–b) Thermal conductivity of the pyrolyzed ceramic monoliths from  $77 \text{ K}$  to room temperature using steady-state longitudinal heat flow, c) Specific heat capacity of two pyrolyzed ceramic monoliths, measured by DSC from  $100 \text{ K}$  to room temperature.

Lastly, permeability along the monolith axis (parallel) was measured with a modified falling head permeability test using water as the medium, and compressed air to vary the pressure (see Appendix Figure A10); this testing showed a permeability of  $3.5 \times 10^{-9} \text{ m}^2$ . The high permeability is ascribed to the open porosity of the unidirectional channels.

## 7.4 Discussion

### 7.4.1 The influence of environmental temperature on compressive strength

Some studies have shown that mechanical properties of solid ceramics improve at cryogenic temperatures. Zirconia-based ceramics have enhanced transformation toughening after cryogenic treatments, due to temperature-induced phase transformations [42]. Improved fracture strengths of reaction-bonded SiC composites [43] as well as  $\text{Si}_3\text{N}_4$ -SiC ceramics [44] were found at  $77 \text{ K}$  compared to that at  $293 \text{ K}$ , due to decreases in the cracks' effective size and increases in propagation resistance or more crack deflection (along crack propagation paths) at cryogenic temperatures. However, little work exists on the mechanical properties of amorphous porous ceramics, which involves no phase transformations.

For porous ceramics, compressive strength is normally influenced by the architecture, porosity, pore size, wall thickness, and ceramic bridges between lamellae, and the testing conditions — like loading speed or sample size. Compared to solid ceramics, when temperature is decreased, the distance between the atoms get smaller, and, accordingly, the pore size at all scales should decrease. The prepared SiOC ceramics have a hierarchically-ordered porous structure, including macropores, mesopores, and micropores (600 °C and 700 °C) [34]. The most significant structural influence on the compressive strength comes from the macropores, as they're the largest defects. One possible explanation for the improvements in the compressive strength of these samples may be the shorter interatomic distances at lower temperatures. It has been reported that compressive strength becomes stronger due to the lattice parameter change at cryogenic temperature [45]. This effect has been observed specifically for bulk metallic glasses  $Zr_{41.25}Ti_{13.75}Ni_{10}Cu_{12.5}Be_{22.5}$  at cryogenic temperatures, which also led to strength improvements [46]. In ceramics, the grain boundaries and the pores (cracks) can decrease the strength greatly. A fracture begins with crack nucleation and then propagates. The influence of crack size on the strength can be seen from Griffith equation:

$$\sigma_{Griffith} = \sqrt{\frac{2\gamma_0 E}{kl}} \quad (7.2)$$

Where  $l$  is the crack size,  $\gamma_0$  is the surface energy,  $E$  is the elastic modulus, and  $k$  is a dimensionless term related to crack and sample geometry. The shorter atom distances result in weaker atomic vibration and stronger interatomic interaction. Accordingly, the elastic modulus and surface energy increase. All those factors lead to the strength increase. Another reason for the strength improvement might be the liquid nitrogen entrapped in the pores. The compression test at 77 K was achieved by placing the samples directly into the liquid nitrogen. The liquid nitrogen entered the pores, due to the high permeability. During the compression test, the samples were immersed in liquid nitrogen, to keep the temperature equilibrium and to exclude moisture getting into the porous structure. Due to the little compressibility of both liquid and solid, the liquid cannot be squeezed out, and it was trapped inside the porous structure. Therefore, the porosity was 'lowered' due to the trapped liquid inside the structure, which led to the increased compressive strength. In order to investigate the influence of liquids on compressive strength, 'parallel' 1MK-1APTES-600-1000 was tested in ethanol-dry ice bath (195 K) and pure ethanol (293 K). The results are shown in Appendix Figure A11. The compressive strength at 195 K was higher than when tested at 77 K. The higher viscosity of ethanol compared with liquid nitrogen may be responsible for the difference. Compressive strength in pure ethanol (293 K) was much higher than tested in air (293 K). Thus, it can be surmised that the major improvements in compressive strength in liquid nitrogen were due to the liquid as well as the cryogenic temperature.

Due to the capillary effect provided by the porous structure, in addition to the relatively hydrophilic ceramic surface, water in the air condenses easily on the inner surfaces of the pores.

At cryogenic temperatures, these adsorbed water molecules may form ice grains inside the pores. The water vapour adsorption at room temperature, as well as the total cumulative volume determined from Hg intrusion porosimetry was used to evaluate possible water contents inside porous monoliths.

Taking the pore volume as measured by Hg intrusion as  $V_p$ , the water adsorption per gram of ceramics as  $W_{vapor}$ , the sample weight as  $m_s$  and the density of water as  $\rho$ , the volume of water adsorbed on the surface  $V_{water}$  may be calculated as:

$$V_{water} = \frac{W_{vapor} \times m_s}{\rho} \quad (7.3)$$

The volume percentage of water in the pores under saturated water vapour  $P_{water}$ , was calculated based on the following equation:

$$P_{water} = \frac{V_{water}}{V_p} \quad (7.4)$$

$P_{water}$  was calculated to be 12 vol.% and 11.6 vol.% for H44-600-1000 and MK-APTES-600-1000 respectively (vol.%: volume percentage). The water content in the air is much lower than the saturated atmosphere and samples were fully dried before being immersed into liquid nitrogen. Thermogravimetric analysis (see Figure A12 in Appendix A3) showed that the water adsorption is around 2.0 wt %; this increased to around 5.7 wt % after storing in air for one day. This can be viewed as the phase equilibrium of vapour and liquid water inside the capillaries. This shows that the volume of water in the pores was quite low, and the influence it may have had on the compressive strength of the monoliths was slight. In order to completely exclude the possibility of ice formation inside the porous material via atmospheric water vapour, further compression testing at cryogenic temperatures will need to be carried out in a protective atmosphere.

#### 7.4.2 Influence of compositions and anisotropy on coefficients of thermal expansion

The CTE of the H44-600-1000 sample was around twice as much as MK-APTES-600-1000. The composition difference between two monoliths contributed to the difference in thermal expansion. The solid density of H44-600-1000 is lower than that of MK-APTES-600-1000; therefore, free carbon content is higher in H44-600-1000. There have been reports using the composition to alter the CTEs [47–48]. Free carbon (forming turbostratic graphite domains) has generally higher thermal expansion than amorphous silica. Amorphous silica has a CTE lower than  $1.0 \times 10^{-6} \text{ K}^{-1}$  CTEs [49], however, amorphous carbon has a CTE of  $1.5\text{--}7.0 \times 10^{-6} \text{ K}^{-1}$  [50]. Besides composition difference, the measurement condition should be also responsible for the observed difference in the CTEs of the two monoliths. In contrast to CTEs of solid materials, the measurement conditions of porous materials need to be specified. There are two extreme

conditions: undrained condition or drained condition [51]. Drained condition corresponds to the behavior of dry porous materials or the case of slow heating of a porous material in a way that the excess pore pressure can be entirely dissipated, therefore, the pore pressure is constant, whereas in undrained condition, the mass of the fluid phase is constant, and the fluid in pore volume generates an excess pore pressure, therefore thermal expansion increases. The measured CTEs of porous SiOC were higher than CTEs of solid SiOC in the literature, around  $3.1 \times 10^{-6} \text{ K}^{-1}$ , which were measured at elevated temperature [52–53]. The measured CTEs of porous SiOC at cryogenic temperature can also be influenced by the measurement conditions. During measurement, samples were put inside a small closed, however, unvacuumed cell, therefore, the moisture which were previously present in the container, may condense in the samples during cooling. Considering that the surface characteristics of both materials are both hydrophilic, they might also contain a certain amount of water even after drying. Due to the small size of the cell and the fact that samples were covered by the strain gauge with glue, the large amounts of moisture from air should be excluded, so the measurement condition can be considered to be between undrained condition and drained condition. The plots  $\Delta L / L$  in Figure 7.6 are very smooth without abrupt change, which means that there is no obvious phase transformation (ice to water). This excluded great amounts of moisture inside the porous structure. However, the measurement condition may be responsible for relatively high CTEs of porous SiOC at cryogenic temperature.

The SiOC ceramic monoliths have anisotropic macroporous lamellar pores (porosity of 58% and 55%) and mesopores. Both macropores and mesopores should have no influence on the coefficients of thermal expansion [54–55]. Large and open pores play no role in the accommodation of thermal expansion, whereas the closed pores (transcrystalline cleavage cracks or microcracks created during temperature change) can accommodate thermal expansion [56], often result in anomalous thermal expansion, like negative and zero thermal expansion coefficients [57]. During cooling to cryogenic temperature, there were no macroscopic cracks observed in SiOC samples, however, microcracks cannot be determined due to the lamellar porous structure.

Lamellar porous SiOC monolith can be considered as ‘composite’ made of aligned solid walls and lamellar pores filled with air. There has been work, predicting the coefficients of thermal expansion of fiber reinforced ceramics [58] or composite materials [59] prepared by freeze-casting and infiltration by using the models proposed by Kerner [60] and Schapery [61]. According to Schapery equation, CTEs in the longitudinal direction (parallel)  $\alpha_l$  and transverse direction (perpendicular)  $\alpha_t$  are as following:

$$\alpha_l = \frac{E_p \alpha_p V_p + E_s \alpha_s V_s}{E_p V_p + E_s V_s} \quad (7.5)$$



$$\alpha_t = (1 + \nu_p)\alpha_p V_p + (1 + \nu_m)\alpha_s V_s - \alpha_l(\nu_p V_p + \nu_s V_s) \quad (7.6)$$

Where  $E$  is the elastic modulus,  $V$  is the volume fraction, and  $\alpha$  is the coefficient of thermal expansion,  $\nu$  is the Poisson's ratio. The subscripts  $s$  and  $p$  denote solid and pore (air). In case of porous materials,  $E_p$ ,  $\nu_p$ ,  $\alpha_p$  are zero, therefore  $\alpha_l = \alpha_s$ , and  $\alpha_t = \alpha_s V_s$ . These results mean that the CTEs in parallel direction should not change with the porosity, which can also be seen from the work of Nakajima [62], whereas the CTEs in perpendicular direction will be influenced by the porosity. The porosity of 1MK-1APTES-600-1000 and H44-600-1000 is 55% and 58%, therefore, the solid volume  $V_s$  is 45% and 42%.  $\alpha_t$  is around half the value of  $\alpha_l$ , which fits the theory very well.

### 7.4.3. Thermal conductivity of hierarchically-ordered porous monolith

The thermal conductivity of crystalline materials at lower temperatures rises before decreasing. The thermal conductivity of amorphous materials, however, increases with increasing temperature over this range, and is several orders of magnitude smaller than that of crystalline materials [63]. Impurities of less conductive materials, e.g.  $\text{SiO}_2$ , lower the overall conductivity of noncrystalline SiC material [23, 64]. Porosity also considerably lowers thermal conductivity; however, it is less significant than bulk crystallinity [27]. Thermal conductivity in porous materials is comprised of solid contribution (main contribution), gas contribution (significantly smaller comparing with solid), radiative contribution (negligible at low temperature), convection contribution (pores smaller than 3–4 mm, is negligible) [33].

Both monoliths have a hierarchically-ordered pore structure, with mesopores inside the lamellar walls. To understand the relationship between the thermal properties and the microstructure, the structure was simplified to a 2-phase mixture (gas-solid composition), as shown in Figure 7.8. The porous structure can be seen as layers of the solid separated by layers of air of uniform thickness, and the walls themselves had mesopores.

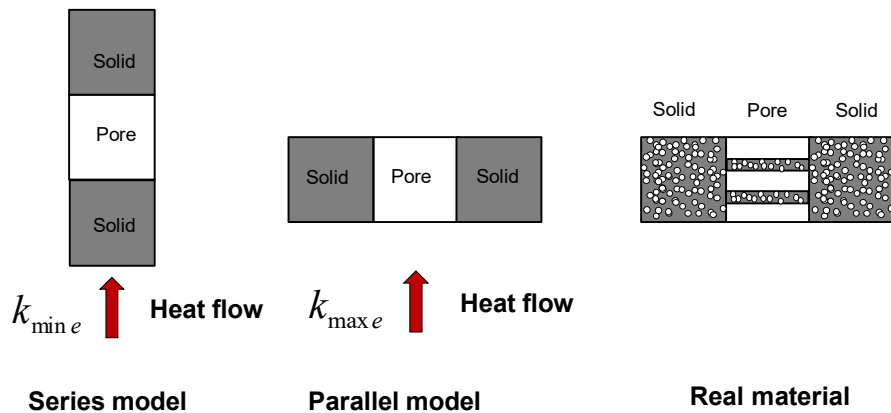


Figure 7.8: Parallel and series models and simplified structure of the real material. Walls contain mesopores (white spheres).

According to ‘series’ and ‘parallel’ models of thermal conductivity in a *i* phase, minimum effective thermal conductivity occurs in the series model, wherein the solid and the gas phases are in layers normal to the direction of heat flow. The maximum value of effective thermal conductivity occurs when the solid and gas phases are in layers parallel to the direction of heat flow, that is, the parallel model [65].

$$k_{\min e} = \frac{k_{s\text{-wall}}k_g}{k_{s\text{-wall}} + (1 - p)k_g} \quad (7.7)$$

$$k_{\max e} = k_g + (1 - p)k_{s\text{-wall}} \quad (7.8)$$

where  $k_{\min e}$  and  $k_{\max e}$  are the minimum and maximum effective thermal conductivity,  $p$  represents the macroporosity,  $k_{s\text{-wall}}$  and  $k_g$  denote the thermal conductivity of the lamellar walls and the gas, respectively. If the ‘gas’ phase is a vacuum,  $k_g$  is 0. The lower boundary  $k_{\min e}$  and upper boundary  $k_{\max e}$  were calculated to be 0 and  $k_{\max e} = (1 - p)k_{s\text{-wall}}$ , respectively. However, this cannot be directly applied to the investigated freeze cast materials. Since in the freeze casted materials, the lamellae walls have bridges between each other as shown in Figure 7.3, the bridges should be considered, shown in Figure 7.8. 8. A geometry factor  $C$  (at certain temperature range,  $C$  can be regarded as independent of temperature) is introduced. Then the  $k_g$  can be rewritten as  $k_g = Ck_{s\text{-wall}}$ . SiOC monolith was composed of nanodomains of  $\text{SiO}_2$  and carbon, which is a hybrid material, and there are mesopores on the lamellar walls. The mesopores, can be considered spherical pores, a randomly interconnected skeleton, forming a two-phase “gas-solid composite” system. The effective thermal conductivity of the walls fits the assumption of the Effective Medium Theory (EMT) model [66–67]. The EMT model

$$k_{s\text{-wall}} = \frac{1}{4} \left\{ (3v_{\text{meso-p}} - 1)k_g + (3v_{\text{solid}} - 1)k_{s\text{-hy rid}} + [(3v_{\text{meso-p}} - 1)k_g + (3v_{\text{solid}} - 1)k_{s\text{-hy rid}}] \right\} \quad (7.9)$$

can be simplified to:  $k_{s\text{-wall}} = \frac{1}{2}(3v_{\text{solid}} - 1)k_{s\text{-hy rid}}$  when the measurement having been conducted under vacuum,  $v_{\text{meso-p}}$ ,  $k_g$  ( $k_g = 0$ ) and  $k_{s\text{-hy rid}}$  represent the mesoporosity inside the walls and the thermal conductivity of the air and hybrid materials.  $v_{\text{meso-p}}$  is very small at 1000 °C pyrolysis, pushing  $k_{s\text{-wall}}$  very close to  $k_{s\text{-hy rid}}$ . The small influence of microscale spherical pores on the thermal conductivity at low temperatures (produced by gas emission during thermal decomposition) has also been reported by the Russell [68]. Therefore,  $k_{\max e} \approx (1 - p)k_{s\text{-hy rid}}$ ; the maximum heat conductivity was determined mainly by the macroporosity and the thermal conductivity of the hybrid material. Since thermal conductivities of amorphous materials increase with temperature, it makes sense that the measured effective conductivities also increased with temperature. As discussed before, the solid phase contained nanodomains of carbon and silica, and the mesopores are on the lamellae walls. When the fractions of silica and carbon nanodomains are known, the thermal conductivity of the hybrid solid can also be

calculated, based on the EMT model which has two solid-solid phases. However, the volume of carbon and silica in the hybrid is not known. Therefore, the thermal conductivity cannot be confirmed quantitatively. Thermal conductivity anisotropy decreases with increased solid loading, due to more bridges formed between lamellae. In this case, the bridge amounts are very similar for samples with both precursors [69].

### 7.4.4 Potential applications

The delivery of cryogenic propellants in propellant management devices are mainly governed by the behavior of cryogenic media in porous materials (cryo-wicking). The cryo-wicking is mainly influenced by the liquid properties in terms of density, surface energy, specific heat capacity, thermal conductivity, and the properties of the porous materials, such as density, specific heat capacity, thermal conductivity, porous structure, pore size and permeability, as well as the environmental conditions such as temperature of porous solid and cryogenic medial, etc. [8]. Due to the very low surface energy of liquid nitrogen ( $8.5 \text{ mN}\cdot\text{m}^{-1}$ ), the pore sizes for wicking should be within micrometer range. The pore size range ( $20\text{--}50 \mu\text{m}$ ), low thermal conductivity ( $0.2$  and  $0.9 \text{ W}\cdot\text{m}^{-1}\cdot\text{K}^{-1}$ ) and high permeability ( $3.5\times 10^{-9} \text{ m}^2$ ) of these porous materials render the materials used in cryogenic liquid transport. The wicking behavior of monolith with radial porous structure prepared by this method under isothermal condition at  $293 \text{ K}$  has been investigated [70], the details about wicking results can be found in Appendix A4. Materials for cryogenic wicking experiments or other space applications need to survive a series of critical treatments before testing, such as sunisoidal vibration, random vibration, ultrasonic bath treatment, and high vacuum environment for long term. However, some particles were observed detached from the monoliths of this work after treatments. Therefore the mechanical strength should be further improved to enable practical cryogenic applications. One possible way is to convert SiOC ceramic monolith to SiC ceramic monolith at higher pyrolysis temperature to diminish mesopores and increase the bonding strength. However, by this the thermal conductivity will be improved as well, which may cause easier heat leak. Therefore, further investigation on how to improve mechanical strength should be done. Besides, the large capillary pumping capacity (small pore size, high permeability), also render these materials open as wicks such as loop heat pipe for cooling electronic components [71].

### 7.5 Conclusion

Porous SiOC ceramics prepared with different polysiloxanes by different cross-linking processes showed that they have slight differences in mechanical and thermal properties. The thermal properties (thermal conductivity, specific heat capacity) and mechanical properties were mainly influenced by the amorphous nature and macroporous structure. For certain cryogenic applications, the anisotropic thermal and mechanical properties in parallel and perpendicular directions, which were shown by the anisotropic porous SiOC monoliths, are desired. The very low thermal conductivities and relatively high compressive strength are very promising for use in cryogenic engineering. The linear thermal expansion of both materials showed anisotropy, and

different CTEs for the two monoliths might be due to different compositions and measurement conditions. Liquid entrapped inside the porous structure and cryogenic temperature might both improve the compressive strength of porous monolith. The unidirectional structure resulted in a high permeability, facilitating a high liquid pumping ability, which is not only suitable for fluid mass transport at cryogenic temperatures, but also similar applications at higher temperatures.

### Acknowledgments

This work was supported by German Research Foundation (DFG) within the research training group GRK 1860 “Micro-, meso- and macroporous nonmetallic Materials: Fundamentals and Applications” (MIMENIMA). The authors thank Prof. Laifeng Li, Prof. Rongji Huang, Xinran Shan and Yuqiang Zhao in Key Laboratory of Cryogenics, Technical Institute of Physics and Chemistry, Chinese Academy of Sciences for their support in measuring the thermal expansion coefficients and thermal conductivity by stable flow method at cryogenic temperatures. The authors thank Vassilios Siozios in Application Thermal Analysis unit in TA Instruments (Waters GmbH) for carrying out low temperature specific heat capacity measurements. H.X. Zhang thanks Prof. Zhipeng Xie for hosting her as visiting researcher at Tsinghua University, China in order to carry out the low temperature measurement. The authors thank Prof. Michael Dreyer and Yulia Grebenyuk at the Center of Applied Space Technology and Microgravity, University of Bremen, for their discussions about potential materials for capillary transport of cryogenic liquids. The authors thank Dr. Thomas Schumacher (University of Bremen), for helping design cryogenic container for compression test and Dr. Evgeny Pogorelov (University of Bremen), for his helpful comments about permeability measurements and thermal properties. The authors thank Harrison Reid (University of Bremen) for language proof reading.

### References

- [1] L. F. Li, Y. Y. Li, O. Sbaizero, S. Meriani, ZrO<sub>2</sub>–CeO<sub>2</sub> alloys as candidate structural materials for cryogenic application, *J. Am. Ceram. Soc.* 80 [4] (1997) 1005–1008.
- [2] E. Rohmer, E. Martin, Christophe Lorrette, Mechanical properties of SiC/SiC braided tubes for fuel cladding, *J. Nucl. Mater.* 453 (2014) 16–21.
- [3] R. Khanna, B. Basu, Sliding wear properties of self-mated yttria-stabilized tetragonal zirconia ceramics in cryogenic environment, *J. Am. Ceram. Soc.* 90 [8] (2007) 2525–2534
- [4] D. E. Jaekle, Propellant management device conceptual design and analysis: galleries, AIAA-97-2811, 1997.
- [5] M. Wollen, F. Merino, J. Schuster, C. Newton, Cryogenic propellant management device: conceptual design study, NASA/CR-010-216777, 2010.
- [6] D. J. Chato, M. T. Kudlac, Screen channel liquid acquisition devices for cryogenic propellants, AIAA-2002-3983, 2002.

- [7] T. Zhang, P. de Bock, E. W. Stautner, T. Deng, C. Immer, Demonstration of liquid nitrogen wicking using a multi-layer metallic wire cloth laminate, *Cryogenics* 52 (2012) 301–305.
- [8] Y. Grebenyuk, M. E. Dreyer, Wicking of liquid nitrogen into superheated porous structures, *Cryogenics* 78 (2016) 27–39.
- [9] B. Seidenberg, T. D. Swanson, Ceramic heat pipe wick, US 4883116 A
- [10] T. Prenzel, M. Wilhelm, K. Rezwani, Pyrolyzed polysiloxane membranes with tailorable hydrophobicity, porosity and high specific surface area, *Micropor. and Mesopor. Mat.* 169 (2013) 160–167.
- [11] E. C. Hammel, O. L. R. Ighodaro, O. I. Okoli, Processing and properties of advanced porous ceramics: An application based review, *Ceram. Int.* 40 (2014) 15351–15370.
- [12] P. Colombo, E. Bernardo, Macro- and micro-cellular porous ceramics from preceramic polymers, *Compos. Sci. Technol.* 63 (2003) 2353–2359.
- [13] P. Colombo, M. Modesti, Silicon oxycarbide ceramic foams from a preceramic polymer, *J. Am. Ceram. Soc.* 82 [3] (1999) 573–578.
- [14] H. X. Zhang, P. D. Nunes, M. Wilhelm, K. Rezwani, Hierarchically ordered micro/meso/macroporous polymer-derived ceramic monoliths fabricated by freeze casting, *J. Eur. Ceram. Soc.* 36 (2016) 51–58.
- [15] E. Volkmann, K. Tushtev, D. Koch, C. Wilhelmi, J. Göring, K. Rezwani, Assessment of three oxide/oxide ceramic matrix composites: Mechanical performance and effects of heat treatments, *Composites Part A*, 68 (2015) 19–28.
- [16] X. R. Ren, W. Pan, Mechanical properties of high-temperature-degraded yttria-stabilized zirconia, *Acta Mater.* 69 (2014) 397–406.
- [17] Q. Z. Chen, J. L. Xu, L. G. Yu, X. Y. Fang, K. A. Khor, Spark plasma sintering of sol-gel derived 45S5 Bioglass®-ceramics: Mechanical properties and biocompatibility evaluation, *Mater. Sci. Eng. C* 32 (2012) 494–502.
- [18] J. Seuba, S. Deville, C. Guizard, A. J. Stevenson, Mechanical properties and failure behavior of unidirectional porous Ceramics, *Sci. Rep.*, 6 [24326] (2016) 1–11.
- [19] A. Dey, N. Kayal, O. Chakrabarti, R. F. Caldato, M. D. de Mello Innocentini et al., Investigations on material and mechanical properties, air-permeation behaviour and filtration performance of mullite-bonded porous SiC ceramics, *Int. J. Appl. Ceram. Technol.* 11 [5] (2014) 804–816.
- [20] F. Ye, J. Y. Zhang, H. J. Zhang, L. M. Liu, Pore structure and mechanical properties in freeze cast porous  $\text{Si}_3\text{N}_4$  composites using polyacrylamide as an addition agent, *J. Alloys Compd.* 506 (2010) 423–427.
- [21] S. Meille, M. Lombardi, J. Chevalier, L. Montanaro, Mechanical properties of porous ceramics in compression: On the transition between elastic, brittle, and cellular behaviour, *J. Eur. Ceram. Soc.* 32 (2012) 3959–3967.
- [22] P. Colombo, J. R. Hellmann, D. L. Shelleman, Mechanical properties of silicon oxycarbide ceramic foams, *J. Am. Ceram. Soc.* 84 [10] (2001) 2245–2251.
- [23] G. A. Slack, Thermal conductivity of pure and impure silicon, silicon carbide, and diamond, *J. Appl. Phys.* 35 [12] (1964) 3460–3466.

- [24] X. Q. Cao , R. Vassen, D. Stoeber, Ceramic materials for thermal barrier coatings, *J. Eur. Ceram. Soc.* 24 (2004) 1–10.
- [25] J. H. Eom, Y. W. Kim, I. H. Song, H. D. Kim, Processing and properties of polysiloxane-derived porous silicon carbide ceramics using hollow microspheres as templates, *J. Eur. Ceram. Soc.* 28 [5] (2008) 1029–1035.
- [26] T. Fend, B. Hoffschmidt, R. Pitz-Paal, O. Reutter, P. Rietbrock, Porous materials as open volumetric solar receivers: Experimental determination of thermophysical and heat transfer properties, *Energy* 29 [5–6] (2004) 823–833.
- [27] P. Wan, Z. Wu, H. Zhang, L. Y. Gao, J. Y. Wang, Porous nano-SiC as thermal insulator: wisdom on balancing thermal stability, high strength and low thermal conductivity, *Mater. Res. Lett.* 4 [2] (2016) 104–111.
- [28] L. F. Hu, C. A. Wang, Y. Huang, Porous yttria-stabilized zirconia ceramics with ultra-low thermal conductivity, *J. Mater. Sci.* 45 [12] (2010) 3242–3246
- [29]. Z. Zivcová, E. Gregorová, W. Pabst, D. S. Smith, A. Michot et al., Thermal conductivity of porous alumina ceramics prepared using starch as a pore-forming agent, *J. Eur. Ceram. Soc.* 29 (2009) 347–353.
- [30] L. Qiu, Y. M. Li, X. H. Zheng, J. Zhu, D. W. Tang et al., Thermal-conductivity studies of macro-porous polymer-derived SiOC ceramics, *Int. J. Thermophys.* 35 (2014) 76–89.
- [31] J. K. Carson, S. J. Lovatt, D. J. Tanner, A.C. Cleland, Thermal conductivity bounds for isotropic, porous materials, *Int. J. Heat Mass Transfer* 48 (2005) 2150–2158.
- [32] D. S. Smith, A. Alzina, J. Bourret, B. Nait-Ali, F. Pennec et al., Thermal conductivity of porous materials, *J. Mater. Res.* 28 [17] (2013) 2260–2272.
- [33] K. E. Pappacena, K. T. Faber, H. Wang, W. D. Porter, Thermal conductivity of porous silicon carbide derived from wood precursors, *J. Am. Ceram. Soc.* 90 [9] (2007) 2855–2862
- [34] H. X. Zhang, C. B. Fidelis, A. L. Serva, M. Wilhelm, K. Rezwani, Water-based freeze casting: Adjusting hydrophobic polymethylsiloxane for obtaining hierarchically ordered porous SiOC, *J. Am. Ceram. Soc.* 100(2017)1907–1918.
- [35] H. M. Liu, D. Xu, P. Xu, R. J. Huang, X. D. Xu et al., Dismountable sample holder apparatus for rapid thermal conductivity measurements based on cryocooler, *AIP Conference Proceedings* 1434 (2012) 1363–1370.
- [36] M. Scheffler, T. Gambaryan-Roisman, T. Takahashi, J. Kaschta, H. Muenstedt et al., Pyrolytic decomposition of preceramic organo polysiloxanes, *Ceramic Transactions*, 115 (2002) 239–250.
- [37] A. Saha, R. Raj, D. L. Williamson, A Model for the Nanodomains in Polymer Derived SiCO, *J. Am. Ceram. Soc.* 89 (2006) 2188–2195.
- [38] S. Deville, E. Saiz , A. P. Tomsia, Ice-templated porous alumina structures, *Acta Mater.* 55 (2007) 1965–1974.
- [39] R. O. Ritchie, The conflicts between strength and toughness, *Nat. Mater.* 10 (2011) 817–822.
- [40] C. Kittel, Interpretation of the thermal conductivity of glasses, *Phys. Rev.* 75 [6] (1949) 972–974.

- [41] A. Gurlo, E. Ionescu, R. Riedel, D. R. Clarke, The thermal conductivity of polymer-derived amorphous Si–O–C compounds and nano-composites, *J. Am. Ceram. Soc.*, 99 [1] (2016) 281–285.
- [42] D. B. Marshall, M. R. Jarnes, J. R. Porter, Structural and mechanical property changes in toughened magnesia-partially-stabilized zirconia at low temperatures, *J. Am. Ceram. Soc.* 72 (1989) 218–227.
- [43] W.J. Xue, T. Ma, Z.P. Xie, J. Yi, Research into mechanical properties of reaction-bonded SiC composites at cryogenic temperatures, *Materials Letters* 65 (2011) 3348–3350.
- [44] W. W. Wu, J. Y. Gui, S. Wei, W. J. Xue, Z. P. Xie, Si<sub>3</sub>N<sub>4</sub>-SiC<sub>w</sub> composites as structural materials for cryogenic application, *J. Eur. Ceram.Soc.* 36 (2016) 2667–2672.
- [45] S. Wei, Z. P. Xie, W. J. Xue, J. Y. Gui, J. Chen, How does pore-induced crack change as temperatures decrease from 293 K to 77 K, *Ceram. Int.* 41 (2015) 15246–15249.
- [46] J. Tan, G. Wang, Z. Y. Liu, J. Bednarčík, Y. L. Gao et al., Correlation between atomic structure evolution and strength in a bulk metallic glass at cryogenic temperature, *Sci. Rep.* 4 [3897] (2014) 1–7.
- [47] F. C. Hull, S. K. Hwang, J. M. Wells, R. I. Jaffee, Effect of composition on thermal expansion of alloys used in power generation, *J. Mater. Eng.* 9 (1987) 81–92.
- [48] C. Dellacorte J. A. Fellenstein, The effect of compositional tailoring on the thermal expansion and tribological properties of PS300: A Solid lubricant composite coating, *Tribol. T.* 40 [4] (1997) 639–642.
- [49] G. K. White, Thermal expansion of reference materials: copper, silica and silicon, *J. Phys. D: Appl. Phys.*, 6 (1973) 2070–2078.
- [50] F. C. Marques, R. G. Lacerda, A. Champi, V. Stolojan, D. C. Cox et al., Thermal expansion coefficient of hydrogenated amorphous carbon, *Appl. Phys. Lett.* 83 (2003) 3099–3101.
- [51] S. Ghabezloo, Effect of porosity on the thermal expansion coefficient: A discussion of the paper ‘Effects of mineral admixtures on the thermal expansion properties of hardened cement paste’ y Z.H. Shui, R. Zhang, W. Chen, D. Xuan, *Constr. Build. Mater.* 24 (9) (2010) 1761–1767, *Constr. Build. Mater.* 24 (2010) 1796–1798.
- [52] G. M. Renlund, S. Prochazka, R. H. Doremus, Silicon oxycarbide glasses, 2. structure and properties. *J. Mater. Res.*, 6 (1991) 2723–2734.
- [53] T. Rouxel, G. Massouras, G. D. Sorarù, High temperature behavior of a gel-derived SiOC glass: elasticity and viscosity, *J. Sol-Gel Sci. Techn.*, 14 (1999) 87–94.
- [54] R. L. Coble, W. D. Kingery, Effect of porosity on physical properties of sintered alumina, *J. Am. Ceram. Soc.*, 39 (1956) 377–385.
- [55] N. Khalili, A. Uchaipichat, A. A. Javadi, Skeletal thermal expansion coefficient and thermo-hydro-mechanical constitutive relations for saturated homogeneous porous media, *Mechanics of Materials*, 42 (2010)593–598.
- [56] A. L. Sutton, V.C. Howard, The role of porosity in the accommodation of thermal expansion in graphite, *J. Nucl. Mater.* 7 (1962)58–71.
- [57] J. A. Kuszyk, R.C. Bradt, Influence of grain size on effects of thermal expansion anisotropy in MgTi<sub>2</sub>O<sub>5</sub>, *J. Am. Ceram. Soc.*, 56 (1973) 420–423.

- [58] Z. H. Karadeniz, D. Kumlutas, A numerical study on the coefficients of thermal expansion of fiber reinforced composite materials, *Compos. Struct.* 78 (2007) 1–10.
- [59] M. Nakata, K. Suganuma, Effect of internal structure on thermal properties of alumina/aluminum composites fabricated by gelate-freezing and partial-sintering process, respectively, *Mater. Trans.* 46 (2005) 130–135.
- [60] E. H. Kerner, The elastic and thermo-elastic properties of composite media, *Proc. Phys. Soc. B* 69 (1956) 808–813.
- [61] R. A. Schapery, Thermal expansion coefficients of composite materials based on energy principles, *J. Comp. Mater.* 2 (1968) 380–404.
- [62] H. Nakajima, Fabrication, properties and application of porous metals with directional pores, *Prog. Mater. Sci.*, 52 (2007) 1091–1173.
- [63] R. C. Zeller, R. O. Pohl, Thermal conductivity and specific heat of noncrystalline solids, *Phys. Rev. B* 4 (1971) 2029–2041.
- [64] K. M. Kim, S. H. Jang, Y. W. Kim, W. S. Seo, Thermal and mechanical properties of SiC–TiC<sub>0.5</sub>N<sub>0.5</sub> composites, *J. Am. Ceram. Soc.* 98 [2] (2015) 616–623.
- [65] I. H. Tavman, Effective thermal conductivity of granular porous materials, *Int. Comm. Heat Mass Transfer* 23 (1996) 169–176.
- [66] R. Landauer, The electrical resistance of binary metallic mixtures, *J. Appl. Phys.* 23 (1952) 779–784.
- [67] J. F. Wang, J. K. Carson, M. F. North, D. J. Cleland, A new approach to modelling the effective thermal conductivity of heterogeneous materials, *Int. J. Heat Mass Transfer* 49 (2006) 3075–3083.
- [68] H. W. Russell, Principles of heat flow in porous insulators, *J. Am. Ceram. Soc.* 18 (1935) 1–5.
- [69] C. Ferraro, E. Garcia-Tuñon, V. G. Rocha, S. Barg, M. D. Fariñas et al., Light and strong SiC networks, *Adv. Funct. Mater.* 26 (2016) 1636–1645.
- [70] Y. Grebenyuk, H. X. Zhang, M. Wilhelm, K. Rezwan, M. E. Dreyer, Wicking into porous polymer-derived ceramic monoliths fabricated by freeze casting, *J. Eur. Ceram. Soc.* 37 (2016) 1993–2000.
- [71] B. Weisenseel, P. Greil, T. Fey, Biomorphous silicon carbide as novel loop heat pipe wicks, *Adv. Eng. Mater.* 19 (2016) 1600379 (1–9).



## 8. Conclusions

### Crack free macroporous monolith

Crackfree porous polymer-derived ceramic monoliths of large size have been fabricated by a suspension based freeze casting process, using water as solvent and polysiloxane-based fillers as the solid phase. Small pore sizes and high permeability allows for large capillary pumping capacity, which is advantageous for cryogenic wicking.

Pore generating method (freeze casting), fillers (partially pyrolyzed polymers) and solid loading, all these factors contributed to the manufacturing of crackfree monoliths. Freeze casting created a macroporous structure before the preceramic polymers (and hybrid fillers) were pyrolyzed, which reduced the cracks formed during the gas evolution and shrinkage. The use of fillers as solid phase in freeze casting process, reduced the shrinkage of polymer derived ceramic monoliths, and increased the thermal shock resistance of the green monoliths, when they were taken out from -150 °C. To avoid inhomogeneity of final monolith and cracks formation inside green bodies (caused by the great volume change between ice and water phase transition), moderate solid loadings (30–40 wt%) were found to be optimal. Unidirectional freeze casting created permeability as high as  $3.5 \times 10^{-9} \text{ m}^2$ , which is very advantageous for wicking and other mass transport processes.

The idea of modifying the surface of polysiloxanes by different ways for water-based freeze casting renders it possible to use other hydrophobic siloxanes in water-based processes other than freeze casting. The surface characteristics of the polysiloxane precursors used in this work are hydrophobic. It was shown that the surface of the polysiloxanes can be modified greatly by thermal decomposition or compositing with hydrophilic monomer (APTES). Thermal decomposition removed the hydrophobic groups (phenyl group) of H44 to make the filler more hydrophilic, while compositing method introduced the hydrophilic groups to MK to make it more hydrophilic.

The combination of polymer derived fillers with freeze casting resulted in hierarchically-ordered porous structure with a relatively high SSA. Pyrolysis of preceramic polymers at lower temperature (e.g. 600 °C) produced fillers with micropores. Therefore, using fillers in freeze casting process produced a micro/macroporous structure. The use of silica sol (binder) resulted in further formation of mesopores (pore size 2–10 nm). The macropore sizes can be altered with different freezing temperatures from a few up to tens of microns, while the micro/mesopore amounts can be controlled by pyrolysis temperature. Therefore, monoliths with micro/meso/macropores, meso/macropores or just macropores can be fabricated depending on preparation conditions.

The hydrophilicity of the final monolith can be adjusted by both pyrolysis temperatures and the ratios between solid and silica sol. The hierarchically ordered porous structure with adjustable

surface characteristics, allows for the specific design of porous structure for specific applications, such as gas separation and liquid filtration.

### **Thermal and mechanical properties at cryogenic temperatures**

Thermal and mechanical properties of anisotropic porous SiOC ceramic at cryogenic temperatures were first investigated in this work, which provided important information for further investigation of cryogenic wicking and other possible cryogenic applications. The influence of both cryogenic temperatures and cryogenic liquids on the compressive strength was investigated.

The compressive strength of such porous ceramics differed greatly in air (~273 K) and in liquid nitrogen (77 K) due to two factors. The liquid trapped inside the porous structure increased the resistance during compression test, and the cryogenic temperature itself also increased the compressive strength. This also means that the mechanical strength of the porous ceramics is stronger during cryogenic wicking than at room temperature.

Different precursors were investigated concerning their mechanical and thermal properties. It showed that the compressive strength of SiOC ceramics prepared by suspension based freeze casting was mainly influenced by porosity, and slightly influenced by composition. The thermal conductivity of the as obtained SiOC ceramics is very low, turning it into potential materials for thermal isolation. Unlike compressive strength, thermal properties were influenced by the compositions (precursors). Additionally, the measurement conditions (drained/undrained conditions) were found to influence linear coefficients of thermal expansion. The investigation of CTEs at cryogenic temperature proved that, the measurement conditions should be carefully controlled to exclude the influence of moisture. At the same time it was demonstrated that Schapery equation can be used to calculate the CTEs of anisotropic porous materials in pore longitudinal and transverse directions.

This work also showed that engineering high porosity into amorphous SiOC ceramics was a useful strategy to produce low thermal conductivity materials. The thermal conductivity of such materials makes them less sensitive to the temperature change and reduces the heat loss in cryogenic applications. Furthermore, this work demonstrated the possibility of calculating thermal conductivity of the hierarchically ordered porous structure by available theory models. The maximum heat conductivity can be calculated based on series and parallel model and EMT model. Although the unknown composition of silica and carbon nanodomains in the final monolith made the calculation of thermal conductivity very difficult, the maximum heat conductivity was determined mainly by the macroporosity and the thermal conductivity of SiOC.

In short, modifying the surface of polysiloxanes for water-based freeze casting process broads fabrication techniques to produce macroporous PDCs. This preparation process also makes hierarchically ordered porous structure easy to produce. The thermal properties of as obtained anisotropic porous ceramics can be predicted by theoretical models. The thermal and

## 8. Conclusions

---

mechanical properties obtained in this work point out key questions and bring up potential solutions for further investigation of cryogenic wicking and other possible cryogenic applications.

## 9. Outlook

Macroporous PDCs monoliths prepared in this work were investigated for isothermal wicking at room temperature, however, not at cryogenic temperatures. Cryogenic wicking requires porous medium to survive very strict pretreatments and critical working conditions. Therefore, the properties, especially mechanical properties need to be further improved for cryogenic wicking. The mechanical strength of prepared monoliths can be manipulated during suspension based freeze casting and pyrolysis process.

In this work, filler materials were prepared by pyrolysis at low temperatures (600 °C) with either MK or H44. Great decomposition at 600 °C means limited reactive groups on the fillers, which led to weak necks between fillers particles during the second pyrolysis, even at 1000 °C. The defects were inside the lamellar walls, which lowered the mechanical strength (less than 10 MPa). One possible way to solve this problem is to prepare fillers at low pyrolysis temperatures (eg. 400 °C), so that the bonding strength between the filler particles during the second pyrolysis can be improved, which improves mechanical strength. However, low pyrolysis temperatures leads to more hydrophobic surface. Therefore, the surface tension of the water should be modified (such as adding additives, etc.) to allow fillers to be better wetted in water solution. The filler particles sizes also influenced the defects formation. Large particle sizes and the broad distribution created defects in the lamellar walls, which deteriorated the mechanical properties. Better ways of milling (grinding) need to be found to get finer particles, which make particles packing tighter during freezing. The mesopores formed inside the structure also deteriorate the mechanical strength. Polysiloxanes cross-link in organic solvents without adding binders in freeze casting can avoid mesopores formation; meanwhile fillers can be added to limit the shrinkage.

The isothermal wicking of porous PDCs with radial lamellar pores at room temperature was investigated. The next interesting step is to investigate the wicking performance of unidirectional porous structure which has a higher permeability, especially at cryogenic temperatures. Anisotropic pores (lamellar pores) in this work were created by putting mold containing the slurry inside a freezer. The temperature gradient was directed by the configuration of the mold, which comprised of either pure aluminum (radial lamellar pores) or PVC and aluminum (unidirectional lamellar pores). The alignment of the porous structure was parallel to temperature gradients (freezing directions). However, the configuration of PVC and aluminum mold was not able to create lamellar pores which were perfectly aligned, resulting in relatively weaker compressive strength and high standard deviations. The relatively weaker mechanical strength restricted its use for cryogenic wicking and further practical use. One possible solution is to improve the pore alignment by controlling the temperature gradient more delicately using unidirectional freezing devices.

Another interesting aspect of cryogenic wicking is to compare mechanical, thermal properties and wicking performance of anisotropic lamellar porous ceramics with isotropic spherical porous ceramics prepared by other techniques, such as direct foaming or sacrificial templating method.

Besides cryogenic wicking, the monoliths prepared by freeze casting method are also potential for other mass transport applications due to their high permeability. The micro/meso/macroporous structure prepared at low pyrolysis temperature which has a high specific surface area ( $> 200 \text{ m}^2/\text{g}$ ) can be used for catalyst supports. Especially compositing polysiloxanes with APTES can make metal catalysts distribution more homogenous.

Another point worth further developing is preceramic polymers derived fillers. In the literature, hydrophilic oxide ceramic powders (eg. alumina) have been modified with short chain amphiphile, forming partially hydrophilic and partially hydrophobic surface, which can stabilize bubbles and form ultra-stable foams. It was observed that by modifying surface of preceramic polymers to partially hydrophilic and hydrophobic (eg. 1MK-1APTES-200 fillers), those fillers can work like a solid 'surfactant', which can stabilize bubbles in water as well. Therefore, introducing air by stirring before freeze casting of amphiphilic fillers creates additional cellular structure and improves the porosity greatly. Notably, the stability of the foams is greatly influenced by the filler particle sizes. To get ultrastable foams, the fillers of nanometer size should be used; therefore a better milling technique is needed.

## Appendix

### A.1 Additional figures for chapter 5:

#### Hierarchically ordered micro/meso/macroporous polymer derived ceramic monoliths fabricated by freeze-casting

Figure A1 shows the crystallinity of the samples after pyrolysis at 1000 °C. No sharp peaks were observed, only a peak around 20–25°, which is typical for amorphous materials. This may explain the weaker mechanical strength. At higher pyrolysis temperature, SiC formed which normally has high mechanical strength.

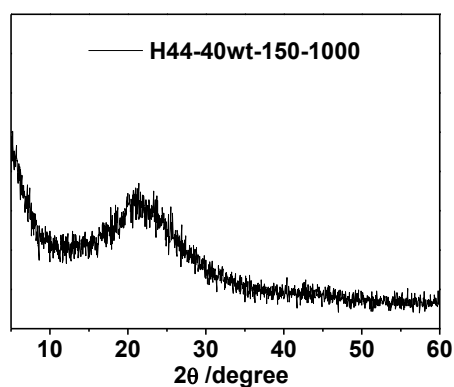


Figure A1: X-ray diffraction (XRD) pattern of sample H44-40wt-150-1000.

The hydrophilicity of surface characteristics determines if the fillers can be well dispersed in water (silica sol). The ratio between water and heptane adsorption can reflect the hydrophilicity/hydrophobicity of the surface. When water adsorption is higher, the material is more hydrophilic.

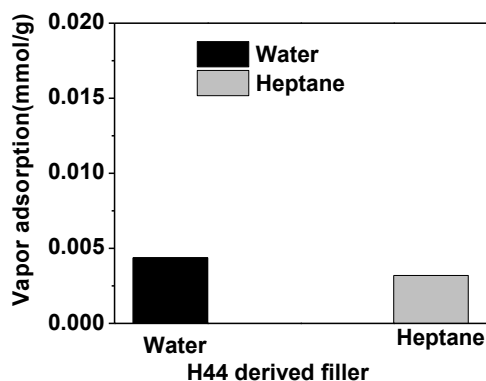


Figure A2: The water and *n*-heptane vapor adsorption at 25 °C for H44-derived filler obtained by pyrolyzing cross-linked H44 at 600 °C. The sorption data were recalculated using the specific BET surface area ( $509 \text{ m}^2 \cdot \text{g}^{-1}$ ) from  $\text{N}_2$  adsorption.

H44-derived filler was obtained by pyrolyzing H44 at 600 °C, therefore there is no obvious weight loss up to 1000 °C. The relative weight loss difference of  $\pm 1\%$  can be regarded as measurement error.

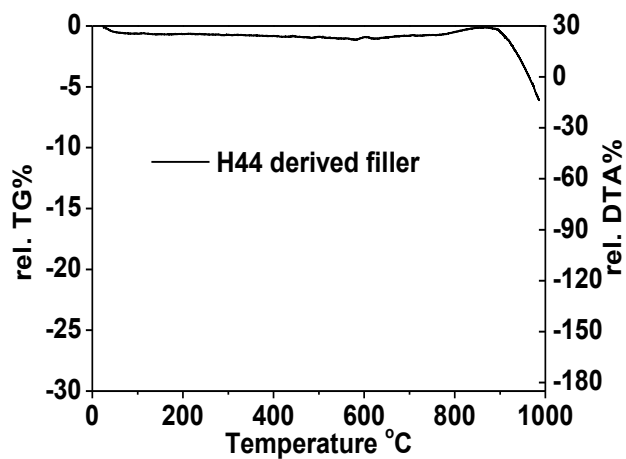


Figure A3: Thermal gravimetric analysis (TGA) of H44-derived filler obtained by pyrolyzing cross-linked H44 at 600 °C in nitrogen.

## A2. Additional figures for chapter 6:

### Water-based freeze casting: Adjusting hydrophobic methyl polysiloxane for obtaining hierarchically ordered porous SiOC

The hydrophilicity of the fillers prepared with different precursors is shown in Figure A4. H44-derived filler (H44-600) showed higher water adsorption than heptane, having a hydrophilic surface. However, MK derived filler prepared with the same procedure (MK-600) was still hydrophobic and can therefore not directly applied in the water-based freeze casting.

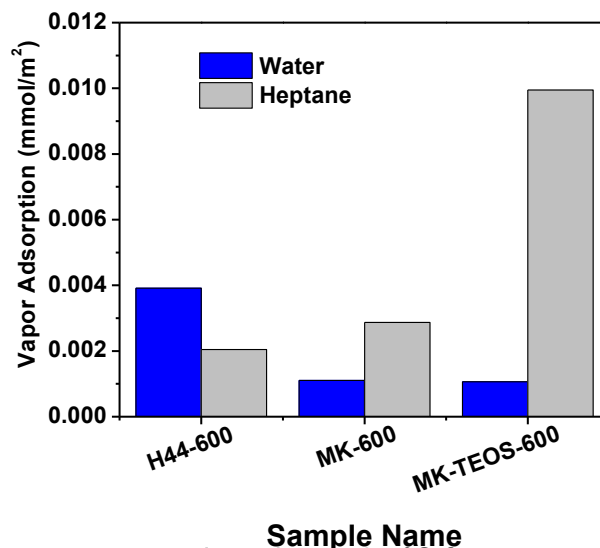


Figure A4: Water and *n*-heptane vapor adsorption at 25 °C for precursors pyrolyzed at 600 °C. The sorption data were recalculated using the specific BET surface area from N<sub>2</sub> adsorption.

Figure A5 shows that MK-APTES-200 cannot disperse well directly in water due to the limited hydrophilicity even after vigorous stirring. Therefore, the hydrophilicity needs to be improved by further pyrolysis of 600 °C.



Figure A5: Slurry prepared with MK-APTES-200 in water.



Despite of the limited dispersion of MK-APTES-200 in water, the freeze casting samples still showed similar structure as MK-APTES-600. Figure A6 shows the cross-section of the lamellae and their perpendicular direction, in which the bridges formed between lamellae.

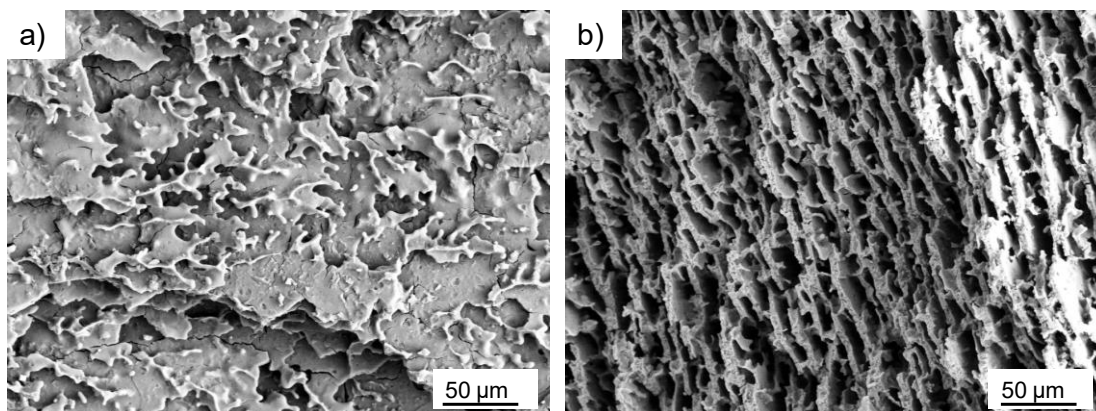


Figure A6: SEM images of pyrolyzed monoliths prepared with MK-APTES-200 a) Cross-section parallel to the lamellar pores, b-c) cross sections perpendicular to the lamellar pores.

The isotherms of MK-APTES-200-600 and MK-APTES-200-1000 (in Chapter 6) were compared in Figure A7. As the same with MK-APTES-600-600, the mesopores in MK-APTES-200-600 are also created due to the silica sol as the binder. However, the sample pyrolyzed at higher temperature, MK-APTES-200-1000, has no mesopores, which is quite different from MK-APTES-600-1000 (in Chapter 6) still having high amounts of mesopores. This can be explained by the high amounts of reactive groups on the surface of MK-APTES-200 fillers before pyrolysis.

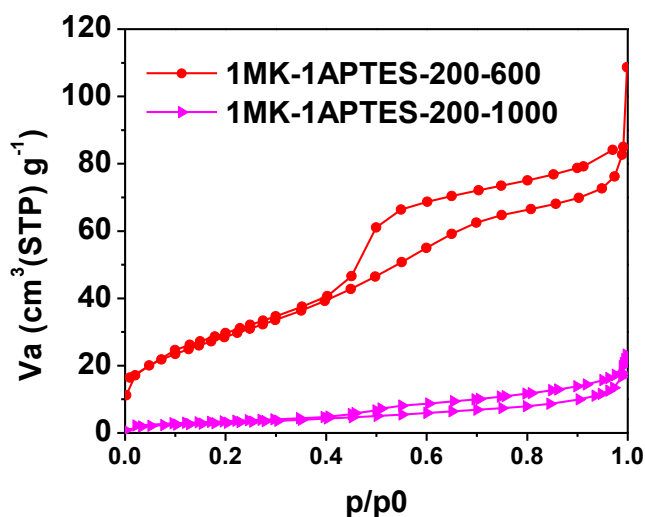


Figure A7: Nitrogen adsorption and desorption of monoliths prepared with MK-APTES-200 pyrolyzed at 600 and 1000 °C.

### A3. Additional figures for chapter 7:

#### Macro/mesoporous SiOC ceramics of anisotropic structure for cryogenic engineering

Figure A8 showed the mold used for unidirectional freezing. Due to the high conductivity of aluminium plates, the heat conduction in it is much faster than in the PVC material (Temperature gradient indicated by the white arrows).

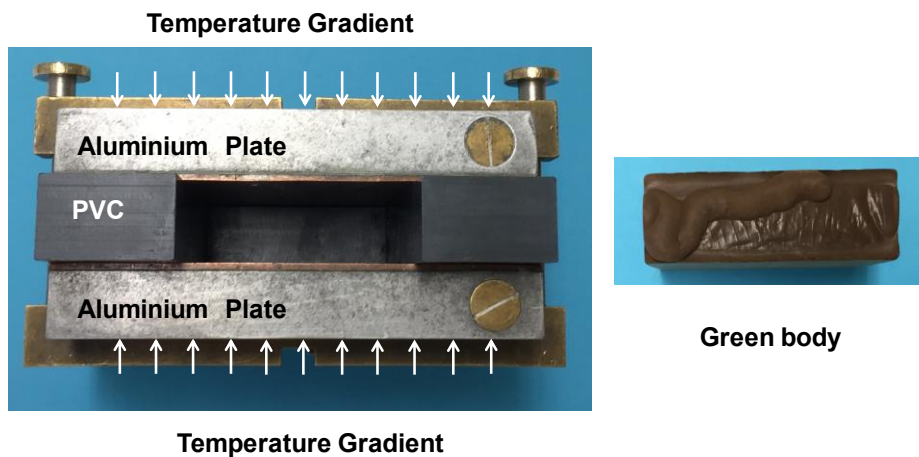


Figure A8: The configuration of the mold for unidirectional freezing.

Figure A9 shows BJH plot of SiOC ceramics made from H44 or MK and APTES. Both monoliths have mesopores size ranged from 2 nm to 20 nm.

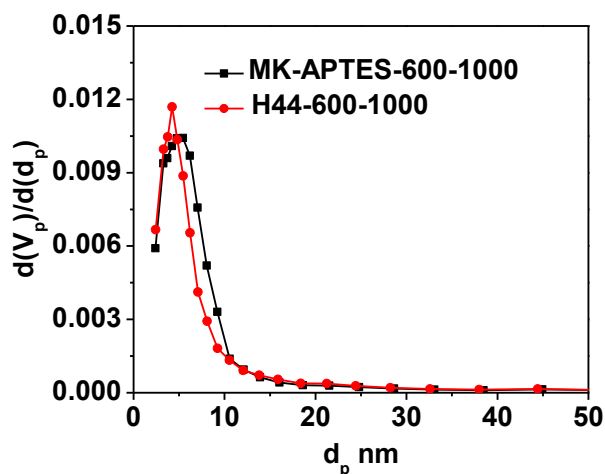


Figure A9: The BJH plots of monoliths prepared with H44 or MK and APTES.

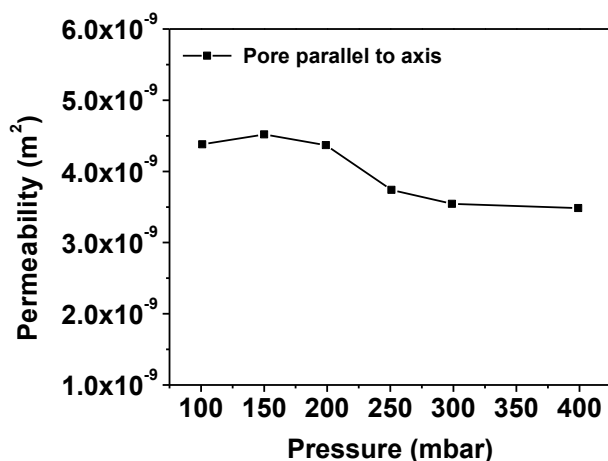


Figure A10: Permeability of monolith (pore perpendicular to monolith axis) measured by falling head permeability test at varied pressure. The pressure was varied by air pressure applied above the water surface. The higher value of permeability at lower pressure was due to the higher errors resulting from the hydrostatic pressure of water. The permeability measured at pressure higher than 250 mbar was considered as accurate. The permeability was calculated as per Darcy's law.

The higher compressive strength in solvents than in air may be due to liquids trapped inside the pores, and the strength also varies with solvents. The compressive strength in liquid nitrogen and dry ice and ethanol are higher than at room temperature. The low temperature decreases the distance between atoms, therefore the interactions between atoms become stronger, which improved the compressive strength.

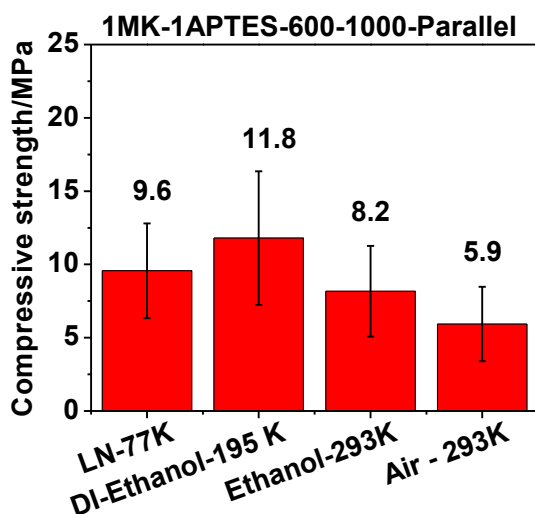


Figure A11: Compressive strength of 1MK-1APTES-600-1000 of 'parallel' monoliths in liquid nitrogen (77 K), dry ice-ethanol bath (195 K), ethanol bath (293 K) and air (293 K).

Moisture inside pores can form ice during the compression test in liquid nitrogen or dry ice bath, and increase the compressive strength. The TGA analysis in Figure A12 showed the low amount of adsorbed water on the sample. The weight increased was around 5% when it was exposed to air for 1 day. Therefore, there will be little ice formed inside pores.

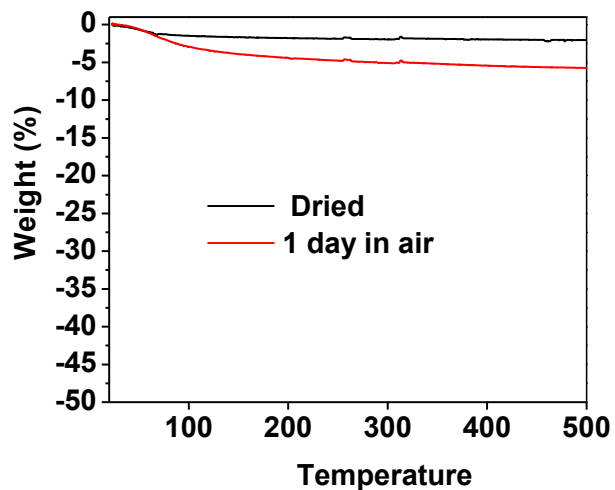


Figure A12: Thermogravimetric analysis of MK-APTES-600-1000 measured after immediate drying and 1 day exposure to air.

#### A.4 Wicking experiments of porous PDC monoliths under isothermal condition

Adapted with permission from Elsevier, license number: 4185901403990, from the joint article 'Wicking into porous polymer-derived ceramic monoliths fabricated by freeze-casting' Y. Grebenyuk, H. X. Zhang, M. Wilhelm, K. Rezwan, M. E. Dreyer, published in *J. Eur. Ceram. Soc.* 37 (2017)1993–2000.

The samples were prepared following the procedure described in Chapter 5. Wicking experiments were performed on two sets of samples, prepared at two different freezing temperatures ( $-80$  and  $-150$  °C). The samples prepared at the freezing temperature of  $-80$  °C are referred as to 80-1 and 80-2, while the samples prepared at  $-150$  °C as to 150-1 and 150-2. The porous structure and the geometrical characteristics of the samples are presented in Figure A13.

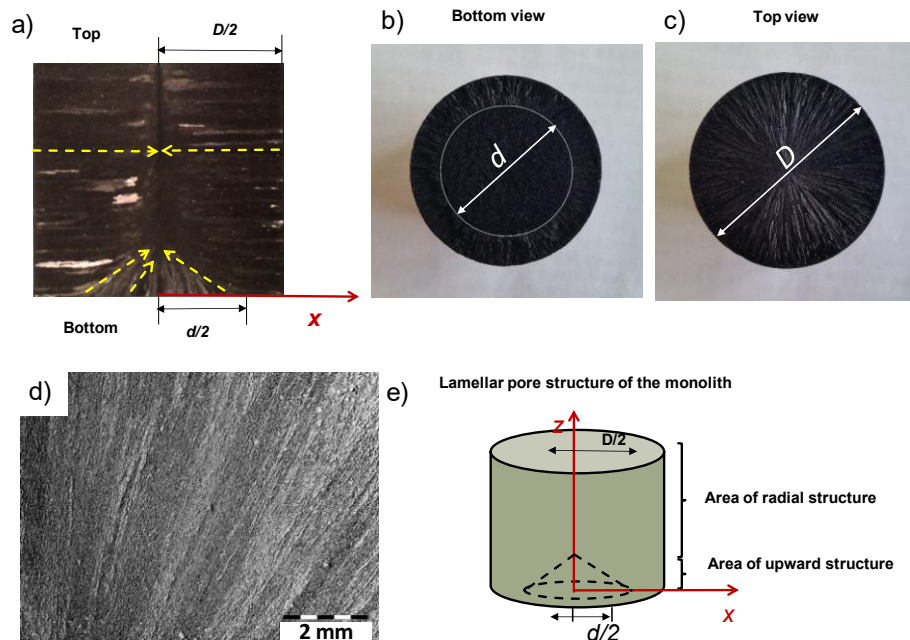


Figure A13: (a) The side view of the longitudinal cross-section of the monolith. The yellow dash lines indicated the directions of the lamellar pores; (b) the bottom view of the monolith; (c) the top view of the monolith; (d) the SEM of the transverse cross-section at the top; and (e) the scheme of the anisotropic structure.  $D$  and  $L$  are referred as to the overall diameter and length of the cylindrical monolith, respectively.  $d$  is referred as to the diameter of the cone area with upward oriented pores that is visible from the bottom of the monolith.

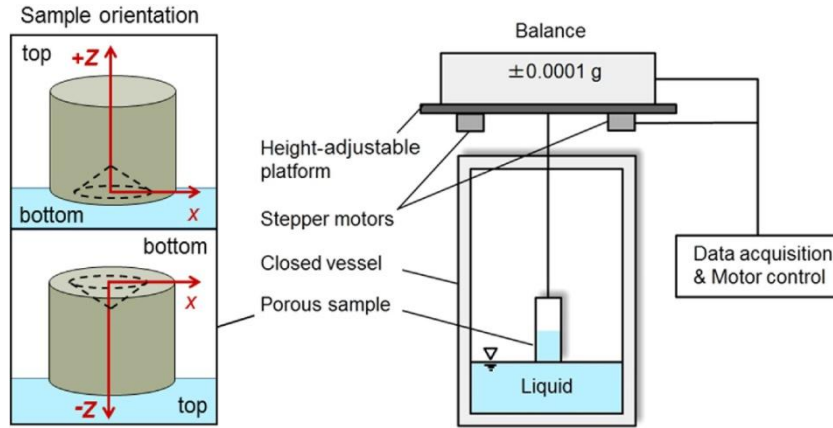


Figure A14: The schematic image of the setup for wicking experiments. Each sample was tested using “bottom to top” and “top to bottom” orientation to the liquid surface. These orientations are referred as to +z and -z, respectively.

Figure A14 shows a schematic image of the setup for the wicking experiments. The weight of a porous sample was measured using an electronic high precision balance (LA 310S-OCE, Sartorius) with an accuracy of  $\pm 0.0001$  g. The balance was fixed on a height-adjustable platform driven by two stepper motors (VRDM566/50, Berger Lahr/Schneider Electric) with a velocity of 0.38 mm/s. The sample was placed in a closed vessel of 0.095 m diameter partly filled with FC-72 liquid supplied by 3M Fluorinet<sup>TM</sup>. Some thermophysical properties of FC-72 liquid are listed in Table A1. The contact angle with regard to the experimental samples was taken as zero due to perfect wetting characteristics of the FC-72 test liquid. The tests were performed at room temperature and normal pressure. In order to initiate the wicking, a vertically oriented porous sample was submerged into the bulk liquid by a depth of approximately 3 mm. The liquid imbibed into the unsaturated (not submerged) part of the sample. The imbibition caused a sample weight increase that was recorded with a sampling rate of 20 Hz. A constant sample weight at the end of the imbibition indicated complete saturation of the sample. To finish the experiment the sample was driven approximately 6 mm upwards and, thus, detached from the liquid surface. To study the impact of the anisotropy on the wicking process each sample was tested using “bottom to top” and “top to bottom” orientation to the liquid surface, see Figure A14. In the following, we refer to these orientations as to +z and -z, respectively.

Table A1: Density  $\rho_L$ , dynamic viscosity  $\mu_L$  and surface tension  $\sigma_s$  of FC-72 liquid at 101,325 Pa and 298.15 K.

$\rho_L$ (kg·m <sup>-3</sup> )	$\mu_L$ (Pa·s) 10 <sup>-6</sup>	$\sigma_s$ (N·m <sup>-1</sup> ) 10 <sup>-3</sup>
1690	709.8	12

A viscous-dominated stage of the imbibition into porous media is described by the Lucas–Washburn equation (A1.1).

$$\frac{2\sigma_s \cos \theta}{R_s} = \frac{p\mu_L \dot{h}h}{K} \quad (A1.1)$$

where  $h$  is the wicking height,  $\rho_L$  and  $\mu_L$  are the surface tension and the dynamic viscosity of liquid, respectively,  $\theta$  is the contact angle and  $R_s$  the static pore radius of a porous structure. The wicking height  $h$  can be recalculated into the mass of imbibed liquid using equation (A1.2)

$$m(t) = \rho_L p A h(t) \quad (A1.2)$$

where  $A$  is the cross-section area of a sample. Rearranging equations (A1.1) and (A1.2), one obtains (A1.3), which can be used to calculate permeability.

$$\frac{m^2}{t} = \frac{4\sigma_s \cos \theta \rho_L^2 A^2 p}{\mu_L R_s} K \quad (A1.3)$$

The static pore radius  $R_s$  indicates the characteristic pore size of porous media determined using the wicking height  $h_{eq}$  at the equilibrium between the capillary and hydrostatic pressures. The equilibrium height for the imbibition with the FC-72 liquid was estimated by equation (A1.4).

$$\frac{2\sigma_s \cos \theta}{R_s} = \rho_L g h_{eq} \quad (A1.4)$$

Where  $g$  is the gravity constant, and  $h_{eq}$  was approximately 0.174 m and 0.923 m for the samples prepared at the freezing temperature of  $-80$  °C and  $-150$  °C, respectively. Due to the sample size limitation it was not possible to achieve such wicking heights experimentally. For permeability calculations, the volume-weighted characteristic pore size  $R_{av}$  obtained via the mercury intrusion porosimetry was used. The geometrical characteristics and macroscopic parameters for permeability calculation and modeling are listed in Table A2.

Table A2: Geometrical characteristics and macroscopic parameters of the porous samples.

Sample	$D$ (m) $10^{-3}$	$d$ (m) $10^{-3}$	$d/D$	$L$ (m) $10^{-3}$	$R_{av}$ (m)	$p_{merc}$	$p_{imb}$	$K_{-z}$ (m <sup>2</sup> ) $10^{-14}$	$K_{+z}$ (m <sup>2</sup> ) $10^{-14}$
80-1	30	21	0.70	42	8.35	0.532	0.466	4.43±0.10	3.65±0.12
80-2	30	19	0.63	42	8.35	0.532	0.471	5.00±0.22	4.48±0.12
150-1	30	21	0.70	42	1.57	0.548	0.516	0.265±0.003	0.177±0.002
150-2	30	15	0.50	42	1.57	0.548	0.516	0.368±0.007	0.336±0.002

$p_{merc}$  is the porosity determined by mercury intrusion porosimetry and  $p_{imb}$  is the porosity calculated using the results of the weight measurements of dry samples and samples completely saturated with FC-72 liquid by equation (A1.5).

$$p_{imb} = \frac{V_{void}}{V_{total}} = \frac{m_L/\rho_L}{V_{total}} \quad (A1.5)$$

where  $V_{total}$  is the total volume of a sample,  $V_{void}$  is the void volume of a sample that includes only the volume of interconnected pores, and  $\rho_L$  is the density of the liquid. The porosity value of  $p_{merc}$  and  $p_{imb}$  obtained using two different methods are in good agreement. However,  $p_{imb}$  was used for permeability calculations, which is a volume-averaged value of the open porosity determined for the whole structure. This is of importance for the macroscopic modeling of the wicking process. Permeability  $K_{-z}$  and  $K_{+z}$  determined from imbibition experiments at  $-z$  and  $+z$  sample orientations are shown with a standard deviation for four test runs.

Figure A15 shows wicking results for the sample 80-1, 80-2, 150-1 and 150-2 in terms of the squared mass of the imbibed FC-72 liquid plotted versus time. The imbibition rates differs for the samples and for  $+z$  and  $-z$  orientations of each sample. Equation (A1.3) was fitted to experimental data up 10% of the equilibrium wicking height for each sample. The equilibrium wicking height corresponds to the equilibrium wicking mass. The horizontal solid line with the inscription  $0.01 m_{eq}^2$  is referred to the squared value of 10% of the equilibrium wicking mass for the samples 80-1 and 80-2. For the samples 150-1 and 150-2 the equilibrium wicking height exceeded the sample length, therefore, equation (A1.3) was fitted to the whole range of the experimental data.

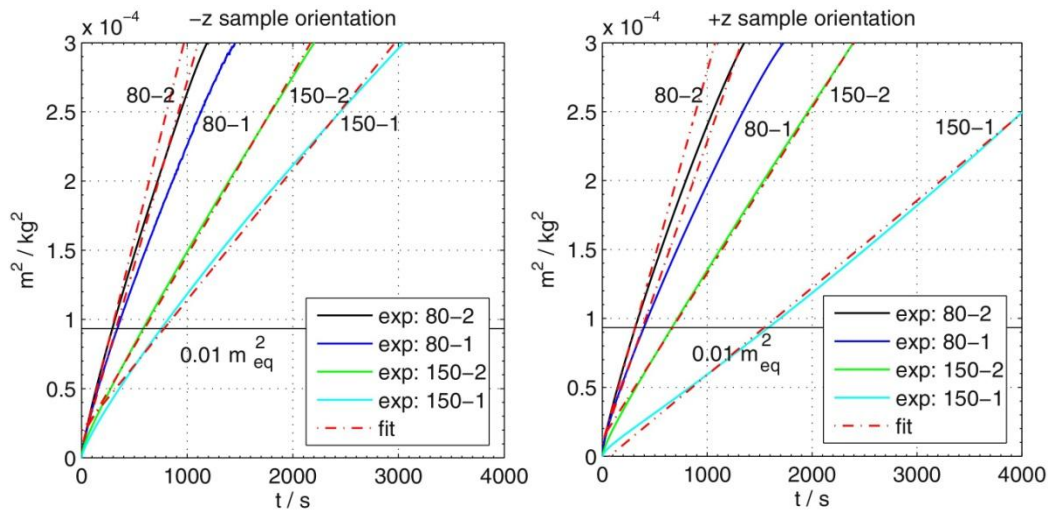


Figure A15: The squared mass of the imbibed FC-72 liquid into the samples 80-1, 80-2, 150-1 and 150-2 versus time.



## A5. Author contributions for the publications presented in this work

### Publication presented in chapter 5

*H. X. Zhang, P. D'A. Nunes, M. Wilhelm, K. Rezwan, Hierarchically ordered micro/meso/macroporous polymer derived ceramic monoliths fabricated by freeze-casting, J. Eur. Ceram. Soc. 36 (2016) 51–58. DOI: 10.1016/j.jeurceramsoc.2015.09.018*

Author	Contribution
Huixing Zhang	Concept and planning of work, fabrication of samples, samples preparation for characterizations, nitrogen adsorption/desorption measurements, SEM, zeta potential measurement, vapor adsorption measurements, data analysis and interpretation, manuscript preparation (design, editing, writing)
Pedro D'Angelo Nunes	Fabrication of samples, samples preparation for characterizations, nitrogen adsorption/desorption measurements, vapor adsorption measurements, data analysis
Michaela Wilhelm	Gave scientific input and conceptual advice, discussed data, edited manuscript
Kuroschi Rezwan	Gave scientific input and conceptual advice, discussed data, edited manuscript

### Publication presented in chapter 6

*H. X. Zhang, C. L. Fidelis, A. L. T. Serva, M. Wilhelm, K. Rezwan, Water-based freeze casting: Adjusting hydrophobic polymethylsiloxane for obtaining hierarchically ordered porous SiOC, J. Am. Ceram. Soc. 100 (2017) 1907–1918. DOI: 10.1111/jace.14782*

Author	Contribution
Huixing Zhang	Concept and planning of work, fabrication of samples, samples preparation for characterizations, thermogravimetric analysis, nitrogen adsorption/desorption measurements, SEM, zeta potential measurement, vapor adsorption measurements, data analysis and interpretation, manuscript preparation (design, editing, writing)
Clara Lana Fidelis	Fabrication of samples, samples preparation for characterizations, thermogravimetric analysis, nitrogen adsorption/desorption measurements, vapor adsorption measurements, data analysis
Ana Luiza Teixeira Serva	Fabrication of samples, samples preparation for characterizations, nitrogen adsorption/desorption measurements, zeta potential measurement,

	thermogravimetric analysis, vapor adsorption measurements
Michaela Wilhelm	Gave scientific input and conceptual advice, discussed data, edited manuscript
Kurosch Rezwan	Gave scientific input and conceptual advice, discussed data, edited manuscript

### Publication presented in chapter 7

*H. X. Zhang, C. L. Fedelis, M. Wilhelm, Z. P. Xie and K. Rezwan, Macro/mesoporous SiOC ceramics of anisotropic structure for cryogenic engineering, Mater. Design, 134 (2017) 207–217 DOI: 10.1016/j.matdes.2017.08.039*

Authors	Contribution
Huixing Zhang	Concept and planning of work, fabrication of samples, prepare samples for characterizations, thermogravimetric analysis, Hg intrusion porosimetry, SEM, compression tests, thermal expansion measurement, thermal conductivity measurement, data analysis and interpretation, manuscript preparation (design, editing, writing)
Clara Lana Fidelis	Fabrication of samples, samples preparation for characterizations, compression tests, data analysis
Michaela Wilhelm	Gave scientific input and conceptual advice, discussed data, edited manuscript
Zhipeng Xie	Gave conceptual advice, discussed data
Kurosch Rezwan	Gave scientific input and conceptual advice, discussed data, edited manuscript

## **A6. Betreute studentische Arbeiten / Supervised work of student**

In der vorliegenden Arbeit sind Ergebnisse enthalten, die im Rahmen der Betreuung folgender studentischer Arbeiten entstanden sind.

### **A6.1 Betreute Diplomarbeiten/Supervised diploma thesis:**

- Pedro D'Angelo Nunes, Fabrication of micro/meso/macroporous polymer derived ceramic monoliths by freeze casting method, 1<sup>st</sup> Oct. 2014–20<sup>th</sup> Apr.2015
- Clara Lana Fidelis, Thermal and mechanical properties of macroporous SiOC ceramics prepared by freeze casting method, 23<sup>rd</sup> Mar. 2015–8<sup>th</sup> Feb. 2016

### **A6.2 Betreute studentische Projekte /Supervised work of students:**

Ana Luiza Teixeira Serva, Functionalization of polysiloxane with (3-Aminopropyl)triethoxysilane to produce monolith ceramic using water-based freeze casting, 9<sup>th</sup> Jun. 2015 –1<sup>st</sup> Feb. 2016

## A7. Curriculum Vitae

**Surname** Zhang  
**First name** Huixing  
**Date of birth** 08.02.1988  
**Place of birth** Linyi, Shandong, China

### Work Experience and Education

10/ 2013– present Ph.D student, Advanced Ceramics Institute, University of Bremen, Germany  
Doctor Thesis: Macroporous polymer-derived ceramic monoliths for cryogenic applications manufactured by water-based freeze casting

11/2015–01/2016 Visiting researcher, Tsinghua University, China

03/2013–09/2013 Research secretary, Technical Institute of Physics and Chemistry  
Chinese Academy of Science, China

09/2009–01/2013 Master of Science, Material Chemistry, Fuzhou University, China  
Master Thesis: Micro-nanostructured molybdenum oxides: synthesis and electrochemical properties

01/2012–08/2012 Internship, Australian Institute for Bioengineering and Nanotechnology,  
University of Queensland, Australia  
Project: Synthesis of AFI structured microporous materials, SBA-15 mesoporous materials and its electrochemical applications

09/2005–07/2009 Bachelor of Science, Chemistry, Shandong Normal University, China  
Bachelor Thesis: The study of adsorption of oxygen on copper surfaces by computing chemistry

## **A8. List of publications and conferences contribution:**

### **A8.1 Peer reviewed articles prepared within the frame work of this thesis:**

H. X. Zhang, P. D'A. Nunes, M. Wilhelm, K. Rezwan, Hierarchically ordered micro/meso/macroporous polymer derived ceramic monoliths fabricated by freeze-casting, J. Eur. Ceram. Soc. 36 (2016) 51–58.

<http://www.sciencedirect.com/science/article/pii/S0955221915301370>

H. X. Zhang, C. L. Fidelis, A.L. T. Serva, M. Wilhelm, K. Rezwan, Water-based freeze casting: Adjusting hydrophobic polymethylsiloxane for obtaining hierarchically ordered porous SiOC, J. Am. Ceram. Soc. 100 (2017) 1907–1918.

<http://onlinelibrary.wiley.com/doi/10.1111/jace.14782/full>

H. X. Zhang, C. L. Fedelis, M. Wilhelm, Z. P. Xie and K. Rezwan, Macro/mesoporous SiOC ceramics of anisotropic structure for cryogenic engineering, Mater. Design 134 (2017) 207–217. <http://www.sciencedirect.com/science/article/pii/S0264127517307918>

Y. Grebenyuk, H. X. Zhang, M. Wilhelm, K. Rezwan, M. E. Dreyer, Wicking into porous polymer-derived ceramic monoliths fabricated by freeze-casting, J. Eur. Ceram. Soc. 37 (2017) 1993–2000.

<http://www.sciencedirect.com/science/article/pii/S0955221916306483>

### **A8.2 Conferences contribution:**

Oral presentation: H. X. Zhang, M. Wilhelm, K. Rezwan, Hierarchically structured SiOC glass by freeze casting technique, 4<sup>th</sup> Cellular Materials CellMat (2016) Dresden, Germany

Oral presentation: H. X. Zhang, C. Fedelis, A. Serva, M. Wilhelm, Z. P. Xie, K. Rezwan, Macroporous SiOC ceramics made by freeze casting for cryogenic applications, 9<sup>th</sup> International Conference on High Temperature Ceramic Matrix Composites and Global Forum on Advanced Materials and Technologies for Sustainable Development (2016) Toronto, Canada.

Oral presentation: H. X. Zhang, M. Wilhelm, K. Rezwan, Fabrication of Macroporous Polymer Derived Ceramic Monoliths by Freeze Casting Method, The 11<sup>th</sup> Pacific Rim Conference of Ceramic Societies (2015) Jeju, South Korea.

Poster presentation: H. X. Zhang, C. Fedelis, A. Serva, M. Wilhelm, K. Rezwan, Hierarchically-ordered porous SiOC monoliths made by freeze casting, 9<sup>th</sup> International Conference on High Temperature Ceramic Matrix Composites and Global Forum on Advanced Materials and Technologies for Sustainable Development (2016) Toronto, Canada.

Poster: H. X. Zhang, M. Wilhelm, K. Rezwan, Adjustment of macroporous structures and surface characteristics of polymer derived ceramic monoliths fabricated by sacrificial templating

method, 4<sup>th</sup> International Conference on Multifunctional, Hybrid and Nanomaterials (2015) Stiges, Spain.

### A8.3 Other publications:

H. X. Zhang, A. Chokkalingam, P. V. Subramaniam, S. Joseph, S. Takeuchi, M. D. Wei, A. M. Al-Enizid, H.G. Jang, J.H Kim, G. Seo, K. Komura, Y. Sugi and A. Vinu, The isopropylation of biphenyl over transition metal substituted aluminophosphates: MAPO-5 (M: Co and Ni), J. Mol. Catal. Chem. 412 (2016) 117–124.

<http://www.sciencedirect.com/science/article/pii/S1381116915301461>

H. X. Zhang, L. X. Zeng, X. M. Wu, L. F. Liang and M. D. Wei, Synthesis of MoO<sub>2</sub> nanosheets by an ionic liquid route and its electrochemical properties in lithium-ion battery, J. Alloys Compd. 580 (2013) 358–362.

<http://www.sciencedirect.com/science/article/pii/S0925838813014989>

H. X. Zhang, Y. F. Li, Z. S. Hong and M. D. Wei, Fabrication of hierarchical hollow MoO<sub>2</sub> microspheres constructed from small spheres, Mater. Lett. 79 (2012) 148–151.

<http://www.sciencedirect.com/science/article/pii/S0167577X12004661>

Y. F. Li, H. X. Zhang, B. B. Guo and M. D. Wei, Enhanced efficiency dye-sensitized SrSnO<sub>3</sub> solar cells prepared using chemical bath deposition, Electrochim. Acta 70 (2012) 313–317.

<http://www.sciencedirect.com/science/article/pii/S0013468612004306>

A. Y. Pang, Y. F. Li, H. X. Zhang, Y. Z. Wang and M. D. Wei, Dye-sensitized solar cells composed of Ti<sub>1-x</sub>Sn<sub>x</sub>O<sub>2</sub> nanocrystals, Materials Chemistry and Physics, 135 (1), (2012) 46–50.

<http://www.sciencedirect.com/science/article/pii/S0254058412003598>

Y. F. Li, X. Z. Zheng, H. X. Zhang, B. B. Guo, A. Y. Pang, M. D. Wei, Improving the efficiency of dye-sensitized Zn<sub>2</sub>SnO<sub>4</sub> solar cells: The role of Al<sup>3+</sup> ions, Electrochim. Acta 56 (2011) 9257–9261.

<http://www.sciencedirect.com/science/article/pii/S0013468611012035>

Z. S. Hong, T. B. Lan, F. Y. Xiao, H. X. Zhang, M. D. Wei, Ultrathin Li<sub>4</sub>Ti<sub>5</sub>O<sub>12</sub> nanosheets as a high performance anode for Li-ion battery, Funct. Mater. Lett. 04 (2011) 389–393.

<http://www.worldscientific.com/doi/abs/10.1142/S1793604711002287>